HYDROTHERMAL ACID-SULFATE ALTERATION
AT KRAFLA AND NÁMAFJALL, NE ICELAND:
IMPLICATIONS FOR GUSEV CRATER AND MERIDIANI PLANUM, MARS

by

George Lougheed Carson III

A Thesis Submitted in
Partial Fulfillment of the
Requirements for the Degree of
Master of Science
in Geosciences
at
The University of Wisconsin – Milwaukee
May 2015

ABSTRACT

HYDROTHERMAL ACID-SULFATE ALTERATION AT KRAFLA AND NÁMAFJALL, NE ICELAND: IMPLICATIONS FOR GUSEV CRATER AND MERIDIANI PLANUM, MARS

by

George Lougheed Carson III

The University of Wisconsin – Milwaukee, 2015
Under the Supervision of Dr. Lindsay McHenry

Opaline silica, sulfate, and phyllosilicate-bearing deposits have been detected on Mars from both obiters and rovers, indicating extensive aqueous alteration of the basaltic surface, some of which likely occurred under hydrothermal conditions. Ongoing hydrothermal acid-sulfate alteration of Mars-like high-Fe (15.48-16.27 wt. % Fe_2O_3T) basalts and hyaloclastites in northeastern Iceland was studied to help interpret the products of alteration in analogous environments on ancient Mars. The Krafla and Námafjall areas feature intense surface alteration in gas- (fumarole) and fluid- (hot spring/mud pot) dominated settings. Influx of H_2S gas ($H_2S + 2O_2 = H_2SO_4$) produced steam-derived acid-sulfate waters with pH values 1.96-2.50 at measured temperatures between 15-92°C, enriched in SO_4, Fe, and Al. During alteration, primary igneous phases (plagioclase, olivine, augite, and basaltic glass) reacted with acid-sulfate waters to produce secondary mineral assemblages dominated by amorphous silica, iron-sulfides, Ca/Fe/Mg/Al-sulfates, phyllosilicates (kaolin and smectite groups), and Fe-(hydr)oxides. Bulk compositions of alteration products were controlled by the leaching and mobilization of major elements (e.g. Ca, Mg, Na, K) out of the deposits, while Si, Ti, and Zr were residually enriched. Fe and Al mobility varied significantly, but these elements are largely retained in the products of alteration. These diverse environmental and geochemical processes in the Krafla and Námafjall areas may provide insight into Martian hydrothermal systems, specifically, the sulfate- and silica-rich deposits near Home Plate, Gusev Crater and in the layered sulfate and hematite deposits at Meridiani Planum.

TABLE OF CONTENTS

Appendices

LIST OF FIGURES

LIST OF TABLES

ACKNOWLEDGEMENTS

I would like to thank my advisors Drs. Lindsay McHenry and Barry Cameron, whose support and guidance was invaluable throughout the duration of this project, and for the countless opportunities they gave me to cultivate my geologic skills through field and laboratory work. In addition, the backbone of this project would not have been possible without unlimited access to Dr. McHenry's lab. I would also like to thank Dr. Brian Hynek at the University of Colorado – Boulder and Teri Gerard for their assistance and observations in the field, Dr. Heather Owen and TA Andrew Kirkpatrick of the UWM Biology Department for instruction on the SEM. Undergraduate lab assistants Chris Vickery, Darian Dixon, Michael Sara, Amanda Dahms, Austin Borgardt, and Mallory Runyan who were essential to completing the copious amounts of lab work with accuracy and efficiency. Finally, I would like to thank my funding sources, the UWM Research Growth Initiative, Wisconsin Space Grant Consortium, and UWM Department of Geosciences for their financial support during this project.

1. Introduction

Extremely acidic mud pots, hot springs, and fumaroles are common features of volcanic hydrothermal systems in Iceland. These features are produced when deep-circulating aquifer fluids undergo depressurization boiling, which effectively mobilizes the vapor phase compared to the liquid phase. Phase segregation produces steam rich in volatiles such as CO_2, H_2S, and H_2 gas, and a separate body of near-neutral boiled water enriched in non-volatile components. After phase segregation, the rising vapor mixes with oxygenated groundwater to produce steam-derived acid-sulfate waters. The water-rock interaction between steam-derived acid-sulfate waters and the basaltic substrate produces a wide-range of secondary minerals (~35 identified) characterized by silicic, solfataric, and advanced argillic alteration (*Heald et al., 1987*). Hydrothermal acid-sulfate alteration in volcanic environments is a common chemical weathering process on Earth and has been proposed for deposits on Mars.

Recent exploration of Mars by orbiters and rovers has revealed widespread occurrences of water-altered minerals, indicating prolonged water-rock interaction and extensive aqueous alteration of the basaltic surface. Remote sensing from the Compact Reconnaissance Imaging Spectrometer for Mars (CRISM) and Observatoire pour la Mineralogie, l'Eau, les Glaces et l'Activité (OMEGA) instruments onboard the Mars Reconnaissance Orbiter and Mars Express orbiter have revealed globally distributed opaline silica, sulfate, and phyllosilicate deposits in discrete locales at Meridiani Planum, Mawrth Vallis, and Nili Fossae and Noctis Labyrinthus (*Chojnacki & Hynek, 2008 Ehlmann et al., 2008, 2010*). Hydrothermal alteration associated with volcanic complexes has been proposed for features at Nili Patera and Gusev Crater (*Schmidt et al., 2008; Yen et al., 2008; Skok et al., 2010*).

The Mars Exploration Rover (MERs) provided *in-situ* geochemical and mineralogical data and close-up images of exposed bedrock from Meridiani Planum and Gusev Crater (e.g. *Squyres et al., 2004; Yen et al., 2008; Ming et al., 2008; Morris et al., 2008; Ruff et al., 2011*). Analyzed rocks and soils reflect extensive acid-sulfate alteration early in the history of Mars. In the Inner Basin of the Columbia Hills (Gusev Crater), MER Spirit identified silica-rich and sulfate-rich deposits in soils and outcrops near Home Plate that likely formed in a hydrothermal system. The exact role, magnitude, and timing of water-rock interactions near Home Plate are still not fully understood. At Meridiani Planum, MER Opportunity observed layered sulfate and hematite deposits within the Burns Formation and interpreted to be the result of acid-sulfate weathering via low-temperature groundwater processes (e.g. *Squyres et al., 2004*). Alternatively, acid-sulfate alteration of ash deposits by SO_2-bearing vapors in high-temperature hydrothermal environments has been proposed by *McCollom & Hynek* (2005).

To more fully understand the alteration processes at Gusev Crater and Meridiani Planum, it is vital to differentiate between secondary minerals on Mars that formed through hydrothermal alteration and by other geological processes. Identifying key alteration signatures in hydrothermal acid-sulfate systems may better constrain the paleoenvironmental conditions that were present at the time of formation (e.g. temperature, pH, Eh, fluid composition, etc.). To address this issue, we investigated the mineralogical and chemical trends during acid-sulfate alteration in gas- (fumarole) and fluid- (hot spring/mud pot) dominated settings in the Krafla and Námafjall geothermal areas (NE Iceland). These sites were selected because their basaltic composition is similar to Martian rocks and soils. In addition, active fumaroles and hot springs provide an excellent natural laboratory to study on-going acid-sulfate alteration of Mars-like high-Fe basalts and hyaloclastites.

The main objectives for this research are to (i) assess the specific mineral assemblages that arise through hydrothermal alteration of high-Fe basalt and hyaloclastite, and how they correspond to gas- and fluid-dominated settings, (ii) assess which elements are preferentially leached and/or retained in the alteration products, (iii) determine the lithological and environmental controls on the secondary mineralogy, and (vi) compare these terrestrial assemblages to those in soils and rocks in the Gusev Crater, Merdiaini Planum, and elsewhere on Mars. This study builds upon previous work in the Námafjall area (e.g. *Geptner et al., 2005; 2007, Mínguez et al., 2011*) and provides the first comprehensive mineralogical and geochemical dataset in the Krafla area. My goal is to understand if the Krafla and Námafjall areas produce diagnostic secondary minerals and features that can provide a framework for interpretations of relict hydrothermal systems on Mars. On Earth, the presence of heat, liquid water, and nutrients associated with hydrothermal systems provide the necessary ingredients for microbial life. In this study, we present the mineralogical and geochemical context for prospective environments that may have once hosted life on Mars.

2. Mars Background

2.1 Martian Geologic Timeline

The geologic history of Mars is divided into three periods based on stratigraphy, crater density, and morphology: the Noachian (4.4-3.8 Ga), Hesperian (3.8-2.0 Ga), and Amazonian (2.0-present) (*Scott & Carr, 1978; Tanaka, 1986; Bibring et al., 2005*). Figure 1 shows *Bibring et al.'s* (2006) three sequential eras based upon the dominant alteration product observed across the Martian surface: (i) phyllosilicates (the "phyllosian" era), (ii) sulfates (the "theiikian" era), and (iii) ferric oxides (the "siderikian" era) (*Bibring et al. 2005, 2006*). The earliest phyllosian era produced widespread Mg/Fe- and Al-rich phyllosilicates through aqueous alteration at the surface, or through subsurface hydrothermal activity (*Bishop et al., 2008; Mustard et al., 2008*).

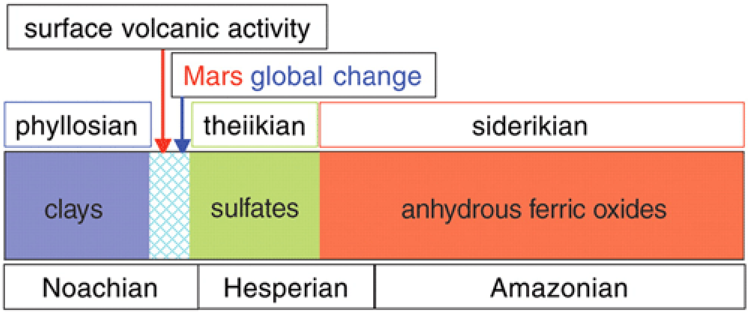

Figure 1: Martian history based on mineral formation (image from *Bibring et al., 2006*).

The theiikian era is characterized by Fe-, Ca-, and Mg-sulfate deposits formed through as extensive evaporitic and/or hydrothermal processes. The transition between the phyllosian and theiikian eras occurred during a critical episode of global climate change on Mars. *Bibring et al.* (2006) postulated that the aqueous environment changed from alkaline to acidic, which may have been coupled by a rapid drop in atmospheric pressure, possibly the result of the heavy bombardment on early Mars (*Chassefiere et al.,* *2004*). The final siderikian era is distinguished by the absence of liquid water, where the main processes involve atmospheric weathering through peroxide reactivity or frost/rock interactions. These processes affect the surface layer, which was directly observed by MER Spirit at Gusev Crater as alteration rinds on the exterior of otherwise unaltered basalts (*Squyres et al., 2004; Ming et al., 2006*).

2.2 Martian Surface Composition

The exposed Martian surface is largely thoeleiitic basalt, consistent with the lack of plate tectonics and associated magmatic processes seen on Earth. Some regions are spectrally consistent with andesite, although these have since been reinterpreted as weathered basalts (*Wyatt et al., 2002*). The Mars Pathfinder landing site also featured rocks with the chemical composition of basalt-andesite to andesite, but these are likely the result of alteration rinds produced via chemical weathering and are now interpreted as basalts (*McSween et al., 2009).* One confirmed intermediate-to-felsic igneous rock unit (i.e. dacite) was identified in the Nili Patera caldera of Syrtis Major based on orbiter-based thermal infrared spectroscopy (*Wray et al., 2013*), while other occurrences of evolved siliceous rocks remain suspect (e.g. *Bandfield et al., 2004; Ehlmann et al., 2009*). These observations support the view that magmatic differentiation has been limited throughout the geologic history of Mars.

Our understanding of the surface of Mars has been refined by MER Spirit and Opportunity, which investigated *in-situ* primary mineralogy and elemental compositions of basaltic soils and rocks (*Squyres et al., 2004, 2006; Klingelhöfer et al., 2004*). Primary igneous mineral assemblages include olivine, pyroxene, plagioclase, and magnetite (*Christensen et al., 2004; McSween et al., 2008; Ming et al., 2008; Morris et al., 2008*).

Plagioclase analyzed from Martian meteorites and basalts have low anorthite compositions (~$An_{30\text{-}60}$) (*Papike et al., 2009*). Gusev basalts and the basalt precursor reconstructed for Meridiani Planum have high Fe_2O_3T content compared to terrestrial basalts and similar bulk and Fe-mineralogical compositions, although basalt composition does vary across Mars. Recent observations by the Mars Science Laboratory (MSL) Curiosity rover revealed alkaline basalts in Gale crater (*McLennan et al., 2013*).

2.3 Martian Hydrothermal Systems

The geologic setting and areal extent of the sulfate deposits suggest a variety of geological and chemical processes of formation, and potential explanations have included precipitation during evaporation of acidic sulfate-bearing groundwater (*Squyres et al., 2004*), ‘acid fog’ (*Tosca et al., 2004*), acid weathering in a glacial environment (*Niles & Michalski, 2009*), oxidation of pyrite or other sulfides minerals (*Zolotov & Shock, 2005*), and impact processes (*Knauth et al., 2005*). Additionally, the OMEGA team suggested that the circulation of sulfur-rich fluids altered volcanic ash into sulfates (*Gendrin et al., 2005*). While each of the proposed scenarios is geologically and chemically feasible, given the abundant volcanism and surface water on early Mars, it is likely that some of the altered deposits were formed as the result of hydrothermal acid-sulfate alteration (*Hynek & Phillips, 2001; Hynek et al., 2011, 2013*).

Potential hydrothermal activity associated with volcanic edifices has been proposed at Nili Patera, SW Elysium Planitia, Apollinaris Patera, and Gusev Crater (*Morris et al., 2008; Lanz et al., 2009; Skok et al., 2010, El Maarry et al., 2012*). The detection of hydrothermal minerals from orbiter platforms and *in situ* observations of putative hydrothermal deposits at Gusev Crater indicate that acid-sulfate alteration in basalt-hosted hydrothermal environments was likely present on the surface of Mars. Basaltic volcanism was widespread (*McSween et al., 2008*) and given the relatively high contents of sulfur in Martian basalts, significant outgassing of sulfur volatiles (e.g. SO_2, H_2S) occurred during these eruptions (*Craddock & Greeley, 2009*). The reaction of volatile sulfur compounds in magmatic vapors and/or groundwater would produce acid-sulfate waters that would subsequently alter the basaltic crust. The overall gas-water-rock interactions could produce a hydrothermal system with sulfur-rich volcanic discharge areas at fumaroles, solfataras, and hot springs.

Understanding how the observed alteration mineralogy fits into its geologic and geomorphic context is vital to unraveling the environmental and geochemical processes present at the time of formation. The MER missions provided detailed geochemical and mineralogical data, offering insights into acid-sulfate alteration of high-Fe basalts in Hesperian-aged deposits at the putative hydrothermal system near Home Plate, Gusev Crater and in potential hydrothermal solutions in the Burns Formation at Meridiani Planum.

2.3.1 Home Plate, Gusev Crater

In 2005, MER Spirit began to traverse the Inner Basin of the Columbia Hills and discovered compelling evidence for a fossil hydrothermal system. Home Plate, a plateau in the Columbia Hills, is an 80 m quasi-circular platform and 1.5 m thick layered sequence of altered alkali basaltic tephra (Figure 2). The lower unit is composed of likely accretionary lapilli and reflects the accumulation of pyroclastic materials. The upper unit consists of fine-grained beds with planar to low-angle cross-stratification, reflecting eolian re-working (*Squyres et al., 2007*). A particularly notable feature in the lowermost unit is a ~3 cm clast interpreted as a bomb sag derived from a block from a phreatomagmatic eruption that landed on and deformed a volcaniclastic layer. Volcanic activity may have produced high-temperature subsurface conditions that resulted in hydrothermal activity, which could have saturated the lowermost unit at the time of deformation and eruption (*Manga et al., 2012*). Elevated Barnhill class rocks (lower unit) contain higher concentrations of halogens (i.e. Cl and Br) and volatile siderophile elements (i.e. Ge and Zn), which may imply interaction with briny groundwater during the eruption and/or later hydrothermal alteration (*Schmidt et al., 2008*).

Additional evidence of water and high-temperature conditions was observed when Spirit's Alpha Particle X-ray Spectrometer (APXS) analyzed two classes of soils: sulfate-rich Paso Robles (targets Paso Robles, Tyrone, Arad) class soils and the silica-rich Gertrude Weise (targets Lefty Ganote, Kenosha Comets) class soils. Near the Home Plate volcanic structure, the Paso Robles and Gertrude Wiese class soils strongly suggest aqueous alteration processes based on mineralogical, geochemical and textural observations (Figure 2b,c). The Paso Robles class soils likely formed in a fumarolic environment or through pyrite oxidation (*Yen et al., 2008*). The silica-rich Gertrude Weise soils formed either through acid-fumarole leaching or near-neutral hot spring sinter deposition (*Ruff et al., 2011*).

Both soils are inferred to belong to the same hydrothermal system because they are in close proximity to one another, however; it is unknown whether these two soil classes are temporally related, or whether they represent discontinuous altered pods. *Schmidt et al.* (2009) theorized that the silica-rich Gertrude Weise class soils may be the result of late alteration compared to the sulfate-rich Paso Robles class soils. Regardless, the variation in secondary mineral assemblages and geochemical data suggest that a dynamic, laterally variable hydrothermal system once existed around Home Plate. Additional hydration signatures have been identified throughout the Home Plate region, and may indicate a more widespread aqueous environment (*Rice et al., 2010*).

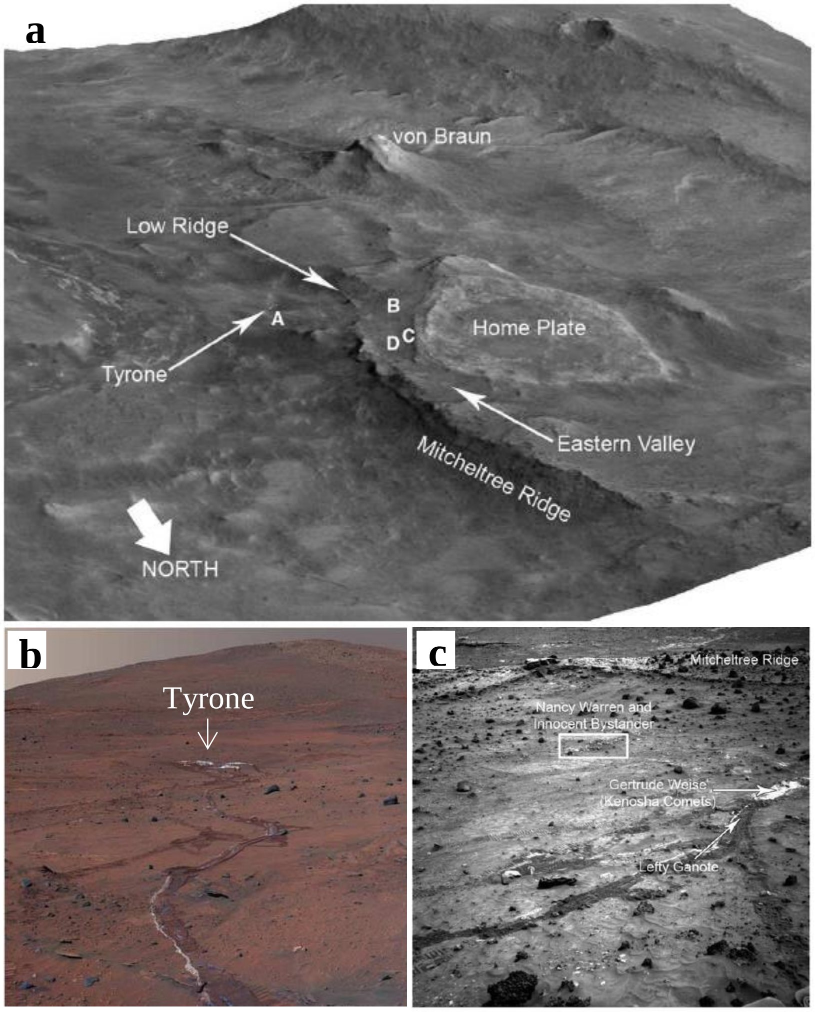

Figure 2: Oblique view of the Inner Basin of the Columbia Hills, Gusev Crater, Mars. (a) A – Tyrone nodule outcrops, B – Kobal outcrop, C – Elizabeth Mahon outcrop, and D – Gertrude Weise soils. (b) Target Tyrone in the Paso Robles class soils is a sulfate-rich deposit with high SO_3 concentrations. (c) Target Kenosha Comets in the Gertrude Weise class soils is a silica-rich deposit composed of opal-A silica. Images from *Squyres et al., 2008; Yen et al., 2008.*

2.3.2 Burns Formation, Meridiani Planum

In 2004, MER Opportunity rover landed in Eagle Crater at Meridiani Planum (Figure 3). The site was chosen for its flat terrain and the anomalously high concentration of gray crystalline hematite detected from orbit by the Mars Global Surveyor (MGS, *Christensen et al., 2000*). The sedimentary outcrops observed by Opportunity indicated aqueous processes, including planar lamination, ripple cross-lamination, low angle cross-stratification, cross bed sets, and embedded spherules/vugs (*Grotzinger et al., 2005*). During its traverse, Opportunity encountered the deposits of what became known as the Burns Formation, which contains hematite-rich spherules (blueberries) dispersed throughout an altered siliciclastic and sulfate-rich outcrop. Modal mineralogy of the Burns Formation includes three major components: 50-60% of the sediments are siliciclastic, 30-40 % are sulfates (Mg- and Ca-sulfates, jarosite), and 10% is hematite (mostly 0.6-6 mm spheroidal concretions) (*Knoll et al., 2005*; *Glotch & Banfield, 2006*). TES mapping has shown that Meridiani Planum contains 5-20% coarse-grained hematite over an area of at least 175,000 km^2. Other surfaces on Mars with more than a few percent coarse-grained hematite are located at Aram Chaos and discrete locales within Valles Marineris (*Christensen et al., 2001*).

Multiple models for the formation of the Meridiani Planum hematite spherules have been suggested. The MER team invokes groundwater alteration of sulfate-rich sand deposits, concentrating fluids in iron and producing hematite spherules. Episodic inundation by surface water to shallow depths, followed by evaporation, exposure, and desiccation, are indicated by sedimentary features and geochemistry (*Squyres et al., 2005*). Groundwater upwelling at Meridiani Planum is supported by global groundwater modeling of ancient flow paths (*McLennan et al., 2005; Andrews-Hanna et al., 2007*).

Other models invoke the deposition of volcanic ash followed by reaction with condensed vapors emitted from fumaroles (*McCollom & Hynek*, *2005*), precipitation from low temperature brines (*Elwood Madden et al., 2004*), or extremely acidic aqueous conditions (*Fernandez-Remolar et al., 2004*). *Golden et al.* (2008) concluded that hematite spherules can form under hydrothermal aqueous conditions during the dissolution of hydronium jarosite, albeit their experimentally-derived spherules are much smaller than those observed on Mars. Although the exact formation mechanism is not fully constrained, it is likely that hematite 'blueberries' precipitated from acid-sulfate solutions of some kind.

Figure 3: Pancam image of Slickrock in the Burns Formation showing planar/low-angle bedding and embedded hematite spherules (Squyres et al. 2004).

3. Geologic Setting

3.1 Iceland

Iceland lies astride the Mid-Atlantic Ridge, where an asthenospheric flow under the North American and the Eurasian Plate boundary interacts and mixes with a deep mantle plume. The buoyancy of the plume uplifted the Icelandic plateau and produced high levels of volcanic activity. Through seismic imaging, the plume has been measured down to ~400 km depth, and tentatively down to the core-mantle boundary (*Helmberger et al., 1998; Wolfe et al. 2002*). Icelandic rift zones have migrated eastwards over the past 20 Ma, with active volcanic belts moving in a step-like progression along with the surface expression of the plume, creating a complex and evolving rift and transform fault zone. Active volcanism and tectonism occurs in four modern rift zones including Reykjanes, Western, Eastern, and Northern Volcanic Zones.

3.2 Krafla Central Volcano Background

Krafla central volcano lies above the Icelandic mantle plume at the Mid-Atlantic Ridge within the Northern Volcanic Zone. Krafla volcano forms a low, broad shield (~25 km diameter); with an 8 by 10 km caldera bisected by a 100 km en echelon NNE-trending fissure swarm (Figure 4) (*Gudmundsson & Arnorsson, 2002, 2005*). The Krafla central volcano exhibits a distinct dacitic welded-tuff caldera rim that formed ~110 ka ago (*Björnsson et al., 1977*). The caldera has been partially in-filled with predominantly basaltic eruptive products with lithologies dominated by hyaloclastite, subaerial lava flows, and fine-grained tuffs, while edifices of icelandite, dacite, and rhyolite have also been emplaced (*Stefansson, 1981; Saemundsson, 1991*). Pleistocene hyaloclastites formed during subglacial eruptions, while Holocene (3 ka – present) subaerial lavas were emplaced during six major eruptions with an interval period of 250-1000 years (*Seamundsson, 1991*). This study focuses on Holocene (post-glacial) basalts and Pleistocene (subglacial) hyaloclastites currently undergoing intense surface hydrothermal alteration in the Krafla and Námafjall areas.

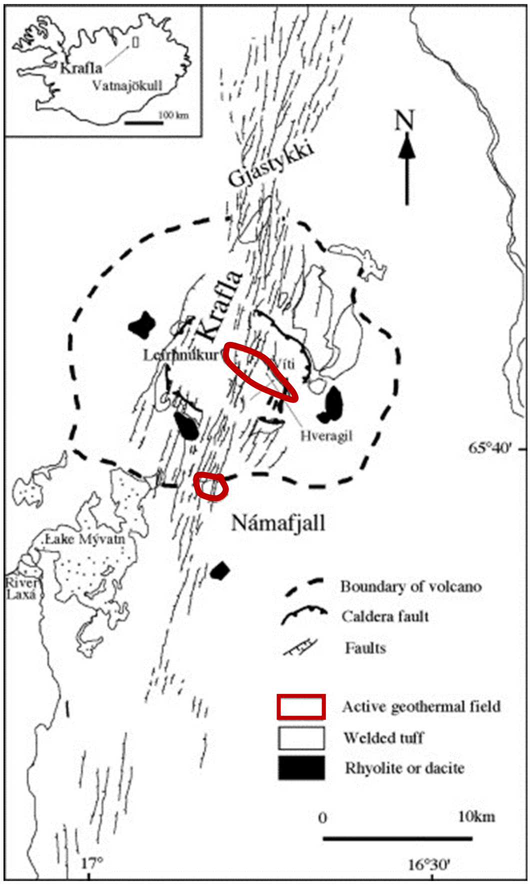

Figure 4: Map of the Krafla central volcano. Krafla and Námafjall geothermal areas are outlined in red. Insert shows the location of Krafla, north of Vatnajökull glacier. Image modified from *Gudmundsson and Arnorsson, 2005.*

3.2.1 Holocene Basalts

Two historic eruptions took place near the active geothermal site at Leirhnjúkur. The 1724-29 eruption is called “Myvatnseldar” in Icelandic, or Mývatn Fires, and is described in detail by *Grönvold* (1984). The eruptive episode began in May 1724 with a rhyolitic phreatomagmatic eruption at Víti, while subsequent rifting and effusive eruptions occurred along an 11 km discontinuous row of craters. Detailed timing of this eruptive episode is not known, but is analogous to the 1975-84 Krafla Fires eruption, or “Kröflueldar” in Icelandic. Myvatnseldar produced both a’a and pahoehoe lava types, whereas Kröflueldar produced mostly pahoehoe lava (*Nicholson, 1991*).

Late Holocene subaerial basalt produced during Lúdent stage (>6100 B.P.) volcanism covers the Hverir geothermal field. During this period, 13 eruptions occurred in the central caldera along with 8 near Námafjall (Hverir). Some of these eruptions may have emanated from the same eruptive vent associated with the Krafla caldera, but stratigraphic control is not sufficient to correlate volcanic events across the whole volcanic system (*Nicholson, 1991*).

Holocene basalts are fine-grained, holocrystalline, and highly vesicular. Central caldera eruptions have produced quartz tholeiites with limited major element variability, composed of olivine, plagioclase, clinopyroxene (augite), Ti-Fe oxide (titanomagnetite) and interstitial basaltic glass (*Grönvold, 1984; Gudmundsson and Arnorsson, 2002, 2005*). These basalts are composed largely of opaque minerals (e.g. titanomagnetite) that largely contribute to the high-Fe basaltic composition in Krafla basalts. Titanomagnetite crystals exhibit skeletal and cruciform texture, indicating rapid cooling of the basaltic lava (Figure 5c) (*Urcia et al., 2010*). Plagioclase is the most abundant phenocryst phase, while forsterite and augite are present in minor amounts, and both exhibit a distinct euhedral texture (Figure 5a,b). Olivine and augite phenocrysts are larger and more abundant in the Late Holocene eruption compared to the recent Mývatn and Krafla Fires eruptions.

Basalts are less porous compared to hyaloclastites and largely crystalline, and release elements into solution according to the stability of primary igneous phases. According to the dissolution experiments of *Stefánsson et al. (2001)*, the suggested sequence of mineral stability during basalt alteration in the Krafla area is the following (most reactive to least reactive): Mg-olivine > Fe-olivine, Ti-rich magnetite > Ca-plagioclase, Mg-orthopyroxene > Fe-orthopyroxene, clinopyroxene > Na-plagioclase, F-apatite > Ti-rich ilmenite >> Ti-poor magnetite, Ti-poor hematite. These results correlate well with observations of weathered basalt elsewhere in Iceland (e.g. *Nesbitt & Wilson, 1992*). Krafla basalts are altered by fumaroles, where the extent of alteration tends to be limited to individual alteration halos or aprons. The random distribution of these features may be related to underlying faults or, perhaps, collapsed deflation features in the lava field that create a pathway for volcanic vapors to ascend to the surface.

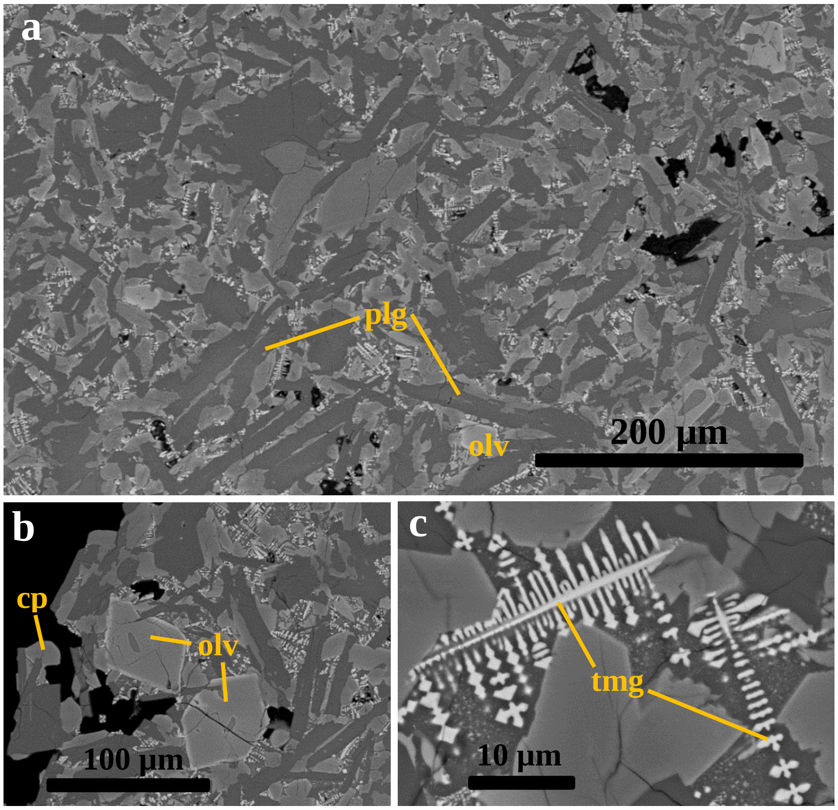

Figure 5: Back-scattered image of a cross section of fresh basalt from the 1724-29 Mývatn Fires eruption. (a) Crystalline basalt with abundant plagioclase laths (dark grey), (b) minor euhedral olivine crystals and (c) skeletal and cruciform titanomagnetite crystals. Plagioclase = plg, olivine = olv, clinopyroxene = cpx, and titanomagnetite = tmg.

3.2.2 Pleistocene Hyaloclastites

During the Pleistocene most of the eruptive products were influenced by the presence of ice or melt-water, forming three main types of landforms: hyaloclastite ridges, tuyas, and rhyolite domes. Hyaloclastite ridges are pronounced topographic features over 100 m high, which consist mainly of pillow basalts, breccia, and glass fragments erupted into a meltwater vault under an ice sheet. Hyaloclastite ridges run approximately parallel to the Krafla post-glacial fissure swarm (e.g. Námaskard and Leirhnjúkur) (*Einarsson, 2008*). Hyaloclastites are composed of basaltic glass (i.e.

sideromelane) and plagioclase phenocrysts. Minor secondary alteration (or palagonitization) has formed a hydrated and heterogeneous smectite-like material around fresh glass or pillow fragments (*Stroncik & Schminke, 2001*).

Hyaloclastite formations tend to be highly porous, however; permeability markedly decreases with increasing alteration as secondary minerals precipitate into the voids. Even so, the loss of primary or original porosity is offset by the production of micro-porosity observed in the most altered samples (*Franzson et al., 2011).* High porosity promotes the migration of geothermal fluids, along with element transport of all major oxides from the dissolution of chemically unstable sideromelane. Prolonged low-temperature alteration can replace sideromelane with smectite, zeolites, and Fe-(hydr)oxides.

3.2.3 Comparison to Martian Basalts

Holocene basalts in the Krafla caldera are relatively evolved in the Icelandic NVZ with moderate MgO (5.51-5.94 wt. %) and high Fe_2O_3T (15.39-16.78 wt. %), while Pleistocene hyaloclastites have higher Al_2O_3 (14.98-16.42 wt. %) and MgO (8.05-8.63 wt. %) with much lower Fe_2O_3T (9.76-11.16 wt. %) compared to the Holocene basalts (*Gronvold, 1984; Nicholson, 1992; Maclennan et al., 2002; Koornneef et al., 2011; Sims et al., 2013*). The Krafla Holocene basalts have a high Fe_2O_3T content relative to most terrestrial basalts and are close to Martian high-Fe basaltic compositions. In addition, Krafla eruptive products are closer in Fe_2O_3T, MgO, Al_2O_3 and alkali contents for the range of soils and rocks in the Gusev Crater and Meridiani Planum than previous Mars analog sites (Figure 6) (e.g. *Morris et al., 2005; Hynek et al., 2013*). The composition of pristine unaltered basalt is important because it largely controls the composition of the fluids during the alteration process, which places constraints on the secondary phases present and their abundance (e.g. *Tosca et al., 2004*).

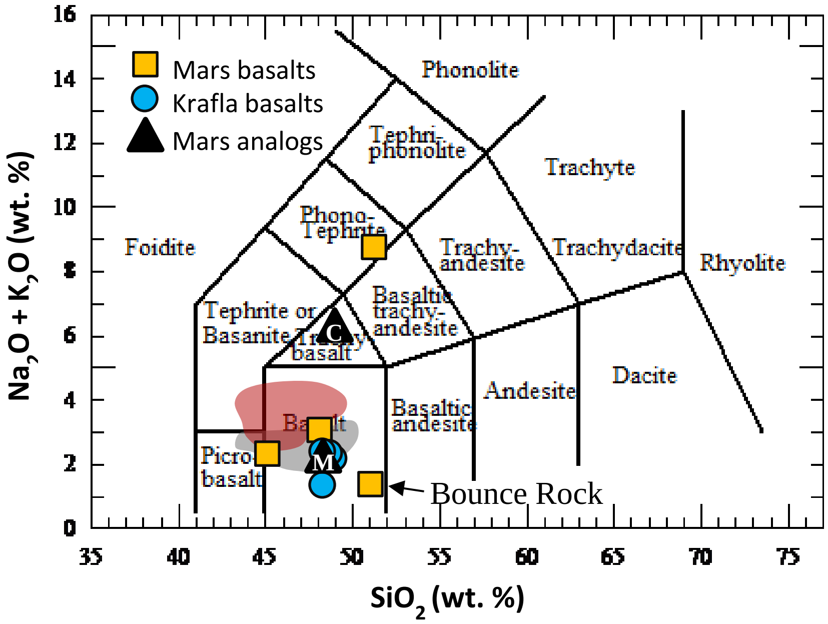

Figure 6: Total alkalis versus silica of Krafla basalts, Mars basalts, and other Mars analogs (M = Mauna Kea, C = Cerro Negro). Diagram after Le Bas et al., 1986. Shaded areas represent the analyses of the range of Gusev and Meridiani Planum rock and soil compositions (red = Gusev Crater; gray = Meridiani Planum). Blue and orange circles are Krafla and Mars basalt compositions, respectively, shown in Table 3. Bounce Rock analysis from *Rieder et al., 2004*.

3.3 Icelandic Geothermal Systems

Icelandic geothermal systems are classified as either high or low-temperature systems (*Bödvarsson, 1961*). Low temperature systems are widespread in the Quaternary and Tertiary formations and may be the result of fluid convection in young fractures formed by deformation of older crust, the drifting of high-T systems out of active volcanic belts, or intrusion of magma into fractures outside of active volcanic belts (*Saemundsson, 1967*). Low-temperature systems are defined as <150°C at 1000 m depth, whereas high-temperature systems are >200°C at 1000 m depth, located within central complexes in active rifting zones.

High-temperature geothermal systems develop when deep circulating aquifer fluids are heated by shallow magma bodies and ascend through NNE oriented rift-related fractures and undergo depressurization boiling (*Bödvarsson et al., 1984*). This effectively mobilizes the vapor phase compared to the liquid phase, which is retained within the pore wall surfaces due to capillary forces. Phase segregation produces less dense steam rich in volatiles such as CO_2, H_2S, and H_2 gas, and a separate body of near-neutral boiled water enriched in non-volatile components. After phase segregation, the rising vapor mixes with oxygenated groundwater to produce steam-derived acid-sulfate waters based on the following reaction:

$$H_2S + 2O_2 \rightarrow 2H^+ + SO_4^{2-}$$

These systems produce three distinct groups of surface geothermal waters based on their chemical composition: NaCl waters (pH >8), steam-derived acid-sulfate waters (pH<4), and mixed geothermal waters with near-neutral pH oxygenated surface- and groundwater.

Water-rock interactions in both active and relict geothermal systems at depth are well documented at Krafla and other high-temperature Icelandic systems as the result of geothermal exploration (e.g. *Gudmundsson & Arnórsson, 2002; Karakaya et al., 2007*). Aqueous alteration of basaltic bedrock at depth produces three distinct zones, reflecting the temperature stability of the alteration mineral assemblage that includes: a smectite-zeolite zone, a zone of mixed-layer clays and prehnite, and a chlorite-epidote zone (*Kristmanndottir, 1982*). Alkali-feldspars, sulfides, quartz, and calcite are found independent of temperature (*Lonker et al., 1993; Franzson et al., 2008)*. These studies indicate that subsurface alteration mineralogy is controlled largely by the equilibrium between geothermal minerals and fluids in Icelandic systems (*Stefánsson & Arnórsson, 2002; Gudmundsson & Arnórsson, 2005*).

3.4 Krafla High-Temperature Geothermal Systems

The Krafla central volcano hosts two distinct high-temperature (~320-350°C) geothermal fields: Krafla and Námafjall (Figure 7). The Krafla geothermal area is located at Leirhnjúkur in the center of the Krafla caldera, while Námafjall is located ~8 km south of Leirhnjúkur along the Krafla volcano boundary. Low total dissolved solids (~700-1500 ppm), geochemical, and isotopic characteristics from geothermal exploration wells indicate that the thermal waters are fed by local meteoric water (*Árnorsson, 1995).* Other thermal waters across Iceland are derived from a mixture of rain and glacial meltwater or the incursion of seawater (*Pope et al., 2013*). Other than H_2O, CO_2 is the dominant volcanic gas at Krafla, while Námafjall has higher H_2S and H_2 gas with overall lower gas concentrations (*Ármannsson, 1993*). Geothermal surface waters are dominated by steam-derived acid-sulfate waters.

Sulfuric acid readily alters the basaltic bedrock to produce zones of intense surface alteration, which at Krafla cover an area of 15 km^2, while at Námafjall cover 3-4 km^2. Solfataric, silicic, argillic and advanced argillic alteration results from the water-rock interaction between basaltic substrate and acid-sulfate waters (*Stefánsson, 1981; Arnórsson et al., 2007*). Widespread fumarolic and hot spring (mud pot) alteration has formed light-toned deposits ranging from white to tan, while dark-toned deposits range from purple to rusty red to orange to brown.

3.4.1 Námafjall Geothermal Area

Intense geothermal activity is centered along Námaskard (Figure 7b), where volcanic vapors and abundant surface waters are concentrated in the vicinity of drainage channels (Figure 8a,c). Hydrothermally altered hyaloclastites are crosscut by subvertical gypsum veins, which are the surface expression of faults and fissures associated with the Krafla fissure swarm (Figure 9). On the slopes of Námaskard, talus deposits consist of blocks of clay, clayey siltstones, and lenses and beds of gravelly conglomerates (*Geptner et al.*, 2007).

The Hverir geothermal field lies to the east of Námaskard and is dominated by vigorous fumaroles along a fault, with abundant mud pots on the downthrown side (Figure 8b) (*Saemundsson et al., 2012*). Large circular fumarolic aprons (up to ~25 m diameter) that produce little to no volcanic vapors are scattered randomly across the Late Holocene lava field nearby.

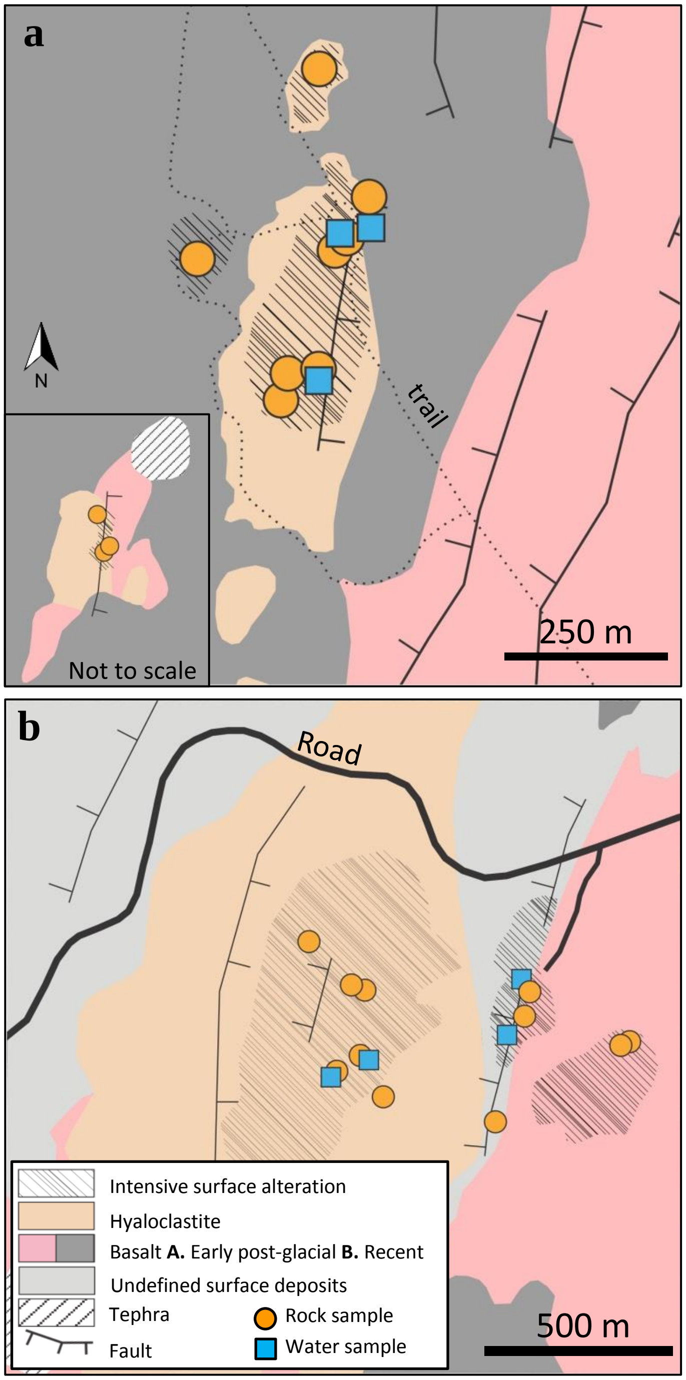

Figure 7: Simplified geologic map of the (a) Krafla (Leirhnjúkur) and (b) Námafjall geothermal areas. Insert shows Lítli-Leirhnjúkur, which lies NW of Leirhnjúkur. Map adapted from *Saemundsson et al., 2012.*

3.4.2 Krafla Geothermal Area

Activity at the Krafla geothermal field is centered at Leirhnjúkur (or “clay-hill” in Icelandic), which is a heavily altered hyaloclastite ridge (Figure 10). Volcanic vapors and thermal features are present over two broad areas: one along the southern end in the vicinity of a discharge channel and another associated with a discharge basin to the north (Figure 7a). Diffuse vapors are present sporadically within the Krafla Fires basalt just north beyond Leirhnjúkur. In the drainage channel, boiling mud pots and fumaroles are frequent, with abundant surface hydrothermal fluids present (Figure 10b). The discharge basin to the north has a large thermal pool with several smaller boiling hot springs along its perimeter, and surface run-off is channeled to the east (Figure 10c).

I investigated two other alteration areas along hyaloclastite ridges within the Krafla geothermal system: a large mound north of Leirhnjúkur and Lítli-Leirhnjúkur (Figure 11f). Lítli-Leirhnjúkur (or “little clay-hill”), an isolated hyaloclastite ridge surrounded by historic basalt flows, lies NW of Leirhnjúkur (Figure 11e). Lítli-Leirhnjúkur is not currently thermally active and, therefore, represents a relict hydrothermal system.

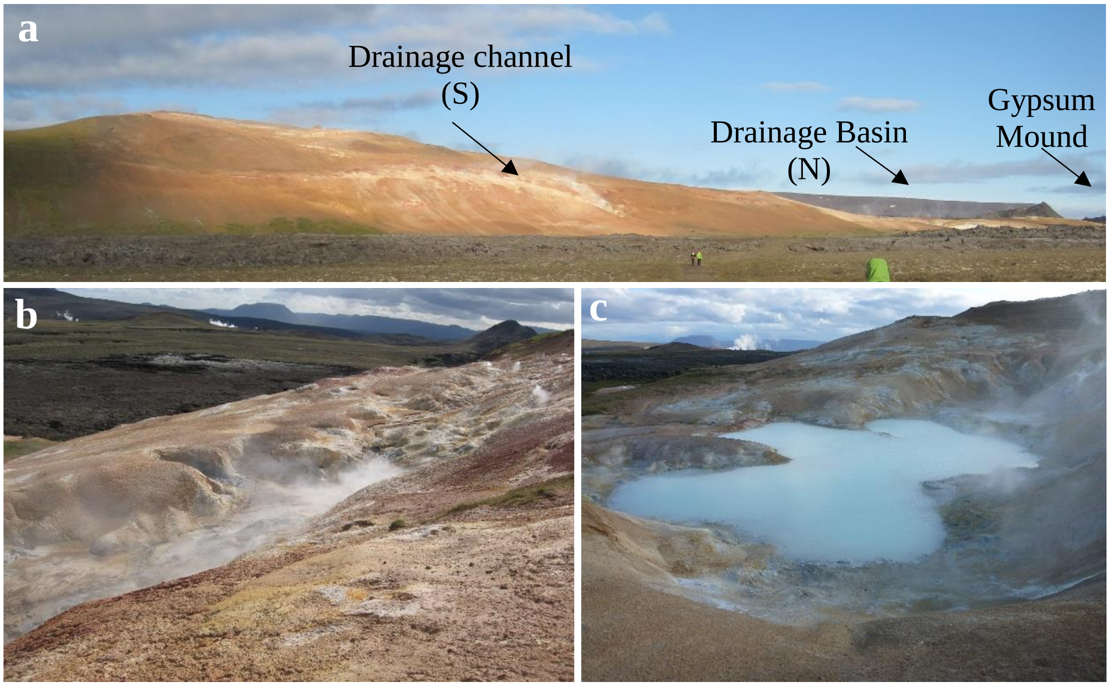

Figure 8: View of Námaskard (or "Mount Námafjall" in Icelandic) and other geothermal features. Námaskard is a basaltic hyaloclastite ridge that has experienced widespread alteration. Visible volcanic vapors and on-going alteration is focused in a large drainage channel that extends from the top of Námaskard. Hverir lies to the east of Námaskard, where geothermal features are associated with a fault. The downthrown side (W) features extensive mud pots, while towards the east (E) fumaroles are the dominant thermal feature. (a) Námaskard, (b) Hverir geothermal field is associated with a fault (dashed line), and (c) the drainage channel near the top of Námaskard (Dr. Lindsay McHenry for scale).

Figure 9: Subvertical gypsum veins at Námaskard

Figure 10: View of Leirhnjúkur and two broad alteration areas. They feature active fumaroles, hot springs, and mud pots, a discharge channel to the south (S), and a drainage basin to the north (N). Further north, there is a hyaloclastite mound with abundant gypsum crystals. (a) Leirhnjúkur, (b) the upper section of the discharge channel with visible volcanic vapors, and (c) a large thermal pool and small hot springs within the drainage basin.

3.4.3 Surface Alteration Mineralogy

Surface hydrothermal alteration of Pleistocene hyaloclastites and Holocene lavas in the Námafjall geothermal area was investigated by *Geptner et al.* (2005, 2007) and *Mínguez et al.* (2011). These studies focused on outcrops and re-deposited talus sediments on the outer edges of present-day fumarole activity. The major components of these deposits are kaolinite, smectite, and iron-oxyhydroxides, while minor abundances of anatase, pyrite, gypsum, and zeolites were observed. The extent of alteration, range in smectite composition, and overall mineral assemblages were observed to vary across the geothermal field, which generates a spotty distribution of red, brown, yellow, pink, and white colored-patches. This mosaic pattern is characteristic of hydrothermal alteration along the distal margins at Námaskard, as the result of surface run-off and diffusive flow of vapors and fluids through heavily altered hyaloclastite deposits, with surface temperatures ranging from ~100°C to ambient.

4. Methods

4.1 Field Work

Samples were collected in August 2013 and 2014 from active geothermal areas associated with the Krafla central volcano, NE Iceland (Figure 11). Figure 7 shows the spatial distribution of altered deposits and geothermal waters collected in the Krafla and Námafjall geothermal fields. We focused on collecting altered basalt and secondary minerals from areas of intense surface alteration. In addition, we collected basaltic substrate samples in areas of little to no geothermal activity to determine the pristine basalt composition relative to the secondary deposits. Surface samples were collected in detailed transects across localized, high-temperature gas- (fumarole) and fluid- (hot spring) discharge areas, which allowed us to document the changes in surface color, temperature, mineralogy, and geochemical composition of the altered deposits with distance from an active thermal feature. Subsurface observations (<1m) and sampling were conducted by trenching with a shovel. We gathered data including GPS coordinates, temperature, depth, texture, and color at all sample locations, and pH for sites with sufficient fluids. In total, this study focuses on ~50 samples collected from the Námafjall/Hverir and Krafla geothermal field. Samples are classified based on their color (e.g. red sediment), nearby thermal feature, and the associated substrate (Appendix C). Variation in sediment color is highlighted in Figure 12. After collection in the field, the samples were stored in individual plastic bags until preparation for analysis.

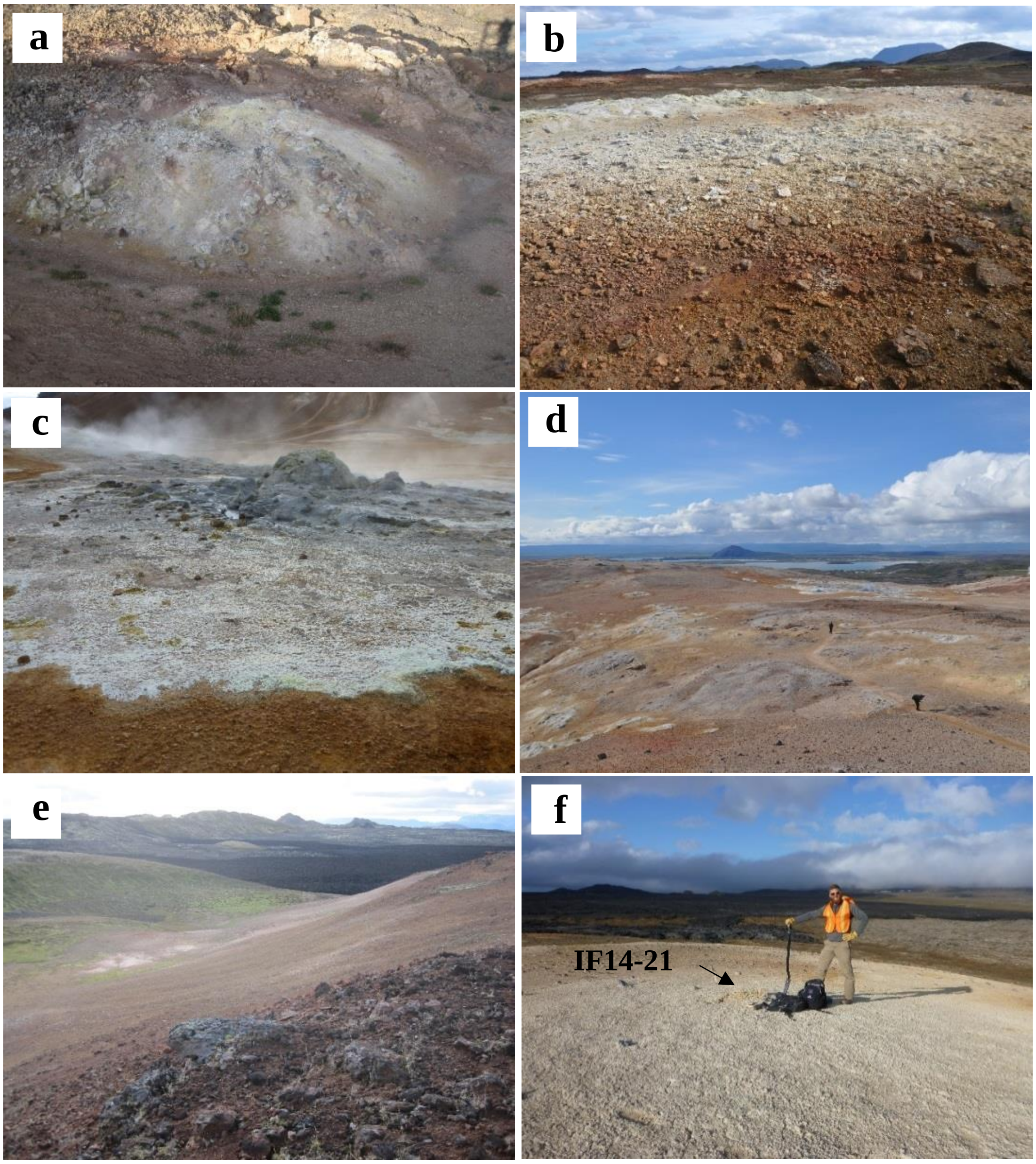

Figure 11: Diverse environmental settings across the Krafla and Námafjall geothermal areas. (a) Fumarole on the edge of the Mývatn Fires lava flow. (b) Large circular apron in the Hverir geothermal field, (c) mud pot in the Hverir geothermal field (d) fumaroles and mud pots at top of Námaskard form 'bulls-eye' alteration aprons, (e) bleached surface at Lítli-Leirhnjúkur, and (f) gypsum mound north of Leirhnjúkur.

Samples were collected across the geothermal fields in a variety of settings. For simplification, surface activity is divided into three categories based on the groups described by *Markússon and Stefánsson (2011)*. High activity areas include steam vents and mud pots with intense acid leaching. Medium activity areas are where the ground is hot but where steam vents and mud pots are uncommon and the surface alteration is less intense. Low activity areas are located along the margins of surface activity, with lower surface temperatures.

Geothermal waters were collected from hot springs, mud pots, and drainage channels to quantify the range of aqueous conditions. Dr. Brian Hynek of the University of Colorado collected condensates from fumaroles during our 2013 field expedition (see methods in *Hynek et al., 2013*). Water samples were filtered on-site through a 0.2 µm cellulose filter into 100 mL polypropylene bottles. Samples collected for major cation analysis were acidified with 10% HNO_3/1% HCl solution. Samples for anions were filtered only. Temperature and pH were measured using a temperature probe and pH paper, respectively. Additional measurements taken from each hot spring (mud pot) included specific conductivity, salinity, oxidation-reduction potential, and total dissolved solids (TDS) using a Hydrolab sonde. These samples were first placed into pre-contaminated glass bottles and allowed to cool <50°C prior to analysis.

4.2 Secondary mineralogy and geochemistry

Secondary alteration products were characterized using X-ray Diffraction (XRD), X-ray Fluorescence (XRF), and Scanning Electron Microscopy (SEM) equipped with an Energy-Dispersive Spectrometer (EDS) at the University of Wisconsin - Milwaukee. For

XRD analysis, samples were placed in aluminum trays to dry overnight. Alteration products were crushed and powdered dry using an agate mortar and pestle. Samples with more than one color were prepared as sub-samples of materials with a distinct color to identify its associated mineral assemblage. Where there was insufficient material to prepare each color separately, equal amounts of the various colors were powdered to achieve a representative bulk composition.

Figure 12: Dried samples in aluminum trays. These represent the sample types listed in Table 2. (a) Altered basalt, (b) white precipitate, (c) orange precipitate/sediment, (d) gray mud, (e) red sediment, (f) purple sediment, (g) clay-rich, (h) silica-rich, and (i) sulfur-rich.

Heat and water were avoided during sample preparation to avoid possible alteration or dissolution of highly soluble and hydrous minerals. Powdered samples (~1 g) were placed into a cavity mount and analyzed as random powders using a Bruker D8 Focus

XRD instrument (Cu Ka radiation, 1 s per 0.02° 2theta, 2°-60° range, Sol-X energy dispersive detector, methods of *McHenry, 2009*). The diffraction patterns were compared against the International Centre of Diffraction Data (ICDD) PDF-2 database using Bruker's EVA software.

For XRF analysis, powdered samples were placed in a drying oven overnight at 105°C and visually inspected for elemental sulfur crystallization (sulfur-rich samples were analyzed by pressed pellet). Loss on ignition (LOI) was determined by heating precisely weighed powdered samples (~1 g) to 1050°C in a muffle furnace for 15 minutes to allow the escape of all volatile components (e.g. hydrates in sulfate minerals). For fused beads, mixtures of 1.000 g of each sample, ~1 g of ammonium nitrate (oxidizer), and 10.000 g of a 50:50 lithium metaborate: lithium tetraborate flux with 1% LiBr a non-wetting agent were fused at ~1050°C in a Claisse M4 fluxer (methods of *McHenry, 2009*). Each bead was analyzed using a Bruker S4 Pioneer XRF. Concentrations of major and minor elements Si, Ti, Al, Fe, Mn, Mg, Ca, Na, K, P and trace elements Zr, Zn, Y, V, Sr, Ni, Nb, Ce, Cr, and Ba were determined using a calibration based on eleven USGS igneous and sedimentary rock standards. An element was considered detectable if the following criteria were met: its concentration was more than double the lower limit of detection and the statistical error was less than 12% or 2% for trace and major elements, respectively.

XRF pressed pellets were prepared for select altered and fresh samples to determine the concentrations of S, Cu, and select elements that were not analyzed or detected in the fused beads. Powdered samples (7.5 g) were placed in a drying oven overnight at 105°C. A mixture of 7.5 g of each sample with three GeoQuant "pills" (wax binder) was placed in the shatterbox for 30 seconds. Each powdered sample was placed into an aluminum Chemplex sample cup and loaded into Specac Atlas T25 press. Each sample was pressed using 25 tons of pressure for 1 minute. Each pressed pellet was analyzed using a Bruker S4 Pioneer XRF for major and minor elements Si, Ti, Al, Fe, Mn, Mg, Ca, Na, K, P and trace elements Zr, Zn, Y, V, Sr, S, Rb, Ni, Ga, Cu, Cr, and Ba using a calibration based on six USGS igneous and sedimentary rock standards, following the methods of *McHenry et al.* (2011). I followed the same detection criteria used for the fused beads.

Seven thin sections and small chips of fresh and altered basalt pieces were analyzed using a Scanning Electron Microscope (SEM) equipped with Energy-Dispersive X-Ray Spectroscopy (EDS). For these analyses, thin sections and small chips of altered basalt were carbon coated using an Edwards Coating System E306A and placed into the geologic thin section holder, and small chips of altered basalt were mounted on an aluminum stub and embedded in epoxy to expose a certain vesicle in-filling or exterior surface of interest. Samples were carbon coated and then analyzed using the S-4800 Hitachi at the University of Wisconsin – Milwaukee, using a cold cathode field emitter in secondary electron or backscattered electron mode with an accelerating voltage of 15 kV, 10 uA emission current, and high probe current. Elemental compositions were determined qualitatively using EDS analysis with Bruker software.

4.3 Geothermal waters

Thirteen water samples were analyzed for major cations using a Thermo iCE 3000 Series Atomic Adsorption Spectrometer using SOLAAR Series software. Major anions were analyzed using a single column Dionex ICS 1000 Ion Chromatograph with an AERS 500 Suppressor using a 4.5mM Na_2CO_3/1.4mM $NaHCO_3$ buffer solution. Silica was analyzed using a SEAL Analytical AA3 HR auto analyzer. Quantitative analysis was accomplished using a calibration curve from stock standards of each element provided by the UWM – School of Freshwater Sciences. For most samples, dilution was needed to fit the calibration curve. An electrical balance was calculated to determine the accuracy of analysis. Many samples had a significant electrical imbalance, which is assumed to be attributed to high Al concentrations (not analyzed) based on published results for another Icelandic hydrothermal system (*Kaasalainen & Stefánsson, 2012*). Aluminum is difficult to calibrate in solution due to its relative insolubility under near-neutral pH conditions. Inferred aqueous Al concentrations were calculated by charge balancing water samples to <5 %. Several samples were already charge balanced and thus do not include Al concentrations.

Elemental relative mobility (RM_i) of the water samples were calculated based on,

$$RM_i = ([i]/[ref])_{sample} / ([i]/[ref]_{basalt}$$

where ([i]/[ref]) is the concentration ratio of the i-th element of a water sample and the unaltered basalt. I selected Mg for the reference element in the water samples because it is a major element in both the basalts and water samples. Other studies have shown Mg to have high apparent mobility in low pH environments, which are present in the Krafla and Námafjall areas (*Markússon & Stefánsson, 2011; Kaasalainen & Stefánsson, 2012)*. Although alkaline geothermal waters are not present in this study area, Mg exhibits very low mobility due to the formation of Mg-rich clays (*Arnórsson et al., 1983*).

5. Results

5.1 XRD

Figure 13 shows fourteen representative XRD patterns that highlight the diversity in alteration mineralogy in the Krafla and Námafjall areas (see descriptions in Appendix E). Samples were collected around acid-sulfate fumaroles and hot springs (mud pots) at the surface and in shallow depth profiles (for more details, see Appendix C & D) that ranged in temperature from ambient to ~100°C and pH from 1.95 to 2.50. The most common minerals that resulted from reactions of high-iron basalts with acid-sulfate waters and/or vapors are (in alphabetical order) members of the alunite-jarosite group, anatase, goethite, gypsum, hematite, kaolinite, montmorillonite, and pyrite (Table 1). Some sulfate phases were observed in SEM and constrained using EDS. Results are categorized into groups that exhibit similar mineral assemblages, combined with surficial color and geochemical composition (see Table 2 & 4).

Hot spring (mud pot) acid-sulfate alteration produced three distinct mineral assemblages: (i) gray mud that includes pyrite/marcasite ± amorphous silica ± anatase ± kaolinite ± elemental sulfur, (ii) white surface precipitates that include halotrichite group ± Fe^{2+}-sulfates ± Ca/Mg-sulfates, and (iii) orange precipitates and underlying sediment that include alunite-jarosite ± hematite and/or goethite ± smectite ± alunogen. Other trace phases within each group are listed in Table 2.

Fumarolic alteration produced the following mineral assemblages: (i) SiO_2-rich soils that include amorphous silica ± anatase ± cristobalite ± quartz, (ii) purple sediments that include natroalunite- jarosite ± hematite ± amorphous silica ± kaolinite, and (iii) red sediments that include hematite ± goethite ± jarosite.

Along the margins of acid-sulfate fumaroles and hot springs are clay-rich sediments that include smectite ± kaolinite ± anatase ± hematite and/or goethite. At Krafla, an isolated mound north of Leirhnjúkur (currently non-thermal) possesses gypsum ± variscite ± kaolinite.

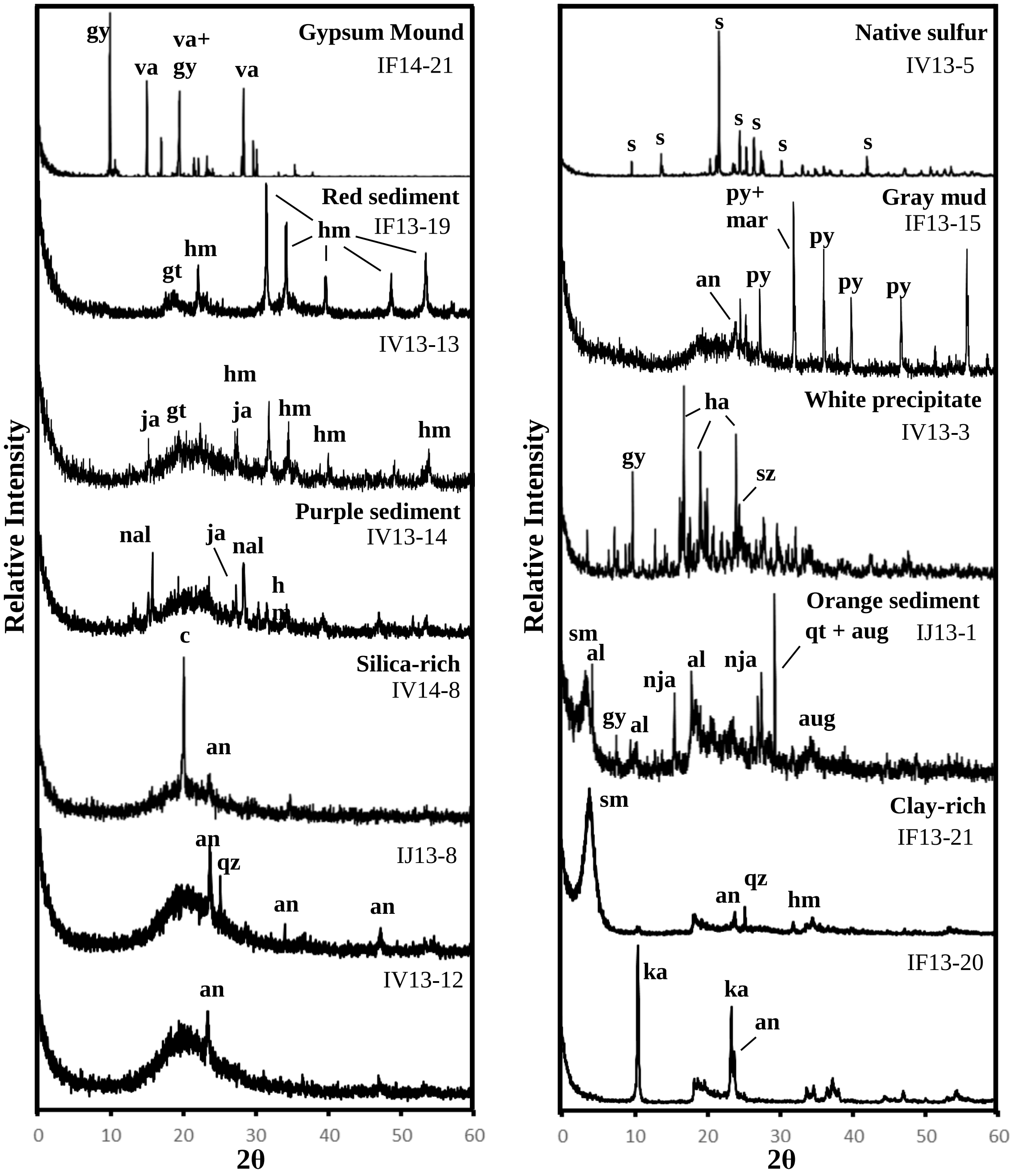

Figure 13: Representative XRD patterns from altered deposits from Krafla and Námafjall geothermal areas. A broad hump ~22° 2-theta is attributed to amorphous silica. Only major peaks have been labeled (for complete mineral list, see Appendix E). Augite (aug), alunogen (al), anatase (an), cristobalite (c), goethite (gt), gypsum (gy), halotrichite group (ha), jarosite (ja), kaolinite (ka), marcasite (mar), natroalunite (nal), natrojarosite (nja), pyrite (py), quartz (qz), smectite (sm), and szomolnokite (sz).

Table 1: *Alteration minerals identified associated with acid-sulfate waters*

Mineral	Formula	Occurrence	XRD	SEM
Kaolinite	$Al_2Si_2O_5(OH)_4$	Found in medium to high activity areas, often mixed with anatase, sulfates, and iron-oxides	X	
Halloysite	$Al_2Si_2O_5(OH)_4$	Found in samples with kaolinite	X	
Smectite	Variable	Found in greater abundances along the margins of activity	X	(X)
Amorphous Silica	am-SiO_2	Found throughout active surface with greater amounts in high activity areas	X	X
Cristobalite	SiO_2	Associated with am-SiO_2 adjacent to high temperature fumaroles	X	
Anatase	TiO_2	Is found in all samples. Higher % in areas of high activity	X	
Pyrite	FeS_2	Below oxidation front near hot springs	X	X
Marcasite	FeS_2	Below oxidation front with pyrite	X	
Hematite	Fe_2O_3	Above the oxidation front with alunite-jarosite and goethite along the margins	X	X
Goethite	$FeO(OH)$	Above the oxidation front in areas of low activity	X	
Variscite	$AlPO_4 \cdot 2H_2O$	Found in one sample in gypsum mound	X	
Zeolites	Variable	Found in areas of low activity	X	(X)

Sulfate minerals identified with acid-sulfate waters

Mineral	Formula	Occurrence	XRD	SEM
Alunite	$KAl_3(SO_4)_2(OH)_6$	Close to surface with am-SiO_2, hematite, and jarosite in medium to high activity areas	X	(X)
Natroalunite	$NaAl_3(SO_4)_2(OH)_6$	Similar to alunite.	X	X
Jarosite	$KFe^{3+}_3(SO_4)_2(OH)_6$	Medium to low activity areas with hematite and am-SiO_2	X	X
Natrojarosite	$NaFe^{3+}_3(SO_4)_2(OH)_6$	Same as jarosite; except more common at fumaroles	X	(X)
Alunogen	$Al_2(SO_4)_3 \bullet 17(H_2O)$	High to medium activity areas in white and orange surface precipitates	X	
Rozenite	$Fe^{2+}SO_4 \bullet 4(H_2O)$	Found with pyrite and white surface precipitates	X	
Szomolnokite	$Fe^{2+}SO_4 \bullet (H_2O)$	Found in white surface precipitates	X	
Halotrichite*	$(Fe^{2+},Mg)Al_2(SO_4)_4 \bullet 22H_2O$	Found at the surface in areas of high activity	X	
Rhomboclase	$HFe^{3+}(SO_4)_2 \bullet 4(H_2O)$	Proximal to high-temperature fumaroles	X	
Ferricopiapite	$Fe^{3+}_{2/3}Fe^{3+}_4(SO4)_6(OH)_2 \bullet 20(H2O)$	Found in one sulfur-rich sample	X	
Starkeyite	$MgSO_4 \bullet 4(H_2O)$	Found in one sample in white surface precipitates	X	
Epsomite	$MgSO_4 \bullet 7(H_2O)$	Found in one sample with starkeyite	X	
Gypsum	$CaSO_4 \bullet 2H_2O$	Forms large mounds and surface precipitates in areas of low and high activity, respectively	X	X
Barite	$BaSO_4$	Found in am-SiO_2 veins		X

(X) – tentative identification in SEM

* - Halotrichite group

Table 2: Mineralogical composition of each sample type found at Krafla and Námafjall geothermal areas[a]

Sample Type	Description	Major/Minor Phases[b,c]	Accessory Phases
Gray Mud	Near bubbling mud pots (T = ~60-100°C, pH ~2)	pyrite (M), amorphous silica (M), anatase (M), marcasite (m), elemental sulfur (m)	alunogen, kaolinite
White precipitate	Fibrous to acicular crystalline aggregates of yellowish white color found at the surface adjacent to an active mud pots and fumaroles (T = ~60-80°C)	halotrichite group (M), gypsum (m) szomolnokite (m), starkeyite (m)	elemental sulfur, epsomite, rozenite
Orange precipitate/ sediment	Small, pale orange bulbous crystalline aggregates often mixed into underlying loose, fine-grained brown sediment composed of remnant igneous phenocrysts, smectites, and zeolites (T= ~30-65°C)	alunite-jarosite (M), alunogen (m), smectite (m), goethite (m), quartz (m)	anatase, hematite, igneous
Sulfur-rich	Acicular crystals of native sulfur form near active steam vents. Often form large mounds (T = ~100°C)	elemental sulfur (M), anatase (m), amorphous silica (m)	-
Silica-rich	Loose, damp whitish-yellow fine-grained sediment with silica contents between ~60 to 86 wt. % (T= ~30-100°C)	amorphous silica (M), anatase (M), cristobalite (m), quartz (m)	kaolinite, hematite
Purple sediment	Dark purple altered basalt and loose sediments often mixed together with yellow, red, and orange particles around fumaroles	alunite-jarosite (M), hematite (M), amorphous silica (m), clays (m)	anatase, goethite
Red sediment	Brick-red, fine to clay-sized particles, with high total Fe content. Often found along the distal margins of surface activity	hematite (M), goethite (M)	alunogen, anatase, maghemite, natroalunite
Clay-rich	White-tan, Al-rich, clay-sized particles often mixed with specks of yellow, purple, and red. Widespread deposits along the margins of surface activity	kaolinite (M), smectite (M), alunogen (m)	anatase, jarosite, quartz

[a] Generalized mineral assemblage for each sample type

[b] M = major, m = minor

[c] includes different members of the alunite-jarosite group

5.2 XRF

Published and original data demonstrate the limited range in major element compositions of the Holocene basalts in the Krafla and Námafjall area (wt. %): SiO_2 48.8 -50.6, TiO_2 1.8-2.1, Al_2O_3 12.7-13.6, Fe_2O_3T 15.4-16.8, MgO 5.5-6.2, CaO 10.1-10.7 (n=16). Krafla basalt samples exhibit a high total iron wt. %, which is higher than a majority of other basalts on Earth and is consistent with some Martian basalts. Pleistocene hyaloclastites have notably higher Al_2O_3, CaO, MgO and lower Fe_2O_3T, TiO_2, Na_2O, and K_2O contents than the Holocene basalts (Table 3).

Bulk compositions of loose sediments and altered basalt are listed in Table 4. The results show major variations in composition relative to the unaltered basalt under geothermal conditions of up to 100°C, ranging from compositions similar to fresh basalt to those composed of mostly silica (Figure 14). Alteration samples related to acid-sulfate waters and/or vapors show SiO_2 concentrations ranging from 20-86 wt. %. All samples show a decrease in CaO, MgO, MnO, and Na_2O and increased concentrations of sulfur and TiO_2. Phosphorous showed limited variability, with depletion in some cases and enrichment in the medium to low activity areas. Potassium, in general, showed a slight decrease in concentration, while it showed enrichment in two samples, which coincided with elevated iron content and the presence of the K and Fe bearing sulfate mineral jarosite. Al_2O_3 and Fe_2O_3T showed significant variability across the geothermal area, ranging in concentration from 3-31 wt. % and <1-50 wt. %, respectively. TiO_2 concentrations range considerably in acid-sulfate environments between 2-23 wt. %. Sulfur concentrations in the surface precipitates fell beyond our calibrated range and could not be accurately measured, whereas others showed less elevated concentrations

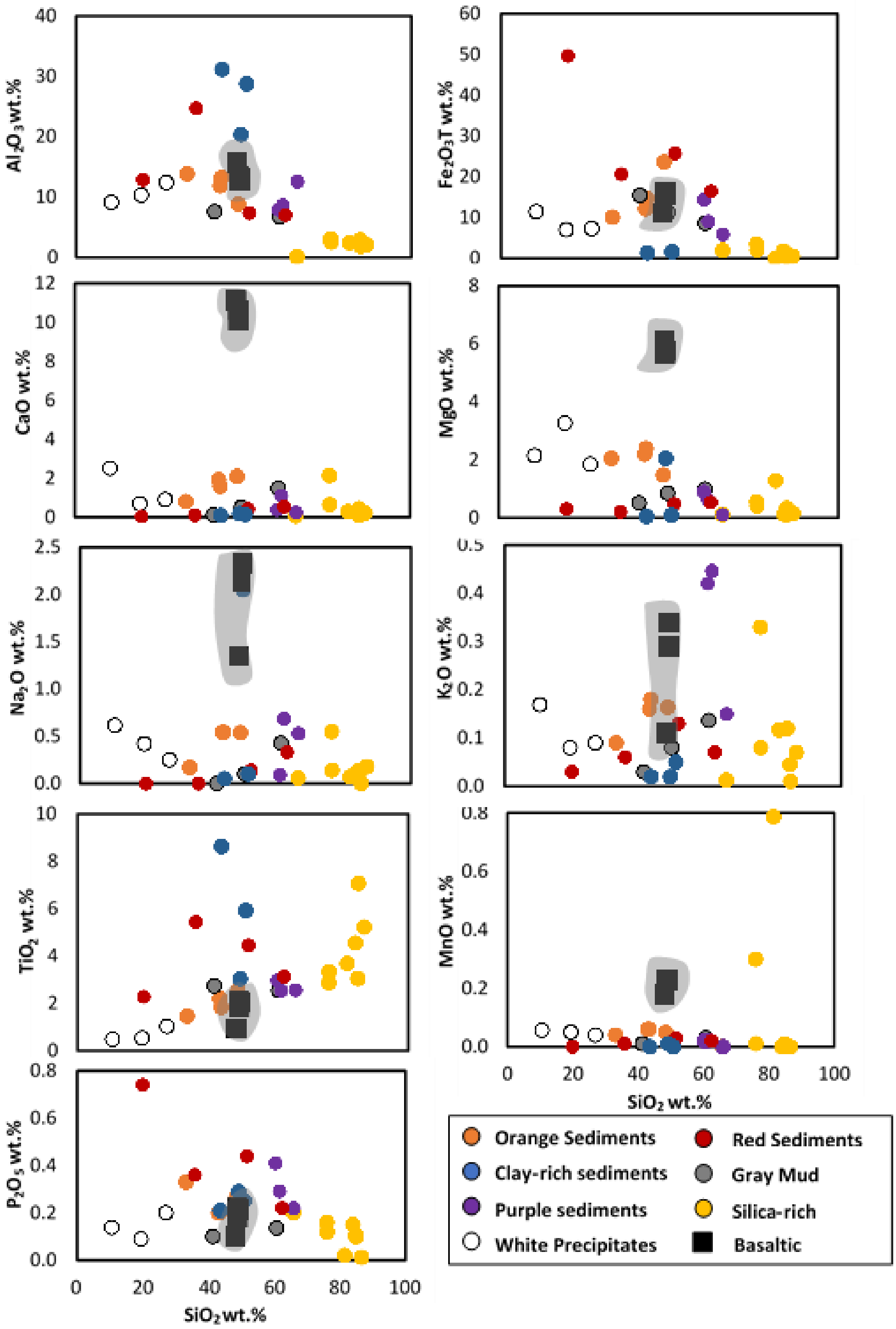
Al_2O_3 wt.%
40
30
20
10
0
Fe_2O_3T wt.%
60
50
40
30
20
10
0
CaO wt.%
12
10
8
6
4
2
0
MgO wt.%
8
6
4
2
0
Na_2O wt.%
2.5
2.0
1.5
1.0
0.5
0.0
K_2O wt.%
0.5
0.4
0.3
0.2
0.1
0.0
TiO_2 wt.%
10
8
6
4
2
0
MnO wt.%
0.8
0.6
0.4
0.2
0.0
P_2O_5 wt.%
0.8
0.6
0.4
0.2
0.0
0
20
40
60
80
100
SiO_2 wt.%
Orange Sediments
Red Sediments
Clay-rich sediments
Gray Mud
Purple sediments
Silica-rich
White Precipitates
Basaltic

Figure 14: Harker diagrams showing the relationship between major elemental composition of the alteration products at Krafla and Námafjall area. Composition of unaltered basaltic substrate is shaded for comparison. All altered products from mud pots and fumaroles had lower Ca, Mg, Mn, and Na compared to an unaltered substrate. Fe, Al, and P exhibited significant variation, but had elevated concentrations in the red, purple, and orange sediments. Clay-rich samples had the highest Al concentrations. K had lower concentrations in most samples, although in the purple sediments were enriched. Ti is enriched in most samples.

that ranged from 0.2-7 wt. %. Zirconium and vanadium are the most abundant trace elements in the alteration samples.

Most samples had high H_2O contents (likely from hydrated sulfate minerals or clays), indicated by the high loss on ignition (LOI) values up to ~53 wt. % in the precipitates and ~12 wt. % in loose alteration sediments (see Table 4).

Table 3: Major element composition of Martian basalts and other analogs compared to basalts from the Krafla and Námafjall areas[a]

Oxide (wt %)	1975-84 Eruption	1724-29 Eruption	> 6100 ka Eruption	Hyaloclastite	Mauna Kea[b]	Cerro Negro[c]	OCBP1[d]	Adirondack[e]	Jake_M[f]
SiO_2	49.00	48.80	48.80	48.10	48.70	48.40	48.19	45.30	51.85
Al_2O_3	12.84	12.70	13.10	15.70	17.40	17.70	8.06	10.40	16.51
Fe_2O_3T	16.27	15.80	15.50	11.20	12.00	9.90	20.23	21.10	7.50
MnO	0.20	0.18	0.18	0.14	0.21	0.20	0.43	0.42	0.14
MgO	5.76	5.70	6.10	9.30	3.90	6.70	10.40	11.90	3.71
CaO	10.13	10.10	10.60	8.10	6.60	11.90	6.46	7.80	6.23
Na_2O	2.33	2.30	2.10	1.40	4.30	2.00	2.19	2.10	6.47
K_2O	0.34	0.34	0.29	0.11	1.90	0.40	0.75	0.03	2.27
TiO_2	2.06	2.00	1.80	0.94	2.80	0.70	1.01	0.49	0.51
P_2O_5	0.21	0.22	0.18	0.10	0.85	0.09	1.37	0.54	0.51
S	-	0.04	0.04	0.06	0.09	0.03	-	-	-
LOI	-	0.25	-0.62	2.30	1.60	-	-	-	-
Total	99.26	98.15	98.92	99.15	99.83	99.90	97.38	99.81	-

[a] Bulk compositions of basalts determined by X-ray fluorescence, this study

[b] Mauna Kea (*Morris et al., 2005*), [c] Cerro Negro (*Hynek et al., 2013*)

[d] OCBP1 (Meridiani) (*Morris et al., 2006*), [e] Adirondack (*McSween et al., 2006*), [f] Jake_M (*Gellert et al., 2013*).

Total Fe reported as Fe_2O_3. “-” = not determined. LOI=loss on ignition, where applicable.

Table 4: Chemical composition of alteration products from the Krafla and Námafjall areas

Category	Sample	SiO2	TiO2	Al2O3	Fe2O3	Mn	MgO	CaO	Na2O	K2O	P2O5	S	LOI	SUM
White precipitates	IV13-3	10.51	0.50	9.10	11.40	0.06	2.15	2.52	0.61	0.17	0.14	x	53.30	90.51
	IF13-12	26.97	1.04	12.40	7.24	0.04	1.85	0.91	0.25	0.09	0.20	x	47.66	98.72
	IF13-22	19.45	0.54	10.32	6.97	0.05	3.27	0.70	0.42	0.08	0.09	x	49.09	91.04
Orange precipitates/ sediments	IV13-4	48.47	2.57	8.80	23.66	0.05	1.48	2.11	0.54	0.16	0.27	1.12	9.37	97.60
	IF13-14	33.16	1.47	13.84	10.04	0.04	2.05	0.81	0.17	0.09	0.33	x	39.94	102.04
	IJ13-1	42.99	2.20	11.84	12.13	0.06	2.20	1.93	0.54	0.16	0.20	6.15	23.79	98.15
	IF13-6	43.41	1.83	13.23	14.60	0.06	2.39	1.60	0.54	0.18	0.20	3.28	17.20	95.38
Gray mud	IV13-2	60.70	2.56	6.71	8.57	0.03	0.99	1.49	0.43	0.14	0.14	6.86	14.17	96.02
	IF13-15	49.67	2.17	14.21	11.19	0.01	0.86	0.53	0.10	0.08	0.20	5.31	18.07	97.22
	IF13-17	41.31	2.74	7.56	15.47	0.01	0.52	0.13	0.00	0.03	0.10	7.86	10.98	95.05
Silica-rich soils	IJ13-8	86.66	5.22	2.04	0.51	0.00	0.16	0.22	0.18	0.07	0.01	0.62	3.95	99.24
	IJ13-9	84.01	4.55	2.38	1.74	0.00	0.13	0.24	0.13	0.12	0.15	0.56	4.43	97.98
	IV13-6	84.93	7.06	1.85	0.31	0.00	0.11	0.09	ND	0.01	0.10	0.19	3.96	98.51
	IV13-8	65.90	23.05	0.09	1.94	0.00	0.12	0.08	0.06	0.01	0.20	0.24	5.03	98.52
	IV13-9	81.52	3.68	2.41	0.02	0.79	1.29	0.30	0.07	0.12	0.02	0.27	4.76	97.77
	IV13-12	84.81	3.05	2.88	1.07	0.01	0.33	0.45	0.14	0.05	0.11	1.00	5.54	96.74
	IF13-5	75.98	2.87	3.06	3.43	0.30	0.56	2.15	0.55	0.33	0.16	x	8.59	97.76
	IF13-7	76.07	3.34	2.50	1.98	0.01	0.41	0.65	0.14	0.08	0.12	2.58	11.78	97.15
Purple sediments	IF13-18	60.38	2.97	7.87	14.37	0.02	0.91	0.39	0.09	0.42	0.41	1.29	11.12	98.64
	IJ13-10	65.97	2.56	12.53	5.82	0.00	0.11	0.25	0.53	0.15	0.22	1.75	9.98	98.24
	IV13-14	61.62	2.54	8.63	9.00	0.02	0.63	1.10	0.68	0.45	0.29	x	10.15	97.04
Red sediments	IF13-13R	35.80	5.43	24.68	20.63	0.01	0.21	0.10	ND	0.06	0.36	x	11.03	98.56
	IF13-19	19.97	2.28	12.85	49.66	0.00	0.30	0.05	ND	0.03	0.74	0.86	11.12	97.26
	IJ13-7	62.45	3.12	7.00	16.45	0.02	0.54	0.56	0.33	0.07	0.22	0.86	7.12	97.98
	IF13-9	51.71	4.45	7.31	25.69	0.03	0.48	0.42	0.14	0.13	0.44	0.54	7.69	98.68
Clay-rich	IF13-13W	50.85	5.92	28.77	1.56	0.00	0.10	0.15	ND	0.05	0.25	x	11.46	99.38
	IF13-20	43.56	8.63	31.12	1.30	0.00	0.05	0.11	ND	0.02	0.21	0.77	13.61	98.80
	IF13-21	49.19	3.04	20.35	14.31	0.01	2.05	0.19	ND	0.02	0.29	x	7.97	97.63

Major elements (wt. %), trace elements (ppm), ND = Not detected, “x” = Not measured

Table 4 cont.

Category	Sample	Zr	Zn	V	Sr	Ni	Cu	Cr	Ba
White precipitates	IV13-3	344	53	252	54	ND	ND	91	ND
	IF13-12	73	40	220	47	31	ND	140	ND
	IF13-22	35	37	213	ND	77	ND	239	ND
Orange precipitates/ sediments	IV13-4	138	80	533	96	37	132	140	69
	IF13-14	98	53	205	80	46	ND	218	63
	IJ13-1	130	83	358	116	32	136	133	58
	IF13-6	127	83	376	102	52	150	142	ND
Gray mud	IV13-2	160	28	257	92	22	104	98	82
	IF13-15	160	40	249	87	50	156	243	126
	IF13-17	183	ND	215	49	78	130	118	58
Silica-rich soils	IJ13-8	279	ND	211	66	ND	22	108	260
	IJ13-9	256	ND	244	120	ND	19	113	219
	IV13-6	351	80	533	ND	ND	86	112	58
	IV13-8	1343	ND	570	ND	ND	41	346	309
	IV13-9	207	ND	156	ND	ND	29	89	309
	IV13-12	183	ND	87	ND	ND	ND	61	309
	IF13-5	184	33	174	31	ND	ND	ND	151
	IF13-7	191	ND	154	35	ND	38	50	69
Purple sediments	IF13-18	209	ND	633	43	18	67	138	186
	IJ13-10	154	ND	467	158	ND	37	174	139
	IV13-14	150	ND	364	233	ND	ND	130	170
Red sediments	IF13-13R	362	ND	727	188	ND	ND	426	172
	IF13-19	148	48	1586	45	9	53	285	117
	IJ13-7	171	ND	495	73	ND	88	157	241
	IF13-9	269	70	894	87	ND	67	200	141
Clay-rich	IF13-13W	417	ND	405	262	ND	ND	546	374
	IF13-20	595	ND	549	73	21	276	380	164
	IF13-21	190	88	1089	ND	56	ND	608	ND

Major elements (wt. %), trace elements (ppm)
ND = Not detected, “x” = Not measured

5.3 SEM/EDS

SEM/EDS analysis supported by XRD phase identification provided a detailed geochemical and mineralogical analysis for altered rocks from four distinct alteration groups: (i) silica-rich soils (IV13-7), (ii) purple sediments (IV13-14), (iii) red sediments (IV13-13), (iv) and a slightly altered basalt along the distal margin (IV13-11) (additional images are shown in appendix B). These samples were collected from the Late Holocene basalt field in a large fumarolic apron within the Námafjall area. Examination of the interior of altered high-Fe basalt shows varying degrees of alteration of primary igneous textures and the precipitation of secondary minerals.

Silica-rich soils and colored-sediments showed extensive alteration and possessed little to no remaining primary phenocrysts, which were completely or partially replaced by amorphous silica. In one instance, a very small section of primary minerals remained and exhibited extensively etched surfaces along augite and plagioclase crystals (Figure 15). EDS results showed relict plagioclase laths with Al and Si, while mobile elements Ca or Na were depleted. Along the margins, primary igneous textures were unaltered. Titanomagnetite retained its skeletal and cruciform texture, but with a notable depletion in Fe (referred to as ‘ghost’ texture by *Urcia et al., 2010*). In one instance, FeOx spherules are observed near the cruciform texture of titanomagnetites (Figure 16). Other FeOx minerals identified by XRD include magnetite ($Fe^{2+}Fe^{3+}2O_4$) and maghemite (γ–Fe_2O_3). Both are likely secondary in nature, formed during alteration of titanomagnetites, since the primary igneous oxides analyzed by EDS had significant Ti concentrations.

Basaltic glass is completely absent in the silica-rich soils, whereas abundant sideromelane with etched surfaces and replaced by amorphous silica and possibly clays and iron oxides/hydroxides is observed in the colored sediments (Figure 17c,d). In Figure 17c, the dark layer near the rim of the sideromelane fragments represents palagonite, i.e. poorly crystalline smectite-like material. In other cases, altered fragments showed distinct repetitive compositional layering. These are considered relict sideromelane fragments based on the sharp, uneven morphology and their close association with other sideromelane fragments (Figure 17a,b).

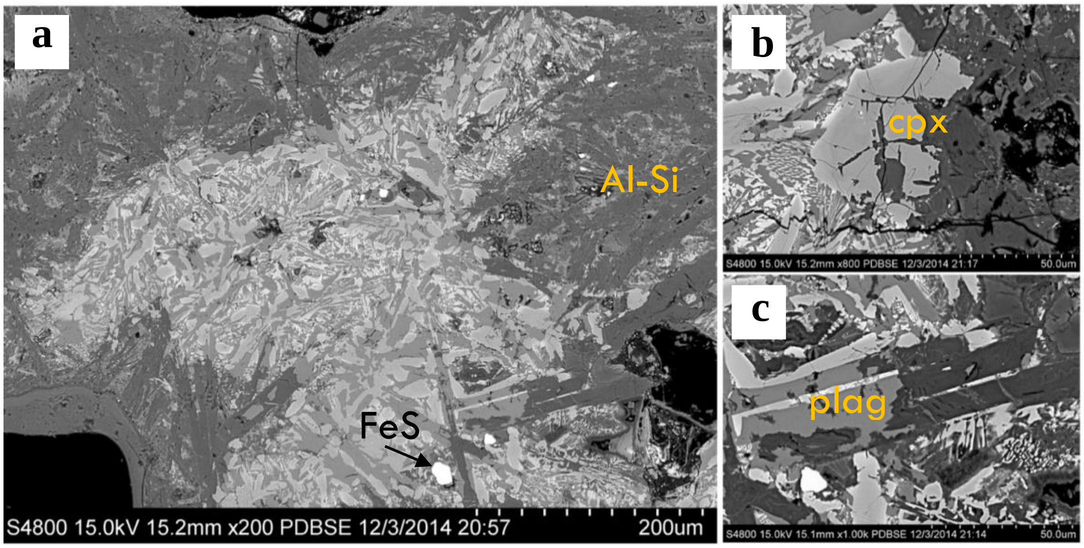

Figure 15: SEM image of a heavily altered basalt within silica-rich soils (sample IV13-7). (a) Small section of primary minerals in a highly leached basalt; Fe-S mineral is tentatively identified as pyrite. (b) Altered clinopyroxene (augite) and (c) plagioclase leached of mobile elements (e.g. Ca, Na) and replaced by amorphous alumino-silicate.

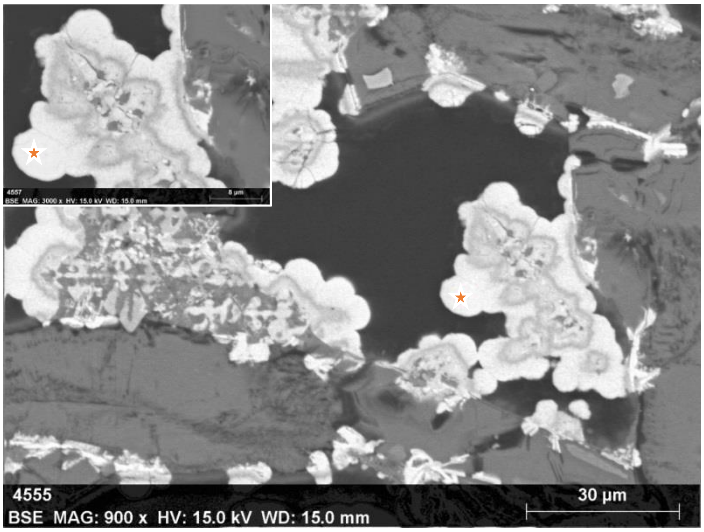

Figure 16: Altered titanomagnetite crystals (sample IV13-7). Botryoidal growth of Fe-oxide spheroids forming in close association with titanomagnetite. Star represents dot analysis using EDS. Insert shows an expanded view. EDS elemental data at the orange star shows high levels of Fe and O with trace amounts of Si, P, and S.

In EDS, the bright layers have a larger proportion of Ti compared to Fe. These relict grains are surrounded by FeOx spherules and amorphous silica. Samples collected along the margins had vesicles filled with altered basaltic glass shards (i.e. sideromelane) rather than amorphous silica. Here, these basaltic glass fragments were lined with an Al-Si material with varying amounts of Fe, Mg, Ca, and S, likely a smectite with varying compositions and/or zeolites based on the XRD results.

Secondary minerals observed in SEM were commonly associated with amorphous silica (Figure 18). The most frequently observed secondary minerals were members of the alunite-jarosite group and hematite. A microscopic needle-like barium and sulfur bearing mineral, presumably barite, was sparsely distributed in amorphous silica veins and surface coatings (Figure 18a). In addition, gypsum, pyrite, and an unidentified Al and Au-bearing material were found in amorphous silica veins (Figure 18b-d). XRD patterns did not show evidence for barite or pyrite, perhaps due to their minor abundance.

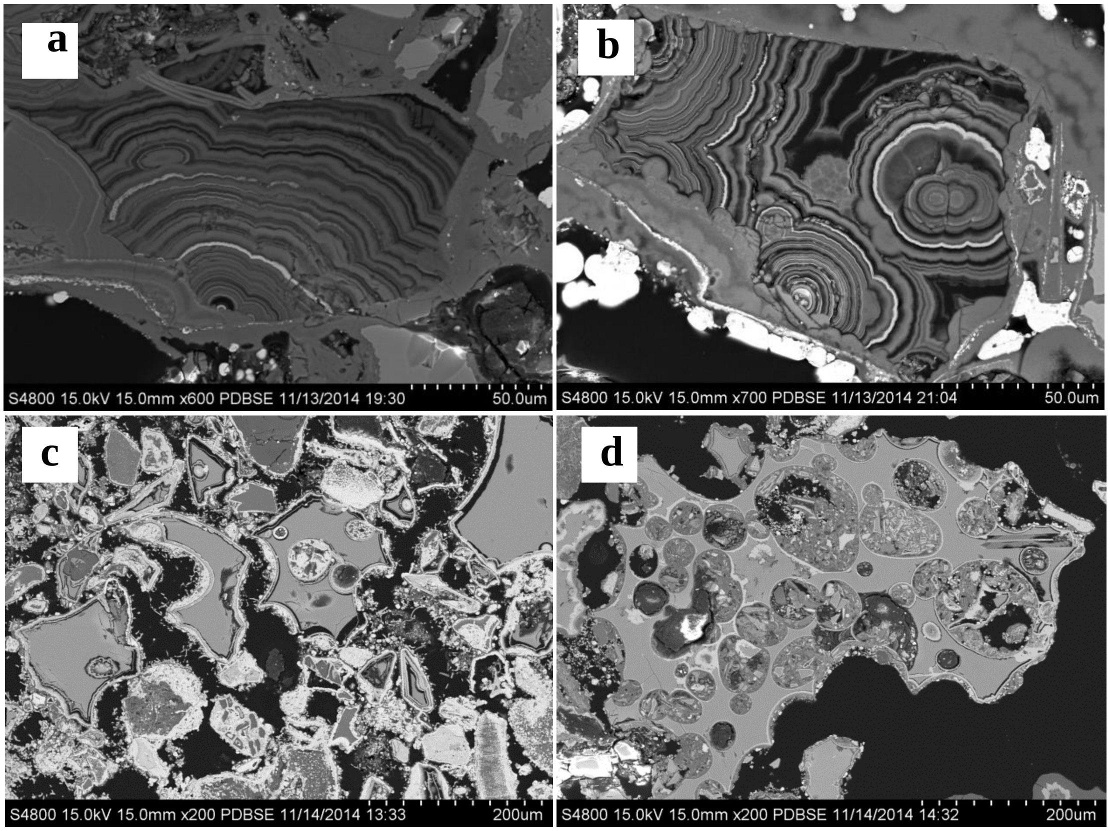

Figure 17: SEM image of altered basaltic glass fragments from sample IV13-13. (a+b) Relict grain boundaries exhibit oscillating layers (c+d) Sideromelane fragments altered to Fe-hydr(oxides) and clays.

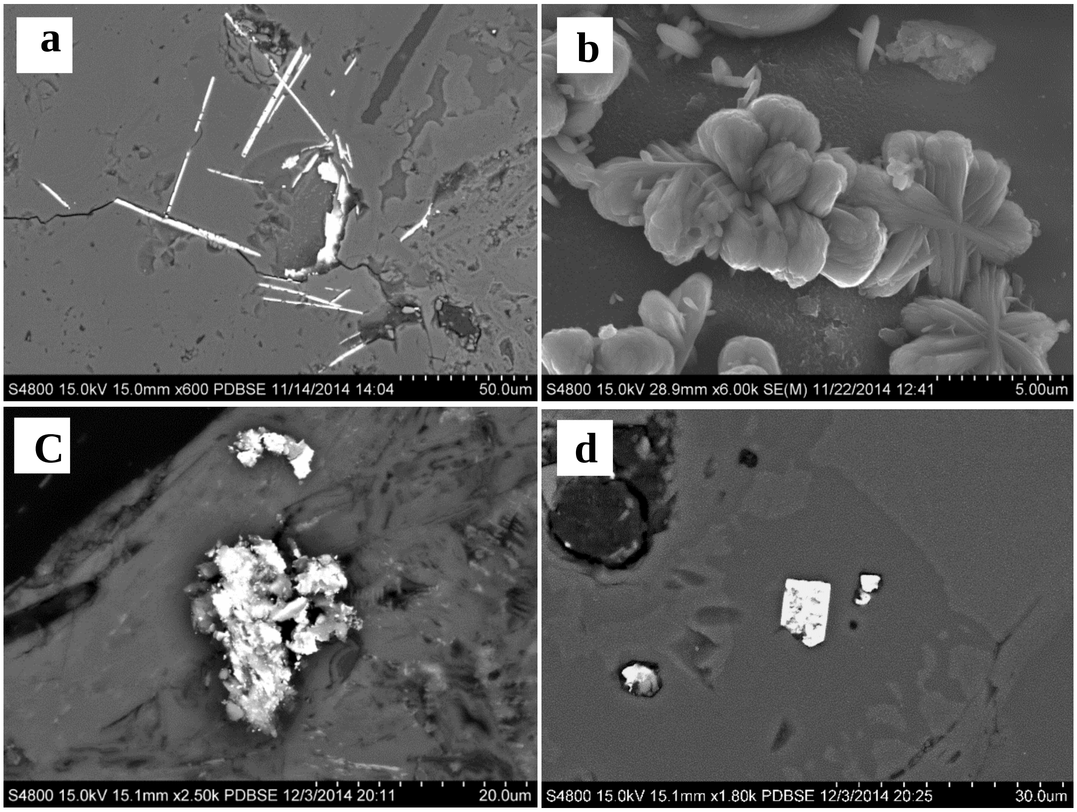

Figure 18: SEM image of secondary minerals identified in amorphous silica veins. (a) Needle-like barite crystals and (b) authigenic gypsum exhibits bladed star-shaped crystals on an amorphous silica spheroid from sample IV13-13. (c) Al and Au-bearing grain with trace amounts of Cr, Ti, and Fe and (d) pyrite cube with a dissolved interior from sample IV13-12.

5.4 Aqueous Geochemistry

The composition of selected geothermal surface waters at Krafla and Námafjall are provided in Table 5. Twelve water samples were analyzed from the most acidic geothermal features (e.g. acid pools, mud pots, drainage channels, etc.), which are classified as steam-derived acid-sulfate waters, although mixed waters were also present in thermal and non-thermal pools. The water pH ranged from 1.96-6.40 at measured temperatures between 13-92°C.

Steam-derived acid-sulfate waters had pH values most commonly between 2.0 – 2.5. Acidity is controlled by the oxidation of H_2S to sulfate, resulting in a decrease in pH values. The oxidation of dissolved sulfide proceeds slowly through SO_3^{2-} and $S_2O_3^{2-}$ and eventually to sulfate. Intermediate oxidation states are unstable in acidic waters and rapidly oxidize in the presence of pyrite, which is a common alteration product in acid pools and mud pots (*Kaasalaninen & Stefánsson, 2011*). Additional acid is generated by the oxidation of elemental sulfur in the following reaction:

$$S^0 + 1.5O_2 + H_2O \rightarrow 2H^+ + SO_4^{2-}$$

Floating pyrite and elemental sulfur were commonly associated with acid sulfate pools and mud pots, suggesting that dissolved sulfur was lost to the formation of sulfur-bearing minerals. H^+ concentrations are typically higher than transition metal cations in solution, and rock dissolution buffered the pH by consuming protons during water-rock interactions. This process is analogous to an acid-base titration, where H^+ ions are consumed by the basalt, which subsequently releases cations into solution. The pH is also buffered by the second dissociation constant of sulfuric acid (HSO_4^-/SO_4^{2-}) (*Kaasalainen & Stefánsson, 2012*).

Geothermal fluid compositions exhibit significant variability but, in general, major cations showed a decrease in abundance in the following order: SiO_2, Fe^{2+}, Al^{3+}, Ca^{2+} ~ Mg^{2+}, Na^{+}, K^{+}, although the inferred Al^{3+} concentration varied substantially between water samples. The inferred elevated Al^{3+}concentrations correspond to the highest sulfate concentrations in mud pots (up to 425 mg/l), and seem reasonable based on results of previous and similar studies (up to ~1100 mg/l) (*Hynek et al., unpublished; Kaasalainen & Stefánsson, 2012).* In general, the greatest cation abundances are found at mud pots compared to acid pools, discharge streams, and condensed vapors.

Acid-sulfate waters are dominated by sulfate anions, ranging from 398 to 3800 mg/l. In general, the highest sulfate concentrations were found at Námafjall compared to Krafla, in particular, the Hverir mud pots ranged from 3801-3819 mg/l and had the highest specific conductivity (6163 ųs/cm) and salinity (3.41 ppt) analyzed in the field. Differences in dissolved sulfate concentrations may be the result of the differences in gas chemistry between the two geothermal areas (e.g. *Ármannsson, 1993*). Additionally, it may be a function of the fumarole discharge intensity, where higher discharge rates transport more dissolved species in solution to the surface, rather than diffusing out into the altered deposits. Chlorine is depleted (<2 mg/l) compared to local source water due to its high mobility during the alteration process and steam condensate dilution (*Arnórsson & Andrésdóttir, 1995, Kaasalainen & Stefánsson, 2012*). Nitrate is found in minor concentrations (<9 mg/l).

In-Situ Environmental Parameters

Sample	T°C	pH	SpCond (ųs/cm)	Sal (ppt)	ORP (mV)
F14-1	88	2*	-	-	-
F14-11	73	2.3	1441	0.76	-368
F14-12	38	2-2.3	-	-	-
F14-15	26	2*	5723	3.16	-313
F14-16	74	2.5	-	-	-
F14-18	13	2*	-	-	-
F14-29	92	2.4	3477	1.89	-239
V14-1	40	2.15	6163	3.41	-56
V14-4	59	2.42	2109	1.13	-136
V14-5	66	2.2	4024	2.19	-343
V14-23	56	2.24	4241	2.32	-269
V14-29	71	2.36	1456	0.77	-302

Dissolved Ions (mg/l)

Sample	SiO_2	Na	K	Ca	Mg	Fe	Al	Cl^-	$SO4^{2-a}$	$NO3^-$
F14-1	233	5.08	0.33	31.4	31.8	107	*17*	0.51	1068	2.82
F14-11	163	2.67	BD	8.8	15.6	84	*x*	0.18	696	1.97
F14-12	177	3.46	0.63	31.2	30.9	204	*186*	0.64	2240	5.58
F14-15	220	3.99	1.15	31.1	34.4	184	*202*	0.54	2310	5.82
F14-16	210	1.86	BD	15	24.3	32	*33*	0.16	572	1.62
F14-18	232	3.91	0.91	30.9	36.8	184	*214*	0.63	2396	6.17
F14-29	253	12.49	0.94	78.9	55.9	134	*141*	0.5	1777	4.02
V14-1	246	24.27	2.24	107.9	82.4	122	*425*	0.38	3819	8.7
V14-4	197	63.37	6.23	90.9	19.4	14.6	*28*	1.82	872	3.69
V14-5	228	15.45	3.36	65.1	53.6	196	*450*	1.52	3801	8.83
V14-23	232	6.92	0.33	85.3	40.1	149	*194*	0.28	2150	5.78
V14-29	253	3.05	0.19	13.9	9.5	9.7	*x*	0.14	398	1.35

*pH measured by pH 2-2.3 strips

"-" not measured, "BD" = Below Detection

Table 5: *In-situ* environmental parameters and dissolved ion chemistry of water samples from the Krafla and Námafjall/Hverir area. Temperatures at time of collection measured using a thermometer, pH measured by Hydrolab sonde unless otherwise indicated, and Specific Conductivity (SpCond), salinity (sal), and oxidation reduction potential (ORP) measured using the Hydrolab sonde. BD = below detection. Al concentrations are inferred based on charge balance calculations. [a]Total sulfur (SO_4^{2-} + S^{2-}) reported as sulfate.

6. Discussion

6.1 Geothermal Alteration and Element Mobility

Surface volcanic areas are open systems, where volcanic vapors ascend and mix with oxygenated ground and surface waters. The production of sulfuric acid promotes the dissolution of crystalline basalt and hyaloclastite, which controls the geochemical composition of alteration products in the Krafla and Námafjall area.

One of the major constituents controlling the rate and dissolution of petrogenic elements is the primary mineral assemblage. Basaltic glass (i.e. sideromelane fragments) is very reactive (e.g. *Stroncik & Schminke, 2001*), while the dissolution of primary igneous minerals is based on their stability under aqueous acid-sulfate conditions in the following order (most reactive to least reactive): olivine > titanomagnetite > plagioclase > clinopyroxene (*Stefánsson, 2001*). It should be noted that the stability of titanomagnetite is sensitive to the Ti composition (higher Ti implies lower stability under the same chemical-physical conditions). Sulfuric acid promotes the dissolution of primary igneous phases (including basaltic glass) and the mobilization of cations that result in the progressive depletion of all major elements, except Si and Ti.

Highly elevated concentrations of dissolved metals such as Si, Al, Fe, and other metals in the acidic geothermal fluids reflect the significant contribution of water-rock interactions and acid leaching of the basaltic substrate. These elevated concentrations of major-rock forming elements (e.g. Ca, Mg) were related to pH, where higher acidity resulted in greater cation abundances. In the most acid waters, fluid compositions correspond well to unaltered basalt and hyaloclastite compositions, suggesting that pristine substrate dissolves nearly stoichiometrically with respect to major rock-forming elements in geothermal waters with a pH <2.5. These trends are related to the increased solubility of Fe- and Al-bearing minerals under low pH conditions (*Markússon and Stefánsson, 2011*).

Metal concentration may also be affected by the dissolution of soluble secondary minerals. For example, a localized high-temperature mud pot (IF-14-11) at Leirhnjúkur had significantly lower cation abundances compared to its associated discharge channel (IF-14-15, -18). The increased Fe, Al, and SO_4 concentrations correspond well to the composition of a variety of soluble sulfate phases (e.g. halotrichite group) that were observed along the margins of the channel, suggesting that the breakdown of secondary minerals may also contribute to dissolved ion concentrations.

The relative elemental mobility (RM_i) of selected geothermal water samples are shown in Figure 19. All major elements have high mobility in steam-derived acid-sulfate waters with pH <2.5 in a variety of aqueous environments such as mud pots, acid pools, drainage channels, and steam condensates. Fe, Al, and K exhibited the highest mobility in the most acid waters. Interestingly, these elements have the highest concentrations in high –temperature fumarolic gas emissions (*Hynek et al., unpublished*). For example, $Al^{3+} >> Ca^{2+}$ in low pH fumaroles and may support its high mobility in the most acidic geothermal fluids and vapors (e.g. *Hynek et al., 2013*). Previous studies have shown Al mobility to decrease rapidly with increasing pH, attributed to the formation of kaolinite in areas of medium to low activity (*Markússon and Stefánsson, 2011*). This study also confirms that kaolinite is a major alteration product in medium to low activity areas, and that Al mobility decreases with increasing pH. Basalt alteration in mildly acid to neutral waters is regarded as an incongruent process. In other words, mobile elements are

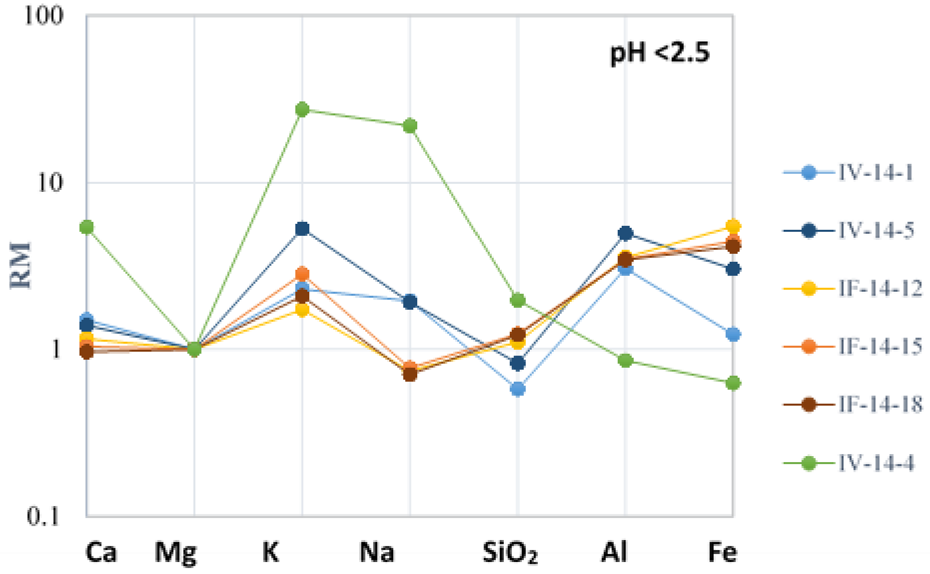

Figure 19: The relative mobility (RM) of elements in water samples with respect to Mg under pH values <2.5. An RM value of 1 indicates that the element has the same mobility as Mg, while below and above indicate relative depletion and concentration, respectively. Most elements exhibit high mobility compared to Mg in mud pots (blue: IV-14-1, -5), acid pools (yellow: IF-14-12), drainage channels (orange: IF-14-15, -18), and condensed steam (green: IV-14-4).

preferentially released according to composition and stability of the primary minerals present in the basaltic substrate.

The dissolution of the primary igneous phases (including basaltic glass) preferentially depleted the elements Mg, Mn, Ca, and Na in the least altered basalts, followed by Al, Fe, and K with increasing extent of alteration. Magnesium, Ca, and Na exhibited similar behavior and were greatly depleted, even along the margins in the more smectite-rich areas. For example, Ca decreased from 10 wt. % in fresh basalts to <1 wt. % in the most extensively altered basalts. In several samples, a slight increase in Ca content in areas of high surface activity was attributed to the formation of gypsum. Sodium concentrations had significant depletion down to 0.1-0.5 wt. % and were below the detection level for several samples. The highest Na and K concentrations coincided with elevated Fe content and the formation of natroalunite ($NaAl(SO_4)_2(OH)_6$) and jarosite ($KFe(SO_4)_2(OH)_6$).

Overall, Al and Fe showed substantial variability in loose sediments and altered basalts across both geothermal areas. Fe mobility was lower in the purple, red, and orange sediments in lower activity areas. In one instance, Fe is concentrated up to ~49 wt. % in a hematite and goethite-rich sample (e.g. red sediments, F13-19). In addition, siderophile elements V and Cr were also enriched with elevated Fe content. Al was strongly depleted in siliceous fumarolic deposits in areas of moderate to high surface activity, with minor concentrations of Al found in relict altered silicate minerals. Kaolinite was present in minor abundances in active high-temperature mud pots and became more dominant in areas of medium to low activity, exhibiting an increase in Al content. Clay-rich sediment along the distal margins of surface activity had the highest aluminum concentrations, which vary between ~12 to 31 wt. %. Al mobility is limited in these areas since it is a constituent of kaolin and smectite clays such as montmorillonite, nontronite, and saponite identified in XRD. These observations are consistent with the smectite compositions identified by *Mínguez et al.* (2011) in the Námafjall area.

Silica is the most abundant residually enriched element in alteration products from areas of high surface activity, often in the form of amorphous silica. Cristobalite and secondary quartz are also observed. Fumarolic (low water-rock) alteration resulted in the highest SiO_2 enrichment (concentrations of up to 86 wt. % compared to 48 wt. % in pristine basalts), while silica enrichments near hot springs were less pronounced (~60 wt. %). Residually enriched silica was always accompanied by enriched TiO_2 and Zr.

Alteration products exhibited high residual TiO_2 contents relative to pristine basalts (~2 wt. %). Titanomagnetite is the main precursor phase for the Ti and through acid-sulfate alteration forms anatase. Hot spring deposits exhibited only minor enrichments (up to 2.74 wt. %), while siliceous fumarolic deposits had pronounced Ti enrichments (3.05-23.16 wt. %). Loose siliceous soils and altered basalts collected from the same site had substantially variable TiO_2 concentrations (e.g. 23.16 and 4.65 wt. %, respectively) (Table 6). *Geptner et al.* (2007) revealed similar high contents of Ti in siliceous rocks within micron sized-globules, isometric accumulations, and bands. They postulated that the dissolution of basaltic glass in extremely low pH settings would form a silicagel and favor colloidal TiO_2 accumulation into local aggregates. *Markússon and Stefánsson* (2011) observed dense accumulations of anatase in SEM, which could support the accumulation of TiO_2 in siliceous deposits.

Table 6: Compositional variation in altered basalts and soils from the same sample site

Sample	Type	SiO2	TiO2	Zr	S
IV13-6	Basalt	86.76	4.54	288	0.29
	Soil	84.93	7.06	351	0.19
IV13-7	Basalt	66.14	2.78	160	1.00
	Soil	71.22	11.27	596	-
IV13-8	Basalt	80.16	4.65	333	0.07
	Soil	65.90	23.16	1343	0.24
IV13-9	Basalt	80.16	4.65	203	0.07
	Soil	81.52	3.68	207	0.27
IV13-12	Basalt	85.46	3.50	224	0.16
	Soil	84.81	3.05	183	-
IV13-15	**Unaltered**	**48.81**	**1.83**	**97**	**0.04**

"-" Not Measured

Alternatively, anatase (or TiO_2 aggregates) may have become preferentially concentrated into the loose sediments as the basalt became more friable due to increasing alteration. The influence of biological activity on TiO_2 accumulations cannot be ruled out, as clusters of anatase were observed in close association with mineralized bacteria (*Geptner et al., 2007*). Nevertheless, the apparent enrichment of TiO_2 in diverse settings indicates its relative immobility in acid-sulfate environments.

6.2 Occurrence and Formation of Secondary Alteration Mineralogy

6.2.1 Leached Silica Deposits

Hydrated amorphous silica was a common alteration product across the geothermal area and increases in concentration with increasing surface activity. Amorphous silica is insensitive to oxidation state and formed veins along the distal margins of activity. Acid-sulfate leaching of high-Fe basalt produced three different manifestations for amorphous silica: (i) pseudomorphic replacements of primary igneous silicates, (ii) altered glass that had been leached of mobile elements, and (iii) deposits lining the exterior surfaces and gas vesicles (Figure 20a-c). Silica-rich soils <1 meter thick developed halos around the fumarole, and at Hverir the extent of alteration was ~4 meters radius around the sulfur mound (Figure 20e). Thin silica-sinter deposits precipitated on altered basalts near hydrogen sulfide vents (Figure 20f). Some of the silica deposits may also have been microbially-mediated, indicated by silica micro-filaments (Figure 20d). The morphology is analogous to microbial filaments in near-neutral sinter deposits observed in several geothermal fields across Iceland (*Tobler et al., 2008*). In our study, the high-temperature silica polymorph cristobalite accompanied amorphous silica near a high-temperature fumarole (~100°C), while quartz was most often observed along the hyaloclastite ridges. Secondary quartz may be a residual product from early alteration of sideromelane in altered hyaloclastite deposits.

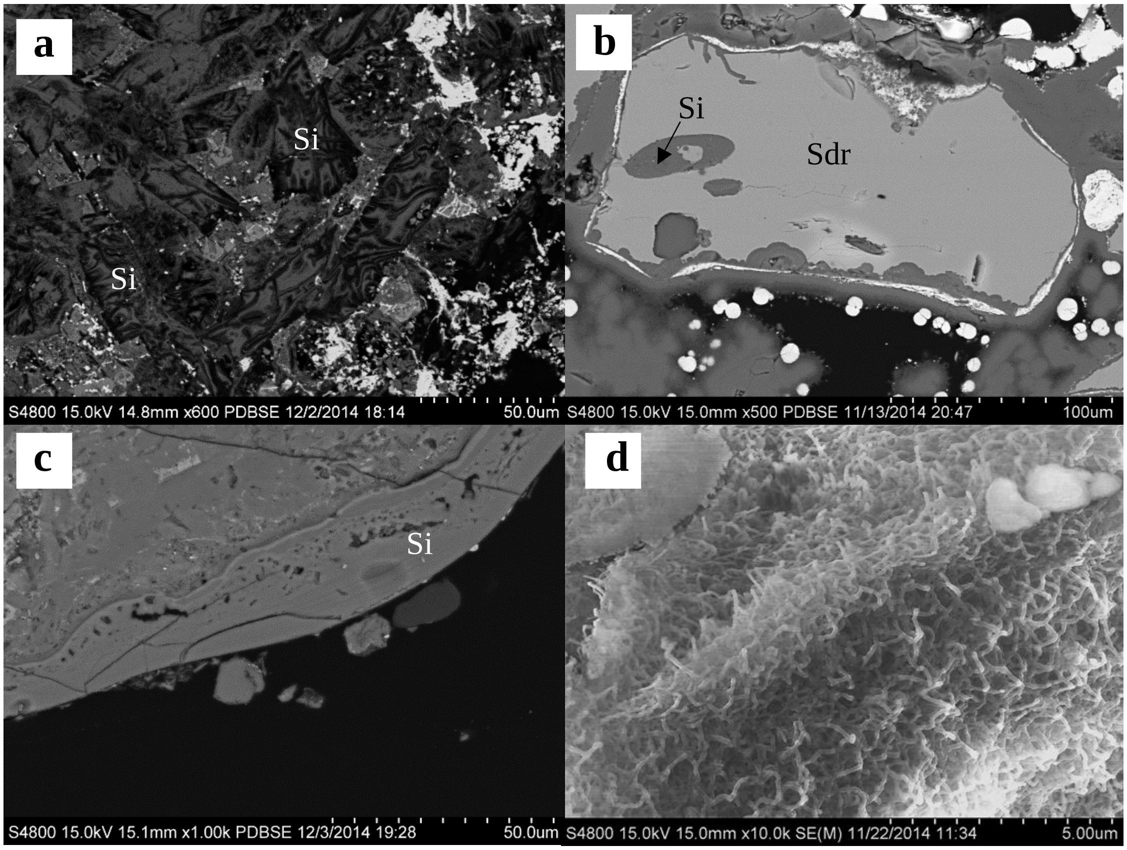

Figure 20: Amorphous silica morphologies shown in SEM images. (a) Pseudomorphic replacement of plagioclase (IV13-7), (b) etched rims of primary basaltic glass (i.e. sideromelane) are leached of major elements and replaced by a layer of amorphous silica (darker gray) (IV13-13), (c) interior lining of a gas vesicle (IV13-12), (d) silica micro-filaments (IV13-13), All samples were collected in the alteration apron from an active fumarole in the Hverir geothermal field. Amorphous silica (Si), Sideromelane (Sdr), and Hematite (Hm).

6.2.2 Iron-Sulfide Formation and Oxidation

Widespread occurrences of Fe-sulfides (pyrite and marcasite) were observed near mud pots at Hverir and to a lesser degree Krafla. A high supply of H_2S gas produced a locally reducing environment with high water-rock ratios, where the oxidation front extends all the way to the surface. In areas of low activity and H_2S supply, pyrite is found at depth below the oxidation front (Figure 21). Micron-scale pyrite cubes were also observed in altered siliceous deposits in high activity areas near fumaroles.

At Krafla, Fe-sulfide minerals are observed directly precipitating from small bubbling mud pots, but are notably absent in the large thermal pool (~30°C) in the northern drainage basin. There, direct precipitates had the same mineral assemblage at the Námafjall mud pots; except, with the notable absence of pyrite and the addition of natroalunite. Water composition reveals a well-mixed thermal pool with lower temperatures relative to the surrounding mud pots. A lower supply of H_2S gas and more oxidizing conditions may have altered previously existing pyrite into natroalunite.

The oxidation of pyrite is a complex biogeochemical process involving hydration, hydrolysis, redox reactions, and microbial catalysis in the reaction below:

$$FeS_2\,(aq) + 3.75O_2\,(g) + 3.5H_2O\,(l) \rightarrow Fe(OH)_3(s) + 2H_2SO_4(aq)$$

The rate of pyrite oxidation depends on a variety of factors that include T, pH, Eh, relative humidity, and surface area. Ultimately, the driving forces for the breakdown of pyrite and marcasite are interaction with H_2O and atmospheric O_2, which results in the oxidation of more soluble Fe^{2+} to insoluble Fe^{3+}, often in the form of goethite, and the formation of sulfuric acid. Large pyrite cubes in relatively discrete abundances can form goethite directly from the oxidation of pyrite, which has been previously observed in other Icelandic geothermal systems (*Markússon and Stefánsson, 2011*). Thermophilic Fe- and S-chemoautotrophs also pay an important role during the oxidation of pyrite. Interestingly, the oxidation of pyrite produces more sulfuric acid per mole than other sulfides (*Alpers & Brimhall, 1989*), which results in very low pH conditions and the release of heavy metals into surface and ground waters (including Au, Ag) (*Geptner et al., 2007*). Acidic hydrothermal solutions precipitate efflorescences of soluble and insoluble sulfate-salts. The former, although ephemeral, provide direct evidence for the pathways of sulfide oxidation and the alteration of associated mineral assemblages.

Layer	Amorphous	Anatase	Kaolinite	Sulfur (S^0)	Fe-sulfide	Fe^{3+}-sulfate	(Natro)alunite
Yellow	XXX	X	-	XX	-	X	X
Light grey	XXX	X	-	X	-	X	X
Dark grey	X	X	+	-	XX	-	-

Layer	Quartz	Anatase	Kaolinite	Smectite	Fe-sulfide	Fe^{2+}-sulfate	Fe^{3+}-sulfate	Al-sulfates
Orange	X	X	-	+	-	-	X	X
Light grey	XX	X	-	-	-	-	-	-
Dark grey	X	X	+	-	XX	X	-	-

Figure 21: Shallow depth profiles atop Námaskard adjacent to two different active mud pots. Fe- and S-oxidation front appears as the transition from the dark gray mud (bottom) to the surface layer in the following redox pairs: Fe^{3+}/Fe^{2+}, S^0/H_2S, and SO_4^{2-}/H_2S. Reduced mineral phases are found at depth, while more oxidized phases appear at the surface. (a) Depth profile near main drainage channel at Námaskard (top to bottom: IV13-31, 32, and 30). Elemental sulfur and Fe^{3+}-sulfates are found at the top, while Fe-sulfides dominate the mineral assemblage at the bottom. (b) A shallow pit atop Námaskard adjacent to several mud pots (top to bottom: IV13-24, 25, 26). The thin orange layer is dominated by jarosite and Al-sulfates (alunogen, rostite), while Fe-sulfides and Fe^{2+}-sulfates are dominant at the bottom.

6.2.3 Efflorescence of Soluble Sulfate-Salts

Bulbous and fibrous aggregates were observed forming white surface efflorescence around mud pots and fumaroles. High-temperature and acidic conditions dissolve primary igneous phases and mobilize Fe^{2+}, Al^{3+} and other mobile cations out of the system. Previous studies indicate that sulfide reacts more quickly than Fe during pyrite oxidation, giving rise to aqueous solutions enriched in SO_4^{2-}, H^+, and Fe^{2+}. The neutralization of acidic fluids promotes the removal of Fe, Al, and other metals form solution, but has a less noticeable effect on SO_4 concentrations.

The oxidation of Fe-sulfides and supply of mobile cations formed a variety Fe^{2+}-, Fe^{2+}Al-, Ca-, and Mg-insoluble and soluble sulfate-salts. Mud pots had high SO_4, Fe, and Al aqueous concentrations that produced a widespread zone of the halotrichite and/or pickingerite ($(Fe,Mg)Al_2(SO_4)_4 \bullet 22H_2O$). Extensive solid-solution occurs in these minerals, where Fe>Mg the mineral is classified as halotrichite, while pickeringite is more magnesium-rich. Their XRD patterns are very difficult to distinguish and, therefore, a positive identification of either mineral is labeled as the halotrichite group. Bilinite ($Fe^{2+}Fe^{3+}{}_2(SO_4)_4 \bullet 22H_2O$) also forms a solid-solution series with halotrichite (identified by *Geptner et al., 2007*), indicating additional solid solution between mixed valence states of Fe.

Ferrous iron sulfates (rozenite and szomolnokite) were found as minor components in the white aggregates. The oxidation of pyrite enhances the formation of these phases by decreasing their solubility. Investigations of sulfate-salts in volcanic and acid-mine drainage environments reveal that the formation of rozenite comes first and through a slow recrystallization processes forms szomolnokite. This observation is supported as rozenite, a metastable phase in aqueous solutions (*Rearclon & Beckie, 1987*), was the only Fe^{2+}-sulfate observed in the gray mud closest to active mud pots. Szomolnokite is the only stable sulfate in contact with aqueous solutions found in the larger Krafla area. Mg-sulfate (starkeyite, epsomite) stability covers a large temperature range. In previous studies, these sulfates are commonly associated minerals in volcanic fumaroles and acid-mine drainage environments (e.g. *Nordstrom & Alpers, 1999*).

6.2.4 Alunite-Jarosite Group

Members of the alunite-jarosite group are the most abundant sulfate phases observed in this study and are found in diverse environmental settings. They were identified in XRD patterns and by SEM, where they were observed to have distinct psuedocubic crystals, ranging from <5 to 20 µm in diameter (Figure 22). These minerals line interior walls of vesicles associated with amorphous silica and spheroidal FeOx. In other instances, dense aggregates partially fill vesicle interiors. Alunite minerals were more abundant in higher temperature areas proximal to the fumaroles, whereas jarosite was observed in medium to low activity areas under more oxidizing conditions.

The alunite-jarosite group minerals have an idealized chemical formula [$\mathbf{AB_3}(SO_4)_2(OH)_6$] where the A site is occupied by monovalent species K^+, Na^+, H_3O^+, while the B site is occupied by trivalent species Al^{+3} and Fe^{+3}. When Fe>Al the mineral is classified as jarosite, while those minerals with Al>Fe are in the alunite family. EDS provides reliable measurements for the alunite-jarosite compositions for the relative proportions of Fe and Al, but underestimates the amount of Na and K in the sample (see *McCollom et al., 2013b*). The qualitative chemical composition at Námafjall ranges from natroalunite to Al-bearing jarosite, and often shows enrichment of Fe and K in the crystal rims (Figure 23). Significant compositional zoning of the A site was also observed within individual crystals. Polished grain mounts showed similar pseudocubic morphology despite differences in chemical composition.

The alunite-jarosite group is known to range in composition as a result of significant solid solution mixing in the A site, while substitution of the B site is less common. Published data reports compositions that lie close to Fe and Al end-members, which likely reflects a miscibility gap between alunite and jarosite (*Stoffregen et al., 2000; Papike et al., 2006*). Possible explanations for the miscibility gap include differences in hydrolysis constants for dissolved Fe and Al species or oxidation state during deposition (*Stoffregen et al., 2000; Papike et al., 2006, 2007*). However, a few studies have reported intermediate compositions between natroalunite and Al-bearing jarosite in zoned pseudocubic crystals that were found in the early stages of acid-sulfate alteration of basalt in natural systems (*Morris et al., 2005; McCollom et al., 2013a*). Compositional zonation of the A site in Námafjall samples likely reflects local and temporal variability in ambient fluid compositions during mineral precipitation (e.g. *Juliani et al., 2005; Papike et al., 2006*). Although Krafla basalts lack significant K-bearing minerals, the abundance of jarosite can be attributed to the release of K from altered glass (e.g. IV13-14). Na-jarosite was associated with orange precipitates in fumarolic settings. This may be because Na and other elements are more readily retained in the products of alteration near fumaroles, which allows Na to be incorporated into the mineral structure.

The substitution of Fe and Al in the B site is likely attributed to local variation in the chemical environment caused by the decomposition of Al-bearing (plagioclase) and Fe-bearing (olivine, augite) minerals. This is supported by the wide compositional variation within an individual sample. On the other hand, the enrichment of Fe in the crystal rims may reflect a transition to more oxidizing conditions, which makes more ferric Fe available for precipitation in the minerals (*Papike et al., 2006*). Regardless, EDS measurements record significant Fe-for-Al substitution within the crystal structure in alunite-jarosite group minerals during acid-sulfate alteration at Krafla, which corresponds well to alunite-jarosite observed in synthetic and natural basaltic systems (*Morris et al., 2005; McCollom et al., 2013a,b*).

Members of the alunite-jarosite group were often associated with spheroidal hematite. This observation suggests that the alunite-jarosite group may be unstable over time, eventually breaking down and forming more stable spheroidal hematite (*Desborough et al., 2010; McCollom et al., 2013b*).

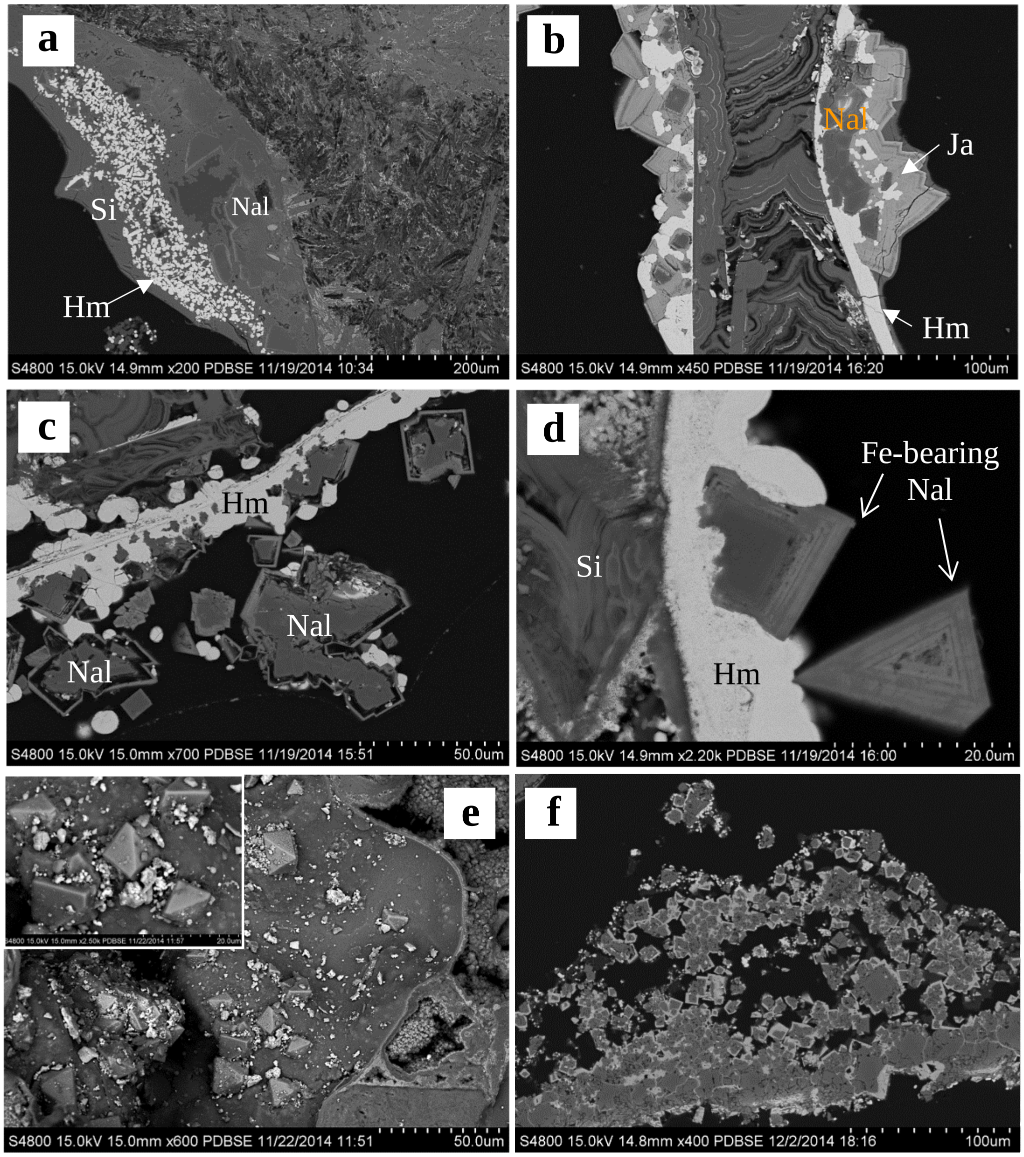

Figure 22: Examples of the pseudocubic habit of the alunite-jarosite group from altered basalts from the Hverir geothermal field. Members of this group shown are natroalunite determined by EDS, except in Figure 6b, where jarosite was observed. (a) Interior vesicle wall with natroalunite, hematite, and amorphous silica (IV13-14). (b) Adjacent vesicle walls with jarosite (white) forming on top of natroalunite (dark) with hematite and amorphous silica intermixed (IV13-14). (c) Natroalunite cubes with dissolved interiors. (d) Natroalunite cubes with K-rich rims and Al-rich interiors (IV13-14). (e) Psuedocubic natroalunite closely associated with hematite spherules. Insert shows expanded view of the surface (IV13-13). (f) Abundant natroalunite partially infilling a vesicle from a heavily altered basalt from the silica-rich alteration zone (IV13-7). Nal = natroalunite, Hm = hematite, Si = amorphous silica.

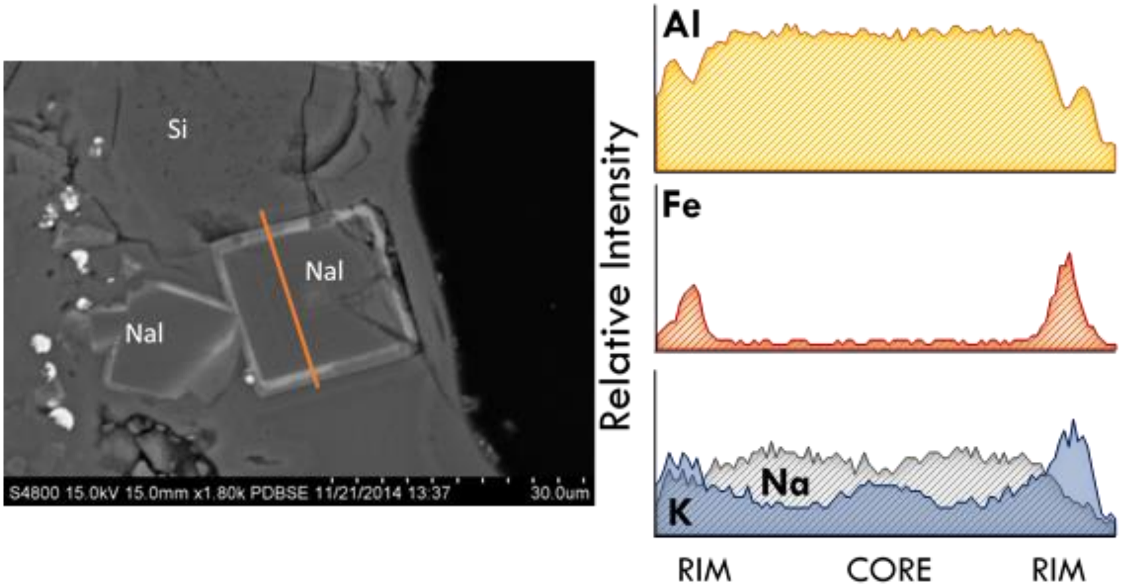

Figure 23: Natroalunite exhibits compositional zoning (IV13-13). Alunite-jarosite group minerals have the chemical formula [$AB_3(SO_4)_2(OH)_6$] (A site occupied by monovalent species K^+, Na^+, H_3O^+, while the B site is occupied by trivalent species Al^{+3} and Fe^{+3}). Zoned natroalunite (orange line = transect) shows Al-rich and Fe-depleted cores with elevated Fe and K along the rims. K is also slightly enriched in the core. Amorphous Silica (Si), Natroalunite (Nal).

6.2.5 Spheroidal Hematite

Abundant spheroidal Fe-oxides were observed in sulfate-rich fumarolic deposits. Two FeOx populations were observed with similar spheroidal shape: (i) micron-sized (typically ~1-3μm diameter) spherules observed forming dense clusters around basaltic glass fragments and relict plagioclase and (ii) larger (~5 to 20 μm diameter) individual spheroids that often form botryoidal clusters (Figure 24). FeOx spherules lining gas vesicles or exterior surfaces are identified as hematite, which was abundant in the XRD patterns. Additional spherules within the interior of the basalt were observed, and may correspond to trace amounts of goethite detected in XRD. All FeOx spherules contain impurities of Al, Si, S, and P that may serve as a nucleation site for mineral formation (*Golden et al., 2008*). Spheroidal FeOx associated with the alunite-jarosite group and amorphous silica lining vesicle walls and exterior surfaces are commonly found mineral assemblage in volcanic acid-sulfate environments (*Morris et al., 2005; Bishop et al., 2007*). Additionally, these FeOx spherules exhibit a radial growth pattern consisting of rods or fibers. Morphology, elemental composition, and association with Fe-bearing sulfates support the interpretation that spheroidal hematite in the fumarolic deposits is related to aqueous precipitation during acid-sulfate alteration of basalt.

The occurrence of Krafla spherules provides direct evidence for the formation of spheroidal hematite during acid-sulfate alteration, but it is unknown whether hematite formed from the dissolution of basaltic precursors or through a multi-step process. The latter involves a simplified two-step process: (i) the formation of Fe-bearing sulfates (e.g. jarosite) and (ii) the dissolution of sulfates to form spheroidal hematite through forced hydrolysis. *Morris et al.* (2005) noted the apparent absence of hematite in altered basaltic tephra at Mauna Kea where hydrothermal solutions did not form sulfate minerals. This observation implied that the formation of jarosite and Fe-bearing natroalunite under acid-sulfate conditions was a necessary precursor for the formation of hematite spherules.

Recent laboratory experiments support the multi-step hypothesis. Several studies have shown that hematite spherules can directly precipitate from aqueous solutions during forced hydrolysis at ~100°C (e.g. *Kandori et al., 2000*). Spheroidal growth is affected by a variety of factors that include: anions (SO_4, Cl), super-saturation, extent of hydrolysis, viscosity of the medium, and impurities (*Golden et al., 2010*). *Golden et al.* (2008) synthesized both jarosite and spheroidal hematite from Mg-Al-Fe-SO_4-Cl solutions in the following reaction sequence: (i) initial precipitation of metastable hydronium jarosite at pH 1.2-1.5, (ii) jarosite dissolution and precipitation of an intermediate ferric hydroxyl species through forced hydrolysis that polymerizes into hematite, and (iii) precipitation of hydronium alunite upon depletion of hydronium jarosite. Hydrothermal acidic conditions and high Fe^{3+} concentrations promote the formation of hematite over goethite (*Cornell and Schwertmann, 1996*). However, goethite is predicted to form from the breakdown of jarosite under reducing conditions (*King & McSween, 2005*), which is supported by observations in acid-mine drainage (AMD) environments (*Fernandez-Remolar et al., 2005*).

The spheroidal hematite observed at Krafla closely resembles that produced by *Golden et al. (2008)* and observed at Cerro Negro (*McCollom et al., 2013b*) in size and morphology. The co-occurrence with members of the alunite-jarosite group suggests that hematite spherules may have formed through dissolution of Fe-bearing natroalunite and jarosite as alteration proceeded. Interestingly, Mauna Kea spherules are up to ~5x larger in diameter than those observed at Krafla. The reason for this is not apparent, but it may be the result of the duration of hydrothermal activity or the extent of jarosite dissolution. Compositional impurities were observed (e.g. Al^{3+}) and may signify changes in the composition of aqueous solutions during the formation of hematite spherules (e.g. *Morris et al., 2005*).

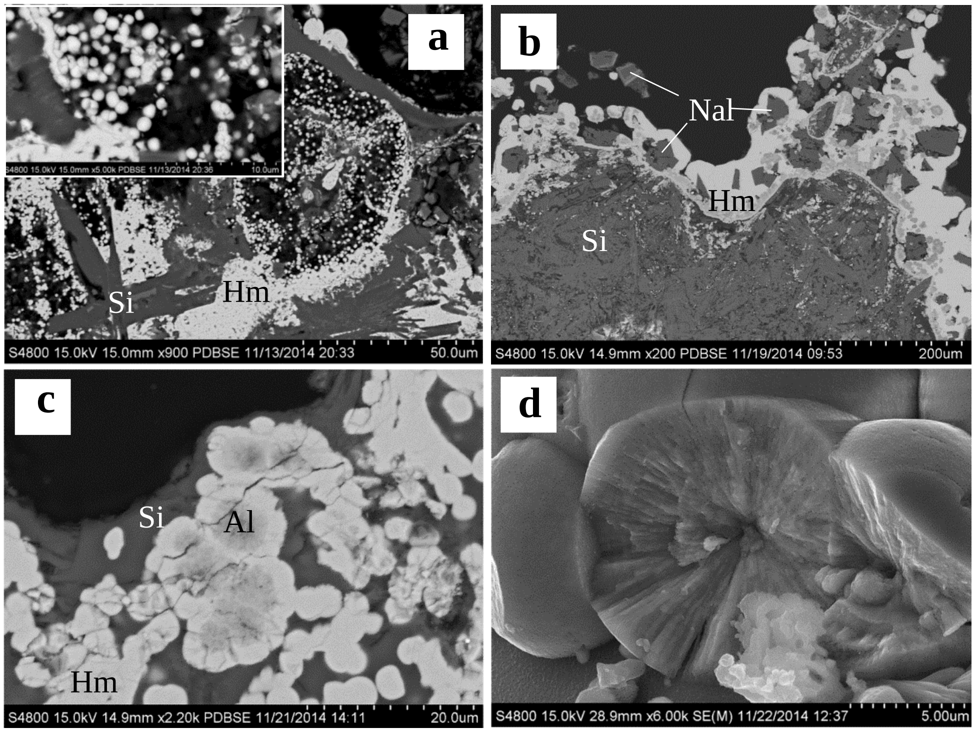

Figure 24: Two distinct hematite spherule size populations: >3 and 5-20 micron range, with minor Al, Si, and S concentrations. (a) Hematite spheroids formed along the wall of vesicles and relict plagioclase crystals (IV13-13). Insert shows an expanded view of spheroids. (b) Botryoidal morphology along vesicle walls with natroalunite cubes present (IV13-14) and (c) Al-rich centers in Fe-oxide spherules may represent Al cores (Al) of remnant natroalunite (V13-13). (d) Broken spherule shows fibrous/radial morphology of hematite. Hematite was identified by XRD analysis.

6.2.6 Phyllosilicates

Kaolin and smectite group minerals are the main phyllosilicates at Krafla and Námafjall. Kaolin group minerals (kaolinite, halloysite) and smectite (Al- to Mg/Fe-rich compositions) generate a spotty distribution of red, brown, yellow, pink and white patches, reflecting the mosaic pattern of alteration along the distal margins of surface activity (*Geptner et al., 2005, 2007*). However, kaolinite and trace amounts of smectite have been found in areas of high surface activity.

Kaolin group minerals are observed near acidic mud pots in the presence of Fe-sulfides. Fumarolic activity near drainage channels produced samples of almost pure kaolinite to kaolinite accompanied by anatase, Al-sulfates, and hematite. Based on these observations, kaolinite initially formed in areas of intense leaching in low pH environments, likely forming during surface channeling of acidic fluids (*Mínguez et al., 2011*). Kaolinite crystallinity improves in low pH environments, albeit kaolin group minerals are more stable in mildly acidic to neutral environments (*Fialips et al., 2000*). In the Krafla and Námafjall areas, kaolinite became more dominant in areas of medium to low activity.

In general, smectite was found in areas of low surface activity, where the neutralization of acidic fluids thermodynamically favors smectite formation. *Mínguez et al.* (2011) observed a range of smectite composition that reflected the composition of the Holocene basalts and Pleistocene hyaloclastites. For example, Al-rich smectite (beidellite and montmorillonite) was more abundant in the hyaloclastite, while nontronite (Fe (III)-bearing smectite) was more abundant associated with altered high-Fe basalt. The varying compositions may also reflect changes in the acidity of the fluids, where the extent of alteration affects the amount of cations released into solution. Additionally, increased distance from the pathway of hydrothermal fluids will raise the pH and neutralize the acidity within the system and, thereby, precipitate out minerals containing more mobile elements (e.g. Ca, Mg). The composition of smectite depends on a combination of several factors including the pH of the fluid, element mobility, and the pathway of the fluids.

It is important to remember that the genesis of poorly crystalline smectite clays comes from the hydration of sideromelane fragments, i.e. palagonite. Through continued alteration, palagonite transforms into smectite, hence, smectite is the most abundant mineral phase in areas of low surface activity along hyaloclastite ridges. Under higher temperature conditions smectite transitions to interstratified smectite and illite; since these clay phases have not been identified, the upper temperature limit at the surface/near surface can be constrained to ~200°C.

Theoretical thermodynamics indicates that most phyllosilicate formation is favored by moderate to alkaline pH conditions (e.g. *Velde, 1995*). However, kaolinite can precipitate at low pH (*Fialips et al., 2000*). The behavior of phyllosilicate stability in low pH systems in high ionic strength is not well understood. For example, Mg-smectites (e.g. saponite) are more susceptible to acid waters than Al-phyllosilicates. Even so, *Story et al. (2010)* showed that these phyllosilicates are able to persist in sediments saturated in acid-saline lakes in Western Australia. In addition, *Peretyazhko et al. (2014*) synthetically produced saponite and nontronite from the alteration of basaltic glass under mildly acidic conditions (pH 4). One important observation is the co-occurrence of smectite and jarosite in medium to low activity areas, suggesting that smectite may be able to form *in-situ* under mildly acidic conditions in the presence of high ionic strength solutions. In the orange sediments, smectite can persist and remain stable in close proximity to low pH local discharge areas.

6.2.7 Gypsum Mound Formation

Gypsum ($CaSO_4 \cdot 2H_2O$) forms large mounds to the north beyond the currently active hot springs at Leirhnjúkur. Gypsum is only an accessory phase in surface precipitates near high-temperature discharge areas, yet makes up the majority of this currently non-thermal deposit. This mound could be the result of an earlier, less acidic phase of hydrothermal alteration where gypsum would be more likely to precipitate. Alternatively, it could represent the replacement of earlier-formed soluble sulfate-salts and elemental sulfur to gypsum after hydrothermal activity decreased.

Another interesting observation is a relatively rare mineral variscite ($AlPO_4 \cdot 2H_2O$) observed in small blue-green nodules. Variscite forms by reactions between phosphate-rich fluids and an aluminous substrate in volcanic environments. Cation analysis in modern Krafla hot springs did not reveal significant phosphate in solution. In other volcanic settings, aqueous phosphate is derived from disseminated apatite in the host rocks, however; apatite is not observed in Leirhnjúkur hyaloclastite or in Krafla drill cores. The exact phosphate source for the variscite is unknown, although *Markússon and Stefánsson (2011)* observed phosphate deposits enriched up to ~22 wt. % in the Krýsuvík geothermal field, SW Iceland. Perhaps geothermal fluids passed through phosphate-rich deposits during the ascent to the surface and reacted with the aluminous hyaloclastites to precipitate nodules of blue-green variscite. The exact formation mechanism for the variscite remains speculative.

6.3 Relict Geothermal System

It is not known exactly when Lítli-Leirhnjúkur was geothermally active, regardless; the relict geothermal system helps identify which secondary phases persist under present-day environmental conditions. A limited suite of secondary minerals was found that includes kaolinite (halloysite), anatase, hematite, and minor amounts of smectite. It is likely that these deposits formed in acid-sulfate fumarole environments. A likely modern analog for the Lítli-Leirhnjúkur deposit is the currently active system at Leirhnjúkur, especially the fumaroles situated along drainage channels with high surface channeling of hydrothermal fluids that precipitate kaolinite and anatase. Along the margins smectite and hematite are more abundant, while goethite is noticeably absent at Lítli-Leirhnjúkur. Perhaps goethite was transformed into hematite under more oxidizing conditions, or upon longer exposure to ambient conditions. On the other hand, goethite may be present in minor amounts not detectable by XRD. The predominance of kaolinite over smectite in the Lítli–Leirhnjúkur area likely reflects intense fumarolic alteration with significant channeling of hydrothermal fluids.

Calcite coatings and veins within altered hyaloclastites were found only at Lítli-Leirhnjúkur. In the Námafjall area, *Mínguez et al.* (2011) observed kaolinite growing around a nucleus of FeOx and calcite grains. The presence of calcite, which corresponded to the most intense alteration at Námafjall, may have been related to the outpouring of CO_2 during the Krafla Fires episodes (*Gudmundsson et al. 2005*). Alternatively, calcite may have been produced by the dissolution of gypsum due to the common ion effect. Gypsum, being more soluble than calcite, would dissolve more readily under rain and snowfall events (~1100 mm/yr in the Mývatn area). When gypsum dissolves, it releases

Ca^{2+} cations into solution, where the fluids can become supersaturated and precipitate calcite in the following reaction:

$$CaSO_4 \cdot 2H_2O + 2HCO^{3-} \rightarrow CaCO_3 + SO_4^{2-} + 2H_2O + CO_2$$

Although there is no direct evidence for gypsum at Lítli- Leirhnjúkur, it is likely that gypsum formed under fumarolic acid-sulfate alteration because it is a common alteration product in active geothermal areas at Leirhnjúkur and Námaskard and is present at the non-thermal mounds north of Leirhnjúkur.

6.4 Overall Water-Rock Interaction, Secondary Mineralogy, and Water Chemistry at the Surface

Hydrothermal surface alteration of Pleistocene hyaloclastites generates a mosaic distribution of varying surface colors and compositions along the margins of surface activity as the result of aggressive and changing geothermal conditions associated with the appearance and renewal of faults and fissures. The alteration halos or aprons around fumaroles and mud pots exhibit distinct mineralogical and geochemical trends as the result of element mobility and the formation and precipitation of secondary minerals. The dominant processes acting within a volcanic geothermal system include: (i) the supply of acid and H_2S, (ii) the extent of the reaction and pH of the water, and (iii) the redox conditions (relationship to the oxidation front) (*Markússon and Stefánsson, 2011*).

Acid-sulfate waters are produced upon the boiling of aquifer fluids, resulting in phase segregation of the vapor/steam from the boiling water. Rising volcanic vapors enriched in H_2S and CO_2 condense into oxygenated ground- and surface-waters where the H_2S is oxidized into sulfuric acid and the CO_2 is mostly degassed (*Kaasalainen &*

Stefánsson, 2012). The results are acidic waters with pH <4 and reducing conditions that alter basalt and hyaloclastite in gas- (low water-rock ratios) and fluid- (high water-rock ratios) dominated settings. Dissolved ion concentrations correspond well to bulk hyaloclastite and basalt compositions in the most acid waters, indicating that the substrate dissolves nearly stoichiometrically (pH <2.5) with respect to most major rock-forming elements. Overall, dissolved ion concentrations are related to pH, with higher acidity associated with greater cation abundances.

These high-temperature and localized fluids become supersaturated with respect to pyrite, kaolinite, amorphous silica, and native sulfur (*Markússon and Stefánsson, 2011*). While amorphous silica, anatase, and kaolinite are insensitive to redox conditions, pyrite and native sulfur oxidize through interactions with atmospheric O_2 and H_2O, introducing more sulfuric acid into the system. Phase segregation and sulfur oxidation are the main controls on the pH of the fluid. In gas-dominated settings, secondary minerals can precipitate directly from the volcanic vapors or during alteration of primary igneous phases. In contrast, alteration products in fluid-dominated settings are controlled largely by the oxidation of iron sulfide deposits.

The dissolution of primary phases at depth creates a continuous supply of dissolved aqueous species that form a diversity of secondary minerals. For example anorthite ($CaAl_2Si_2O_8$), a common feldspar in the hyaloclastite and basalt substrate, is altered in the following generalized chemical equation from *Stoiber and Rose* (1974):

$$CaAl_2Si_2O_8 + H_2SO_4(l) + 3H_2O + O_2$$

$$\rightarrow CaSO_4 \cdot 2H_2O + Al_2Si_2O_5(OH)_4$$

The reaction of Ca-rich plagioclase with sulfuric acid produces gypsum and kaolinite at some fumaroles, while gypsum, amorphous silica, and amorphous alumino-silicate are dominant at Hverir fumaroles. Plagioclase readily releases Ca and Na into solution followed by Al, where some of these elements are incorporated into a variety of sulfate phases. Augite, olivine, and basaltic glass releases Fe into solution that forms hematite, goethite, and sulfates (Fe-bearing natroalunite, jarosite). Other sulfate phases identified likely formed from the leaching of primary minerals and basaltic glass through similar chemical reactions described by *Stoiber and Rose* (1974). The chemical and mineralogical trends across the geothermal area vary depending upon the water-rock ratios, lithology, and other environmental parameters that will be discussed below. Field photos that helped create the conceptual models are found in Appendix A.

6.4.1 Hot Springs (Mud Pot) Alteration Model

A conceptual model of alteration was created for mud pots, as shown in Figure 25. The influx of H_2S gas results in extensive pyrite and native sulfur deposits, enriching alteration products in S (5.31-7.86 wt. %). Acid leaching dominates closest to the mud pot, resulting in significant depletion of most major elements. This area also features a residual enrichment in SiO_2, TiO_2, and Zr (as illustrated in X_2, Figure 26). In the orange sediments and precipitates along the margins, most elements are still depleted with the exception of phosphorous and iron (X_1, Figure 26). Fe and Al mobility are lower in these sediments and these elements are incorporated into alunite, jarosite, smectite, and zeolites. Iron and sulfur mineral assemblages depend largely on the position of the oxidation front, defined by the transition from reduced to oxidized mineral phases.

Pyrite oxidation generates a secondary mineral series associated with increasing distance from the mud pot in the following order: pyrite→ rozenite → szomolnokite/ halotrichite group → jarosite → hematite/goethite (e.g. *Nordstrom & Alpers, 1999*). Fluid compositions near mud pots have enriched ferrous Fe concentrations (122-196 mg/l) that become supersaturated with respect to iron-sulfide minerals (*Markússon and Stefánsson, 2011*). Pyrite oxidation forms a series of soluble sulfate-salts, which likely reflects the lower mobility of Fe and S in the fluid phase due to increasing oxidation. Here, Fe- and S- redox gradients develop, and can be seen in the formation of sulfides under reducing conditions and the formation of sulfate-salts and oxides as they undergo varying degrees of oxidation.

Ultimately, the further from the discharge source the more control atmospheric O_2 exerts on the secondary mineral phases and element mobility. The predominance of Fe- and Al-sulfates reflects the dominance of these dissolved species in the fluids, while Ca^{2+} and Mg^{2+} are minor components in both the aqueous and mineral phases. Fe^{2+}-sulfates (e.g. white precipitates) are only observed in areas of high to medium surface activity, suggesting that these minerals may also be temperature dependent.

At the surface, iron and sulfur oxidation occurs over several meters, while below the surface the oxidation front exhibits a sharp boundary over several centimeters (Figure 21). In two depth profiles, a thin laterally-continuous transitional layer (<5 cm) separates the oxidized from the reducing layer, but mineralogically is more similar to the oxidized surface layer. In low activity areas, pyrite appears to alter directly into goethite and/or hematite, rather than through a series of soluble sulfate-salts (*Nordstrom & Alpers, 1999*). *Markússon and Stefánsson (2011)* observed a similar trend, where Cu-sulfide (covellite) was present below the oxidation front and Cu-sulfates at the surface. At Krafla, jarosite and natroalunite dominate the sulfate mineralogy along the margins of activity, where they breaks down to form hematite and/or goethite. Smectites and zeolites are found along the distal margins of surface activity.

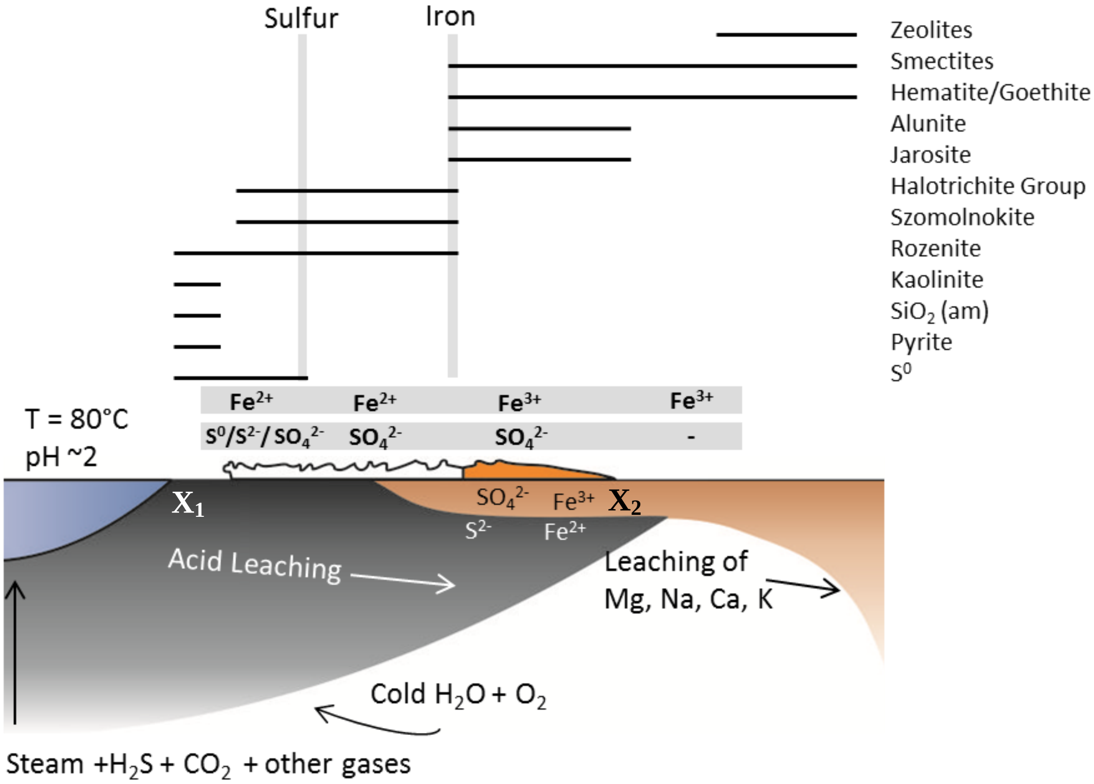

Figure 25: Conceptual model for mud pot related alteration. Alteration apron is ~2 meters in diameter. Vertical shaded bars represent oxidation-reduction boundaries between Fe^{2+}/Fe^{3+}, S^{2-}/SO_4^{2-}, and S^0/ SO_4^{2-}determined by surface mineralogy. X_1 and X_2 correspond to isocon plots in Figure 27

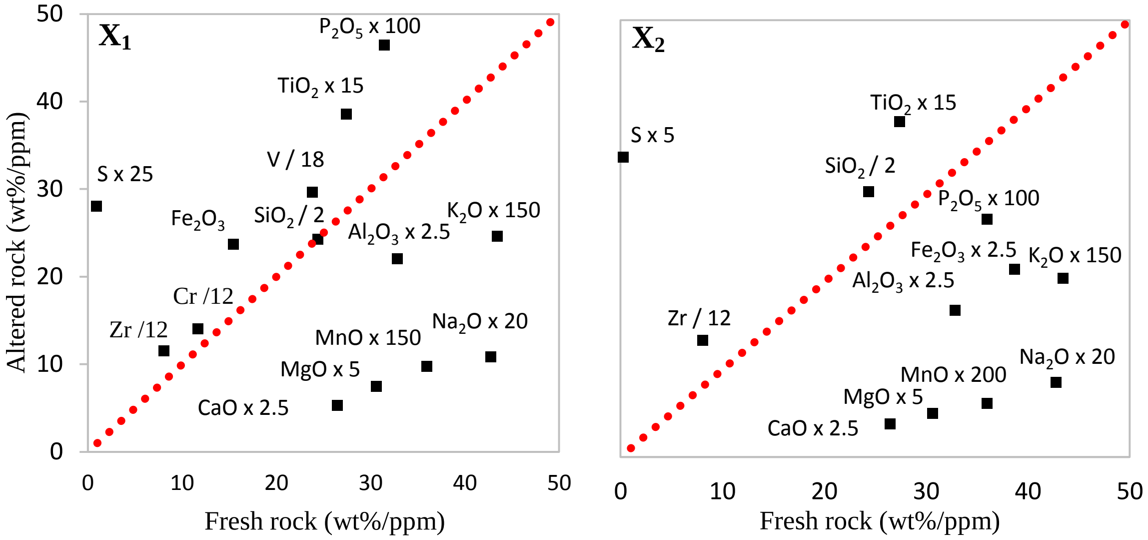

Figure 26: Isocon plots for two samples from the vicinity of a Hverir mud pot. Sample locations are marked as X_1 and X_2 on Figure 26. Enrichment and depletion of elements are assessed by their relation to the 1:1 ratio line. For these graphs, any element that plots above the line is enriched, below is depleted, and on the 1:1 ratio line is immobile relative to the fresh basalt. (X_1) In the orange precipitate/sediment, phosphorous, Fe, and siderophile elements (e.g. V and Cr) are enriched, while most major cations are depleted (IV13-2). (X_2) In the gray mud, all major cations are depleted with residually enriched Si, Ti, and Zr (IV13-4). S is enriched in both samples.

6.4.2 Fumarolic Alteration Model

Two conceptual models for fumarolic alteration illustrate the differences (and similarities) when volcanic vapors interact with Holocene basalt and Pleistocene hyaloclastite (Figure 28 and 30, respectively). These substrates differ in terms of pristine chemical composition, primary mineral stability, and petrophysical properties. These lithological proprieties affect the redistribution of petrogenic elements by geothermal fluids. The cation supply for surface precipitates and mineral formation depends upon the extent of the reaction of primary mineral phases and how effectively cations are mobilized out of the system.

Fumaroles in sideromelane-rich hyaloclastite generate alteration halos <2 meters in diameter and readily leach Mg, Ca, Mn, and Na out of the system, while Fe, Al, Ti, and Si are largely retained in the alteration products. Fumarolic vapors condense and form alunogen ($Al_2(SO_4)_3 \bullet 17(H_2O)$), gypsum, halotrichite group minerals, and Fe^{2+}-sulfates at the surface in white efflorescence. These are similar secondary minerals to those produced from the oxidation of pyrite around mud pots, indicating that the condensation of fumarolic vapors rich in Fe, Al, Ca may represent another pathway for the formation of these sulfate minerals. The mobility of Mg, Ca, Na, and K are only slightly lower along the margins of the alteration apron, but with increasing distances these highly mobile elements are incorporated into poorly crystalline Mg-silicates, smectites, and zeolites (*Geptner et al., 2007; Markússon & Stefánsson, 2011*).

Fumarolic alteration of high-Fe basaltic substrate exhibited isochemical trends, where mobile cations were extremely depleted near the discharge source (X_4 – Figure 28) but retained in the alteration apron (X_1 – Figure 28). Here, the low-water rock environment effectively mobilized major rock-forming and trace elements. Sulfur exhibits a slight enrichment in the silica-rich soils, but the majority is mobilized into the purple and red sediments. Dissolved silica and other metals were transported in solution and precipitated amorphous silica and a variety of sulfate and oxide phases along exterior surfaces and vesicle walls such as barite, gypsum, alunite-jarosite group minerals, hematite, iron-sulfides, and a minor Au-bearing material. Intermediate sulfur species (e.g. $S_2O_3^{2-}$) may help complex, transport, and precipitate transition metals (such as Au) observed in SEM (*Kaasalainen & Stefánsson, 2011*). In the purple and red sediments, Fe and Al mobility was lower in a more oxidizing environment, which enriched the samples in immobile ferric Fe. Both Fe and Al were incorporated into Fe^{3+}-bearing sulfates and oxides (e.g. $X_{2,}$ X_3 – Figure 28). These phases were important secondary minerals in medium to low activity areas. The least altered basalts show minimal leaching along the margins of surface activity, where only minor depletion of Mg, Ca, and Na were observed. Overall, sulfates and oxides were found in similar abundances in the basalt and hyaloclastite substrate.

The absence of abundant volcanic gas emissions at Hverir fumaroles may explain the lack of surface efflorescence (e.g. Fe^{2+}-sulfates), but sulfates were found in shallow depth profiles. Here, alunite is the dominant sulfate, whereas alunogen ($Al_2(SO_4)_3 \bullet 17(H_2O)$) was more abundant near fumaroles in the hyaloclastite substrate. The dominance of Al-sulfates over other sulfate phases corresponds well to fumarolic gas emissions, where $Al^{3+} >> Ca^{2+} + Mg^{2+}$ (*Hynek et al., unpublished*). Fe-bearing natroalunite, spheroidal hematite, and amorphous silica were commonly associated alteration minerals that formed along vesicles walls and exterior surfaces. These secondary phases have beenobserved in other basalt-hosted volcanic environments at Mauna Kea and Cerro Negro volcanoes (*Bishop et al., 2007; McCollom et al., 2013b*), and thus likely represent a key mineralogical assemblage of hydrothermal acid-sulfate alteration.

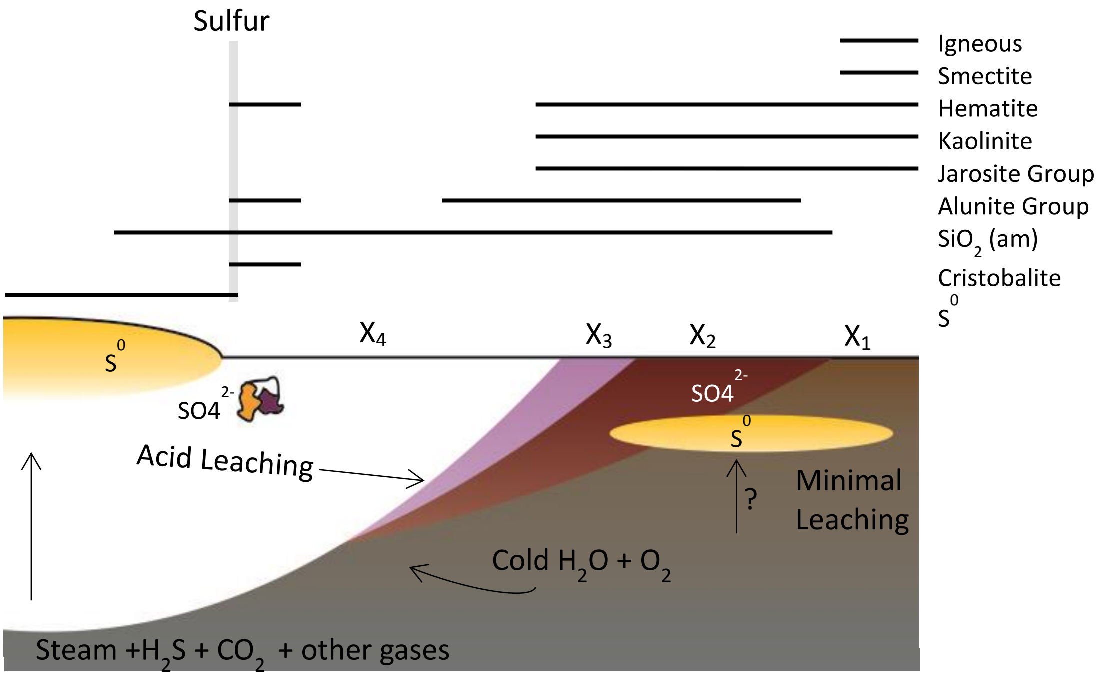

Figure 27: Conceptual model for the Hverir fumarolic apron. Alteration apron is up to 8 meters in diameter. Vertical shaded bars represent oxidation fronts determined by surface mineralogy. The sulfur-rich layer found at depth may signify diffuse sulfur-bearing vapors that did not penetrate the surface. X_1-X_4 correspond to isocon plots in Figure 28.

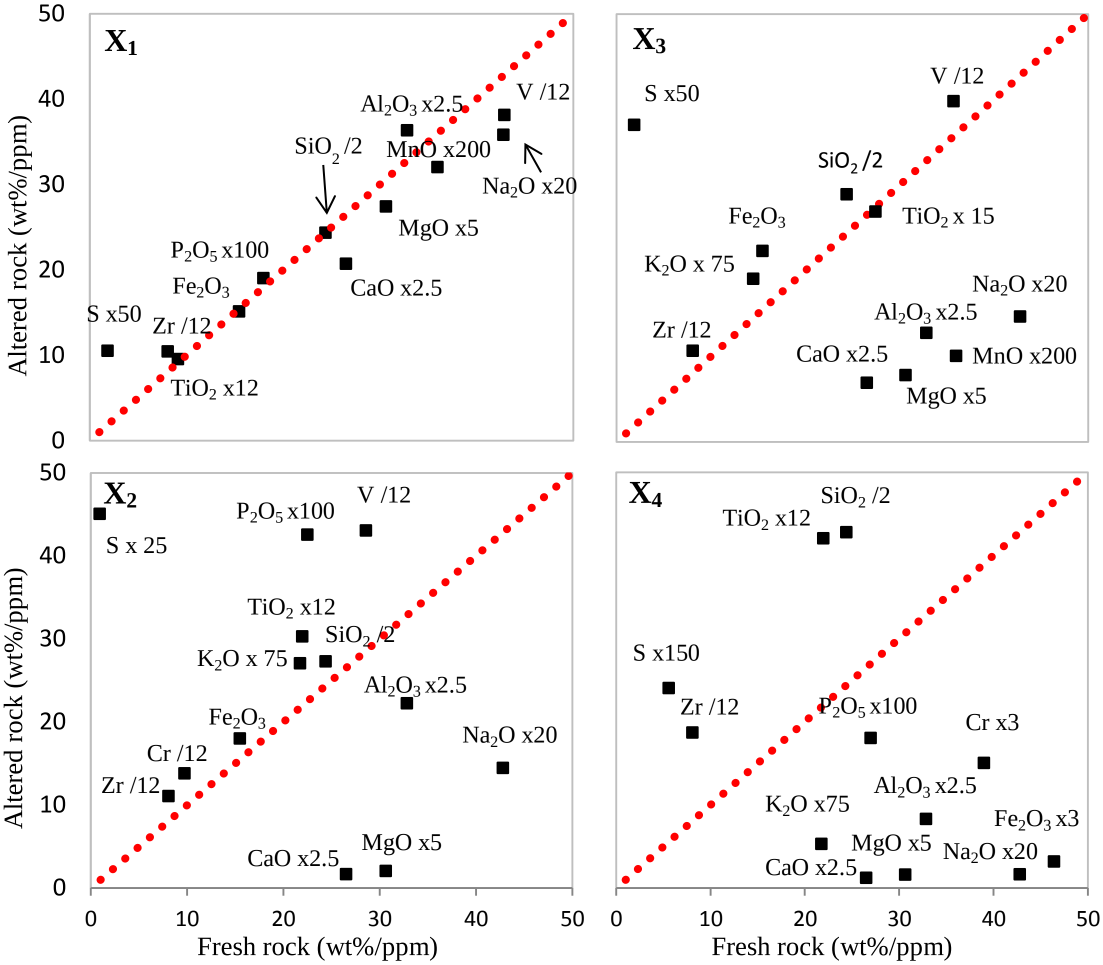

Figure 28: Isocon plots for four samples from the Hverir fumarole. Sample locations are marked as X_1, X_2, X_3, and X_4 on Figure 28. (X_1) Along the distal margin (~7 m away, IV13-11), a slightly altered basalt has minor depletions in Ca, Mg, Na, and Mn. (X_2) In the red sediments (~6 m away, IV13-13), Fe, K, and P are enriched and Al is slightly depleted, while, Ca, Mg, and Na are substantially depleted. (X_3) Purple sediments (~5 m away, IV13-14) exhibit pronounced depletions in most major elements, except for enrichments in Fe and K. (X_4) Heavily altered basalts within the silica-rich soils (~2-4 m away, IV13-12) are highly depleted of major cations with a residual enrichment of Si, Ti, and Zr. S is enriched in all samples.

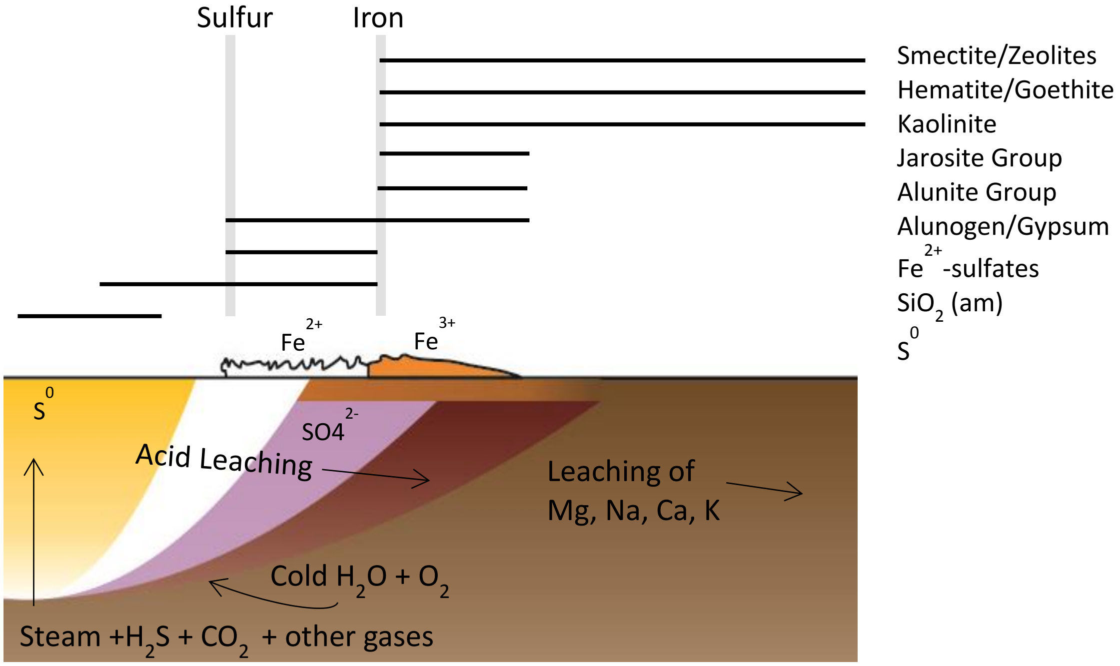

Figure 29: Conceptual model for fumaroles along hyaloclastite ridges. Alteration apron is <2 meters in diameter. Vertical shaded bars represent oxidation fronts determined by surface mineralogy.

7. Implications for Martian Hydrothermal Systems

Extrapolation of the mineralogical and chemical trends associated with the Krafla and Námafjall geothermal systems to analogous environments on Mars requires the consideration of several factors. First, the basaltic composition in Iceland differs from that of Mars. Krafla basalts have similar Fe, higher Al and lower Mg than Martian basalts. This is significant because substrate largely controls the aqueous geochemistry, which affects the secondary mineral phases present (e.g. *Tosca et al., 2004*). As a result, the basalt composition will control in part the relative abundance of secondary minerals. Second, Icelandic geothermal areas occur in open-system environments, where soluble salts and Mg, Ca, Na and other cations are leached out of the system by meteoric water. Today, Martian atmospheric conditions differ significantly from modern terrestrial conditions; however our understanding of atmospheric conditions during the Hesperian-Noachian period is limited. The abundance of ferric minerals and phyllosilicates in Noachian terrains may indicate at least locally oxidizing conditions as the result of higher atmospheric O_2 levels and/or abundant surface water that altered basaltic substrate. The gas chemistry is wholly unconstrained, but given the high levels of sulfur in Martian basalts, volcanism likely produced a high volatile content in the form of SO_2 and/or H_2S gas (*Gaillard et al., 2009*).

7.1 Home Plate, Gusev Crater

7.1.1 Sulfate-rich Paso Robles class soils

Paso Robles class soils are among the most altered materials found in the Gusev Crater, demonstrated by the presence of high SO_3 concentrations (>31%) and ferric-sulfate mineral composition (Figure 2b). Other mineral phases identified were amorphous silica, Mg-sulfates, Ca-sulfates, Ca-phosphates, hematite, halite, and allophane (*Ming et al., 2006; Yen et al., 2008*). *Yen et al.* (2008) favored alteration processes in an acid-sulfate leaching environment (e.g. fumaroles or steam condensed into caustic pools) derived from magma degassing and/or oxidation alteration of crustal iron sulfide deposits. Home Plate, a remnant volcanic structure, indicates that high-temperature volcanic gases and fluids were once common in the area (*Squyres et al., 2007*). The localized nature of the Paso Robles soils at various elevations, including depressions and on slopes, accompanied by high S concentrations, further supports a fumarole origin. The presence of hydrated ferric sulfates indicates oxidizing, low pH conditions and, therefore, that these soils formed in a highly acidic environment.

Krafla fumarolic deposits exhibit a diversity of sulfate minerals (see Table 1), but were dominated by the alunite-jarosite group, soluble sulfate-salts, and clays. *Yen et al.* (2008) noted greater abundances of Mg-sulfates, which are only a minor component of the soluble sulfate-salts at Námafjall. These differences may be attributed to variation in the major cations available in the parent rocks. Higher Mg contents in Martian basalts may have produced more Mg-sulfates during acid-sulfate alteration. On the other hand, hyaloclastite Mg contents compare well with Gusev basalts and yet hydrated Mg-sulfates (Pickeringite – $MgAl_2(SO_4)_4 \cdot 22H_2O$) are only slightly more abundant. Mg is a highly mobile element under acid-sulfate conditions. High porosity of the hyaloclastites and the frequency of rainfall events may have preferentially mobilized Mg from the basalts, explaining the low abundance of Mg-sulfates. Acid-sulfate alteration of Martian basalts may have been more akin to a closed-system, where Mg and other mobile elements would be retained in the products of alteration. Additionally, Ca and ferric Fe-phosphates were detected in the Paso Robles soils (*Lane et al., 2008*, *Yen et al., 2008*), while in the altered hyaloclastite only Al-phosphates (variscite) were detected, reflecting the high Al concentrations in the substrate.

Paso Robles class soils also contain a mixture of poorly constrained ferric sulfates (*Lane et al., 2008*). In target Arad Samara, a Fe:S ratio of approximately 2:3 was obtained by the removal of hematite, silica, and Mg-sulfate from the bulk using elemental abundances. Ferrous sulfates are excluded from consideration because they are not consistent with the Spirit Mössbauer results. *Wang et al.* (2011) identified one ferric sulfate mineral, ferricopiate ($Fe^{3+}_{2/3}Fe^{3+}_4(SO_4)_6(OH)_2 \bullet 20(H_2O)$), based on a visible-near infrared (VIS-NIR) spectral variation attributed to dehydration after exposure to the Martian atmosphere. Ferricopiatpite forms in low pH environments (pH <2.5) and under highly oxidizing conditions, typical of fumarolic settings (*Wang et al., 2011*). Other ferric sulfates are likely present, but cannot be easily constrained using available spectroscopic data. Other candidates include rhomboclase ($HFe^{3+}(SO_4)_2 \bullet 4H_2O$), paracoquimbite ($Fe^{3+}_2(SO_4)_3 \bullet 9H_2O$), kornelite ($Fe^{3+}_2(SO_4)_3 \bullet 7H_2O$), and yavapaiite ($KFe^{3+}(SO_4)_2$).

Fe^{3+}-sulfates identified in the Krafla and Námafjall area are ferricopiapite, rhomboclase, and (natro)jarosite. Pancam spectra eliminates jarosite as a viable option in the Paso Robles soils primarily because it lacks a convex upward shape at ~480 nm in VNIR spectra (*Lane et al., 2008*). The VNIR patterns of other ferric sulfates like ferricopiapite and rhomboclase exhibit this unusual spectral feature. At Krafla, these minerals were identified in sulfur-rich fumarolic soils in low pH (~2) environments, similar to those interpreted for the salty sulfate soils at Tyrone and other sites in the

Columbia Hills. Although the occurrences of these specific ferric sulfates are rare in the Krafla and Námafjall area, their presence in sulfur-rich fumarolic deposits supports the acid-sulfate fumarole model proposed by *Yen et al.* (2008). Alternatively, ferriocopiapite may have formed from other sulfate phases through a combination of dehydration, neutralization, and oxidation (e.g. *King & McSween, 2005*; *Lane et al. 2008*), similar to pyrite oxidation and/or volcanic vapors observed at Krafla and Námafjall.

7.1.2 Silica-rich Gertrude Weise Class Soils

Gertrude Weise class soils were exposed by Spirit's right front wheel in the Eastern Valley between Home Plate and the Mitcheltree/Low Ridge complex (Figure 2c). The light-toned soils are enriched in silica (as much as 91 wt. % SiO_2), Ti, Cr, and Zn, while most other major elements show a downward trend in abundance with increasing element atomic number relative to typical Martian soils (*Squyres et al., 2008*). The hydrated silica phase is identified as opal-A and no high-temperature silica phases (e.g. cristobalite or quartz) were observed, indicating a lack of diagenetic maturation (*Ruff et al., 2011*). The exact depositional mechanism, fluid-rock ratios, and environmental parameters for the silica-rich soils in the Eastern Valley are not well defined.

Eastern Valley soils and nodular outcrops are enriched in silica (~64-92 wt. %) and titanium (0.42-1.74 wt. %) and initially interpreted as leached acid-sulfate fumarole deposits due to their proximity to the Paso Robles (e.g. Tyrone) class soils. The sulfate-rich soils and Fe^{3+}/Fe total indicate low pH and highly oxidizing conditions (*Lane et al., 2008*). Acid-sulfate alteration could explain the leaching of most minerals from Gusev basalts and the relative enrichment of the most insoluble components (e.g. SiO_2, TiO_2).

However, the solubility of silica is relatively independent of pH under acidic to neutral conditions (*Alexander et al., 1954; Krauskopf, 1959*) and, therefore, the composition of the Si-rich deposits does not constrain the pH of the fluids. *Ruff et al.* (2011) argued that the silica enrichment is the result of precipitation of silica-enriched fluids in a hot spring setting rather than acid leaching. They favored near-neutral hot spring sinter deposition, noting that the lack of sulfur enrichment was inconsistent with acid-sulfate leaching. Furthermore, the high water-rock ratios associated with hot spring settings would be necessary to transport excess sulfur out of the system.

Both Krafla and Námafjall have areas of enriched silica- (~75-86 wt. %) and titanium- (~3-23 wt. %) soils, as the result of intense fumarolic acid-sulfate leaching (Figure 31). Near-neutral sinter deposits were not observed at these sites and a direct comparison between these two formation mechanisms cannot be assessed in this study. One fumarole in the Krafla area exhibited a thin, flakey silica crust altered by a hydrogen sulfide vent and showed a significant enrichment of sulfur (Figure 30a). The SO_3 content in the parent rock was 0.04 wt. % and 2.58 wt. % in the silica residue, an enrichment similar to that observed at fumaroles in the Kilauea crater (e.g. *Payne & Mau, 1946*).

Alternatively, low sulfur contents were observed in thick Si-rich soils (<1 m depth) in Hverir (Figure 31b) and Námaskard fumarolic aprons, never exceeding ~1 wt. % SO_3 (see Table 6), which is below all measured values for Eastern Valley materials on Mars. At Hverir, amorphous silica and anatase were the dominant mineral assemblages. In addition, these samples had the lowest S contents of other silica-rich deposits, and lacked sulfate phases in XRD. *Hynek et al.* (2013) also noted low sulfur contents (below ~1.5 wt. % SO_3) in silica sinter deposits near SO_2-bearing fumarolic discharge areas at

Cerro Negro volcano. In sum, results show that silica deposits related to fumarolic alteration in the Krafla and Námafjall area exhibit highly variable sulfur enrichment, ranging from <2 to 65x greater than the parent rock.

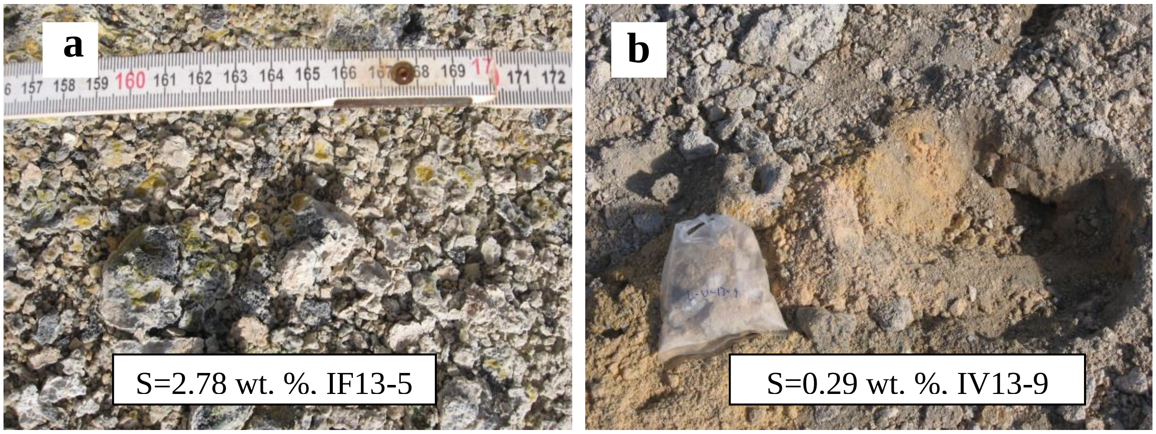

Figure 30: Silica-rich deposits associated with acid-fumaroles. (a) Thick silica-rich soils (~4 m away from vent) with only a minor sulfur enrichment (S = 0.29 wt. %). Soils dominated by amorphous silica and anatase, without a significant presence of sulfate minerals. Alunite group minerals are present in rare instances in SEM (IV13-7). (b) Thin silica-sinter deposits adjacent to active fumarole (several cm away from vent) had elevated sulfur content (S = 2.78 wt. %). Sulfur was incorporated into elemental sulfur, gypsum, and Al-sulfates.

In addition, the vast majority of silica sinter deposits reported in the literature are dominated by hydrated amorphous silica (opal-A), although accessory phases (e.g. alunite, jarosite) can form in acidic sinter deposits (pH 2-6) (e.g. *Jones & Renaut, 2003*). Eastern Valley deposits did not exhibit other secondary minerals or other high-temperature silica phases. *Ruff et al.* (2011) concluded that the lack of other mineral phases, especially sulfates, indicated a near-neutral hot spring setting. However, our study demonstrates that fumarolic acid-leaching can remove the majority of excess sulfur from the system and produce a deposit dominated by amorphous silica (and anatase) without the presence of sulfates. These thick silica-rich soils generated by acid-fumaroles may be an effective analog for Eastern Valley soils (e.g. Lefty Ganote and Kenosha Comets). Therefore, the pH of the fluids and formation mechanism (near-neutral sinter deposition versus acid-sulfate leaching) that formed the silica deposits in the Eastern Valley may not be easily constrained by SO_3 concentrations and the presence or lack of associated sulfate minerals, as this could be the result of either process.

7.2 Jarosite and Spheroidal Hematite at Meridiani Planum

Jarosite ($KFe^{3+}_3(SO_4)_2(OH)_6$) is an important environmental indicator mineral, which has been detected by orbiters (e.g. *Miliken et al., 2008; Bishop et al., 2009; Roach et al., 2010; Thollot et al., 2012*) and the Opportunity rover (Figure 30a) (e.g. *Klingelhofer et al., 2004*) in diverse geologic settings on Mars. In terrestrial environments, jarosite is found in low-pH volcanic sulfur-rich fumarolic deposits, acid-mine drainage (AMD), and saline-acid lakes (e.g. *Elwood Madden et al., 2004; Tosca et al., 2005; Papike et al., 2006; Story et al., 2010*). The stability of jarosite in terrestrial settings has placed constraints on the environmental conditions present in the sulfate-bearing rocks in the Burns Formation at Meridiani Planum that consists of ephemeral mildly to strongly acidic waters with a pH <4.5 and oxidizing conditions, since Fe must be present in ferric form (e.g. *Burns, 1987; Tosca et al., 2005*).

The presence of jarosite in the Meridiani outcrops would also place constraints on the conditions after deposition. *Elwood-Madden et al.* (2004) concluded that low water-rock ratios are needed to preserve the jarosite and Ca-sulfate weathering products, because progress towards equilibrium causes early-formed minerals to become unstable. Therefore, the presence of jarosite in Meridiani outcrops indicates that basaltic weathering on Mars likely did not go to completion. Limited water near the surface/subsurface would explain the presence of soluble sulfate-salts. Perhaps, after deposition from an ephemeral hydrothermal or non-thermal aqueous solution, the solution evaporated and stayed dry until the present day.

In terrestrial systems, jarosite is a relatively unstable mineral and breaks down to form Fe^{3+} oxides and hydroxides; either hematite and/or goethite, depending on the environmental conditions. This is supported by our observations of the relict hydrothermal setting at Lítli-Leirhnjúkur. There, sulfates were limited and clays and hematite dominated the secondary mineral assemblage. At Meridiani Planum, one proposed pathway to form hematite spherules involves the incongruent dissolution of a jarosite precursor; both jarosite and hematite have been proposed to be products of acid-sulfate alteration of basalt (*Morris et al., 2005; Golden et al., 2008; Elwood Madden et al., 2012; McCollom et al., 2013a*). Krafla FeOx spherules are closely associated with jarosite and Fe-bearing natroalunite, providing a natural analog to further support this scenario.

Golden et al. (2008) presented the following model, which is also supported by our studies of acid-sulfate alteration in basalt-hosted volcanic environments at Krafla/Námafjall, and studies elsewhere (Figure 31b-d) (e.g. *Morris et al., 2005; McCollom et al., 2013b*). Acid-sulfate alteration of basaltic materials at Meridiani Planum and Krafla formed Fe (e.g. jarosite), Ca- and Mg-sulfates. The source of sulfur at Meridiani is uncertain; the MER team infers that evaporative conditions of acidic groundwater would enrich S concentrations to form sulfates (*Grotzinger et al., 2005*). Alternatively, S enrichment could be associated with the condensation of fumarolic emissions and/or the exposure and oxidation of iron-sulfides in the presence of water (*Knauth et al., 2005; McCollom & Hynek, 2005*), processes both present at Krafla and Námafjall. Acid-sulfate solutions would have quickly dissolved the primary igneous phases; a scenario supported by only residual presence of igneous Fe-bearing phases and plagioclase, and released Fe into solution to form jarosite and hematite (*Glotch et al., 2006*). Low water-rock ratios are inferred because the bulk chemical composition is basaltic when calculated as S-free (*Morris et al., 2006*), indicating that mobile elements were not removed as would be expected at higher water-rock ratios.

More detailed studies are required to determine the characteristics of hematite at Krafla, but it seems likely that spheroidal hematite there may have similar properties to those synthesized by *Golden et al.* (2008) (Figure 32). Krafla spherules are also similar to spherules in other volcanic settings (e.g. *Morris et al., 2005; McCollom et al., 2013*); though they are substantially smaller than those at Meridiani (which are ~40 to 400x larger than terrestrial hydrothermal spherules). This difference in size may be the result of high-temperature (>100°C) conditions, which would improve the kinetics of spheroidal hematite formation, whereas the Krafla spherules are found in samples at temperatures <70°C. Longer duration of aqueous activity is also inferred at Meridiani Planum, while the altered Krafla and Námafjall substrates were deposited in the last ~35 to 12,000 years and are therefore geologically young features. Prolonged acid-sulfate alteration on Mars could help form more extensive hematite deposits and possibly alunite within the altered siliciclastic materials.

The presence of jarosite at Meridiani was largely determined by Mössbauer spectra of outcrops. A range of synthetic Fe-bearing natroalunite compositions produced by *McCollom et al.* (2013a) yield spectra that closely resemble the Mössbauer spectral signature for jarosite, suggesting that Fe^{3+}-bearing natroalunite should be considered as an alternative to a pure Fe^{3+}-sulfate component in the Merdiani outcrop. The presence of Fe^{3+}-bearing natroalunite in the Burns Formation would indicate variable Fe-Al substitution in the B site.In terrestrial settings, intermediate compositions reflect early stages of acid-sulfate alteration of basaltic rocks in hydrothermal volcanic environments (*McCollom et al., 2013b*). This observation may offer further support for the volcanic origin for the inferred jarosite and hematite deposits at Meridiani (e.g. *McCollom & Hynek, 2005*). Fe-bearing members of the alunite family would also considerably expand the range of possible environmental conditions present at the time of formation. Alunite is thermodynamically stable up to pH 7.5 and under less oxidizing conditions, and can precipitate from Fe^{2+} solutions (*Burns, 1987*). If further evidence determines the Martian ‘blueberries’ formed under hydrothermal conditions, then this would suggest significantly different paleoenvironmental conditions at Meridiani than models that propose low-temperature interaction of sediments with groundwater (e.g. *McLennnan et al., 2005*).

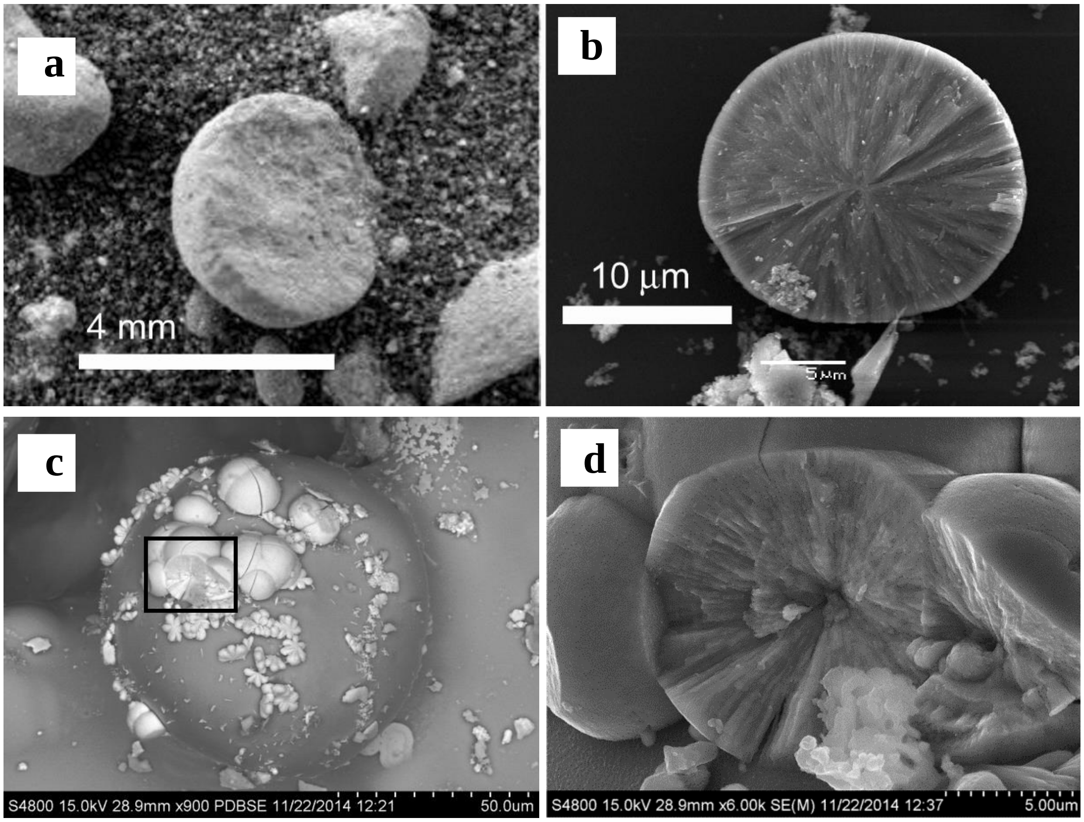

Figure 31: Comparison of hematite spherules from the Burns Formation, experiments by *Golden et al*, and Krafla. (a) Close up image of hematite spherule, (b) experimental hematite spherule from *Golden et al*. (2008), (c) Krafla hematite spherule on top of amorphous silica spheroid, this study, and (d) close-up image exhibiting radial morphology, this study.

7.3 Habitability

Extremophile microbial communities thrive in volcanic hydrothermal systems, which are possible settings for the origin of microbial life on Earth (e.g. *Wächterschäuser, 2006*). These microbial communities harness energy from reduction-oxidation (redox) reactions used to synthesize ATP to power their metabolic processes. Known terrestrial redox couples that support microbial communities involve iron (Fe), sulfur (S), nitrogen (N) and carbon (C), which can act as electron acceptors and/or donors. Potential redox metabolisms on Mars would likely involve anaerobic Fe and S redox cycles given the known environmental, atmospheric, and mineralogical/ geochemical parameters. Terrestrial organisms in this category include iron and sulfur reducing and oxidizing bacteria, and their biomass is mediated by temperature, pH, and redox conditions (e.g. *Krebs et al., 2014*). Iron (Fe) and sulfur (S) species are globally widespread and are significantly more enriched within Martian rocks and soils than on Earth (*McSween et al., 2009*). On Mars, sulfur enrichment may be explained by Noachian-Hesperian volcanism releasing abundant sulfur compounds into the atmosphere, along with the high-Fe composition of Martian basalts.

OMEGA, CRISM, and the MER missions have identified globally distributed mono- and poly-hydrated Mg/Ca/Fe-sulfates within diverse geologic settings that include sedimentary and hydrothermal environments (*Langevin et al., 2005; Yen et al., 2008).* MER Opportunity and Spirit detected iron oxides and oxyhydroxides that include hematite and goethite (*Klingelhofer et al., 2004; Morris et al., 2008*). Hematite may have formed in a variety of settings, but the presence of goethite is indicative of aqueous processes. Other possible hydrothermal or leached iron-sulfide deposits, similar to those sulfate and oxide mineral assemblages in the Krafla and Námafjall area, include Juventae Chasma (*Bishop et al., 2009*) and the etched terrains of Arabia Terra (*Poulet et al., 2008*). The abundance of Fe^{3+} and sulfate phases provides a supply of electron acceptors for Fe- and S-reduction, although electron donors are scarce on Mars.

Abundant Fe^{2+} phases in Martian igneous basalts (e.g. olivine, pyroxene) could serve as electron donors for Fe- and S-oxidation. In terrestrial settings, O_2 or nitrates would be the likely electron acceptors, however; nitrate has not been detected on Mars.

Iron-sulfide deposits have been found in Gale Crater and igneous sulfide is likely to exist on Mars, as it has been identified in SNC meteorites. Most microbial sulfide oxidation occurs under aerobic conditions and without constraints on the NO_3^- concentrations in the atmosphere; there is no known complete oxidation redox couple (*Nixon et al., 2013*). However, iron-oxidizers on Mars can use CO_2 as an electron acceptor, a compound that is abundant in the Martian atmosphere (e.g. *Weber et al., 2006*). In addition, recently detected organic molecules in carbonaceous meteorites could provide a full redox couple to support microbial anaerobic iron and sulfur oxidation on Mars (*Nixon et al., 2012*).

Iron and sulfur redox gradients in localized environments were likely present at or near Home Plate and Meridiani Planum, suggesting potential habitable sites on Mars (*Yen et al., 2008*). Recently, Curiosity revealed the presence of Fe- and S-redox gradients in secondary minerals such as magnetite, sulfide, and sulfate minerals in an ancient lacustrine environment, which could provide the necessary redox couples and aqueous environment to support microbial metabolisms early in the history of Mars (*Grotzinger et al., 2014*). In Gusev Crater, possible chemoautotrophic and acidophilic bacteria could have utilized H_2, H_2S, and elemental sulfur in redox reactions to support metabolic functions in fumarolic Paso Robles soils (*McKay, 1997*). At Meridiani Planum, the paleoenvironment conditions in the sedimentary rocks indicate arid, acidic, and oxidizing conditions. On Earth, microbial communities have adapted to low pH, and episodic and limited water, suggesting that Meridiani may have been habitable when deposition and early diagenesis took place. If hydrothermal conditions were present, redox reactions may have been present to provide energy for thermophilic Fe- and S-oxidizers. However, the environmental conditions inferred in the Paso Robles soils and the Burns Formation may have posed a challenge for prebiotic chemical reactions and the origin of life on early Mars (e.g. *Knoll et al., 2005*).

The investigation of the microbial communities in the Krafla and Námafjall areas is beyond the scope of this project. However, this study provides a mineralogical and geochemical context of Fe- and S-redox gradients in analogous environments on Mars. Investigating the extreme limits of microbial metabolic processes in fumarolic/hot spring environments in Iceland may improve habitability parameters in the search for signs of life on Mars.

8. Conclusions

This study focused on acid-sulfate alteration of Mars-like high-Fe basalts. I investigated the formation mechanisms of secondary minerals in the Krafla and Námafjall geothermal areas, which provide insights for the origin of soils and outcrops in the Gusev Crater and Meridiani Planum on Mars. This study can conclude that in fumarolic and hot spring acid-sulfate environments:

(i) Bulk compositions of alteration products were controlled by the leaching and mobilization of most major elements (e.g. Ca, Mg, Na, K) out of the deposits, while Si, Ti, and Zr were residually enriched. Distinct patterns of alteration around fumaroles/hot springs are highlighted by surficial color, which is a strong indicator of mineral and geochemical composition.

(ii) Most major cations exhibit high mobility in steam-derived acid-sulfate waters (pH <2.5).

(iii) Pyrite oxidation and volcanic vapor condensation produce a series of soluble Fe-and Al-sulfate-salts that eventually break down into the more stable alunite-jarosite group minerals and Fe-(hydr)oxides along the margins of activity.

(iv) The co-occurrence of smectite and jarosite in medium to low activity areas suggests smectite may be able to form *in-situ* under mildly acidic conditions in the presence of high ionic strength solutions.

(v) Amorphous silica, alunite-jarosite group minerals, and spheroidal hematite are a common secondary mineral assemblage derived from acid-sulfate alteration of high-Fe basalts. Alunite-jarosite group minerals had intermediate compositions in the B site (i.e. Fe-bearing natroalunite) that likely reflects hydrothermal acid-sulfate alteration in basalt-hosted volcanic environments.

(vi) Spheroidal hematite lining vesicle walls likely formed from the dissolution of Fe-bearing natroalunite and/or jarosite in Hverir fumaroles. This multistep process is similar to experiments conducted by *Golden et al.* (2008), suggesting a pathway of formation for hematite ‘blueberries’ on Mars. If Fe-bearing natroalunite is the Fe^{3+}-sulfate component in the Burns Formation, this may be a key signature of hydrothermal acid-sulfate alteration.

(vii) Silica-rich soils observed at Hverir and Námaskard had high Si and Ti with low S contents, and lacked sulfate minerals. These observations contradict arguments of *Ruff et al.* (2011) who suggested high water-rock ratios (hot spring settings) are necessary to remove S from the system. Acid fumarole environments were found to produce Si-soils that closely match the geochemical and mineralogical compositions in the Eastern Valley at Gusev Crater, Mars. Therefore, the exact aqueous conditions present at the time of formation are still not fully constrained.

References

Alexander, G. B., Heston, W. M., and Iler, H. K., 1954. The solubility of amorphous silica in water: *Jour. Phys. Chem., 58,* 453-45.

Alpers, C. N., & Brimhall, G. H. (1989). Paleohydrologic evolution and geochemical dynamics of cumulative supergene metal enrichment at la Escondida, Atacama Desert, northern Chile. *Economic Geology and the Bulletin of the Society of Economic Geologists, 84*(2), 229-255.

Andrws-Hanna, J.C., Phillips, R.J., Zuber, M.T. (2007). Meridiani Planum and the global hydrology of Mars. *Nature 446,* 163-166.

Ármannsson, H. (1993). The Geothermal System in Námafjall – Chemical Compilation. Collaboration Project of Landsvikjunar and Orkustofnunar, OS-93053/JHD-29 B, 30p (in Icelandic).

Arnorsson, S. (1995). Geothermal systems in Iceland; structure and conceptual models; I, high-temperature areas. *Geothermics, 24*(5-6), 561-602.

Arnorsson, S., & Andresdottir, A. (1995). Processes controlling the distribution of boron and chlorine in natural waters in Iceland. *Geochimica Et Cosmochimica Acta, 59*(20), 4125-4146.

Arnorsson, S., Fridriksson, T., & Gunnarsson, I. (1998). Gas chemistry of the Krafla geothermal field, Iceland. *Proceedings - International Symposium on Water-Rock Interaction, 9*, 613-616.

Banfield, J.L., Hamilton, V.E., Christensen, P.R. & McSween, H.Y. Jr. (2004). Identification of quartzofeldspathic materials on Mars. *Journal of Geophysical Resarch, 109,* E10009.

Bibring, J. et al. (2005). Mars Surface Diversity as Revealed by the OMEGA/Mars Express Observations. *Science, 207,* 1576-1581.

Bibring, J. et al. (2006). Global Mineralogical and Aqueous Mars History Derived from OMEGA/Mars Express Data. *Science, 312*, 400-404.

Bishop, J. L., Schiffman, P., Murad, E., Dyar, M. D., Drief, A., & Lane, M. D. (2007). Characterization of alteration products in tephra from haleakala, maui; a visible-infrared spectroscopy, mossbauer spectroscopy, XRD, EMPA and TEM study. *Clays and Clay Minerals, 55*(1), 1-17.

Bishop, J.L. et al. (2008). Phyllosilicate diversity and past aqueous activity revealed at Mawrth Vallis, Mars. *Science, 321,* 830-833.

Bishop, J. L. et al. (2009). Mineralogy of juventae chasma: Sulfates in the light-toned mounds, mafic minerals in the bedrock, and hydrated silica and hydroxylated ferric sulfate on the plateau. *Journal of Geophysical Research.E.Planets, 114*

Bjornsson, H. (1977). Konnun a joklum med rafsegulbylgjum. *Natturufraedingurinn, 47*(3-4), 184-194.

Bodvarsson, G. (1961). Physical characteristics of natural heat resources in Iceland. *Jokull, 11,* 29-38.

Bodvarsson, G. S., Benson, S. M., Sigurdsson, O., Stefansson, V., & Eliasson, E. T. (1984). The krafla geothermal field, iceland; 1, analysis of well test data. *Water Resources Research, 20*(11), 1515-1530.

Burns, R. G. (1987). Ferric sulfates on mars. *Journal of Geophysical Research, 92,* E570-E574.

Chassefiere, E. et al. (2004). MEP (mars environment package); toward a package for studying environmental conditions at the surface of mars from future lander/rover missions. *Advances in Space Research, 34*(8), 1702-1709.

Chojnacki, M., & Hynek, B. M. (2008). Geological context of water-altered minerals in Valles Marineris, mars. *Journal of Geophysical Research, 113.*

Christensen, P. R. et al. (2000). Detection of crystalline hematite mineralization on Mars by the Thermal Emission Spectrometer: Evidence for near-surface water. *Journal of Geophysical Research, 105,* 9623-9642.

Christensen, P. R. et al. (2001). Global mapping of Martian hematite mineral deposits: Remnants of water-driven processes on early Mars. *Journal of Geophysical Research, 106*, 23,873-23,885.

Christensen, P. R. et al. (2004). Mineralogy at Meridiani Planum from the Mini-TES Experiment on the Opportunity Rover. *Science, 306*(5702), 1733-1739.

Craddock, R.A., Greeley, R. (2009). Minimum estimates of the amount and timing of gases released into the martian atmosphere from volcanic eruptions. *Icarus, 204*, 512-526.

Desborough, G. A. et al. (2010). Mineralogical and chemical characteristics of some natural jarosites. *Geochimica Et Cosmochimica Acta, 74*(3), 1041-1056.

Ehlmann, B. L., Mustard, J. F., Fassett, C. I., Schon, S. C., Head, James W., I.,II, De Marais, D.,J., Grant, J.A., Murchie, S. L. (2008). Clay minerals in delta deposits and organic preservation potential on mars. *Nature Geoscience, 1*(6), 355-358.

Ehlmann, B. L. et al. (2009). Identification of hydrated silicate minerals on Mars using MRO-CRISM: Geologic context near Nili Fossae and implications for aqueous alteration. *Journal of Geophysical Research, 114,* E00D08.

Ehlmann, B. L., Mustard, J. F., & Bish, D. L. (2010). Weathering and hydrothermal alteration of basalts in Iceland; mineralogy from VNIR, TIR, XRD, and implications for linking mars orbital and surface datasets. *Abstracts of Papers Submitted to the Lunar and Planetary Science Conference, 41.*

Einarsson, P. (2008). Plate boundaries, rifts and transforms in Iceland. *Jokull, 58*, 1-24.

El Maarry, R.M. et al. (2012). Searching for evidence of hydrothermal activity at Apollinaris Mons, Mars. *Icarus, 217*(1), 297-314.

Elwood Madden, ,M.E., Madden, A. S., Rimstidt, J. D., Zahrai, S., Kendall, M. R., & Miller, M. A. (2012). Jarosite dissolution rates and nanoscale mineralogy. *Geochimica Et Cosmochimica Acta, 91*, 306-321.

Elwood-Madden, M. E. E., Bodner, R. J., Rimstidt, J. D. (2004). Jarosite as an indicator of water-limited chemical weathering on Mars. *Nature, 431*, 821-823.

Fernandez-Remolar, D. et al. (2004). The Tinto River, and extreme acidic environment under control of iron, as an analog of the Terra Meridiani hematite site of Mars. *Planetary and Space Sciences, 52*, 239-248.

Fernandez-Remolar, D., Morris, R. V., Gruener, J. E., Amils, R., & Knoll, A. H. (2005). The rio tinto basin, spain: Mineralogy, sedimentary geobiology, and implications for interpretation of outcrop rocks at meridiani planum, mars. *Earth and Planetary Science Letters*, *240*(1), 149-167.

Franzson et al. (2011). Icelandic Hyaloclastite Tuffs. Petrophysical Properities, Alteration and Geochemical Mobility. *Prepared for National Energy Authroity and Reykjavik Energy*. Report no. ISOR-2011/064.

Gaillard, F., & Scaillet, B. (2009). The sulfur content of volcanic gases on mars. *Earth and Planetary Science Letters*, *279*(1-2), 34-43.

Geptner, A. R. (2005). Hydrothermal fossilization of microorganisms at the earth's surface in iceland. *Lithology and Mineral Resources, 40*(6), 505-520.

Geptner, A. R., Ivanovskaya, T. A., Pokrovskaya, E. V., Lyapunov, S. M., Savichev, A. T., Gorbunov, A. V., & Gor'kova, ,N.V. (2007). Hydrothermally altered hyaloclastites at the earth's surface in the rift zone of iceland; problem of the biochemogenic accumulation of trace elements. *Lithology and Mineral Resources, 42*(5), 453-476.

Gendrin, A., et al. (2005). Sulfates in Martian layered terrains; the OMEGA/Mars express view. *Science*, *307*(5715), 1587-1591.

Glotch, T., Bandfield, J. (2006). Determination and interpretation of surface and atmospheric Miniature Thermal Emission Spectrometer spectral end-members at the Meridiani Planum landing site. *Journal of Geophysical Research, 111*, E12S06.

Glotch, T., Bandfield, J. L., Christensen, P.R., Calvin, W.M., McLennan, S.M., Clark, B.C., ROogers, A.D., Squyres, S.W. (2006). Mineralogy of the light-toned outcrop at

Meridiani Planum as seen by the Miniature Thermal Emission Spectrometer and implications for its formation. *Journal of Geophysical Research, 111*, E12S03.

Golden, D. C., Ming, D.W., Morris, R.V., Graff, T.G. (2008). Hydrothermal synthesis of hematite spherules and jarosite: Implications for diagenesis and hematite spherule formation in sulfate outcrops at Meridiani Planum, Mars. *American Mineralogist, 93,* 1201-1214.

Golden, D. C., Ming, D. W., & Morris, R. V. (2010). Spherulitic growth of hematite under hydrothermal conditions; insights into the growth mechanism of hematite spherules at meridiani planum, mars. *Abstracts of Papers Submitted to the Lunar and Planetary Science Conference, 41*, Abstract 2541.

Grönvold, K. (1984). Mývatn fires 1724-1729. Chemical composition of the lava. *Nord. Volc. Inst. Report 8401*.

Grotzinger, J.P. et al. (2014). A Habitable Fluvio-Lacustrine Environment at Yellowknife Bay, Gale Crater, Mars. *Science, 343*(6169), 1-14.

Gudmundsson, B. Th., Arnorsson, S. (2002). Geochemical monitoring of the Krafla and Námafjall geothermal areas, N-Iceland. *Geothermics*, *31*, 195-243.

Gudmundsson, B. T., & Arnorsson, S. (2005). Secondary mineral-fluid equilibria in the Krafla and Námafjall geothermal systems, Iceland. *Applied Geochemistry, 20*(9), 1607-1625.

Heald, P., Foley, N.K., Hayba, D.O. (1987). Comparative anatomy of volcanic-hosted epithermal deposits: acid-sulphate and adularia-sericite types. *Economic Geology, 82,* 1-26.

Hynek, B. M., & Phillips, R. J. (2001). Evidence for extensive denudation of the martian highlands. *Geology, 29*(5), 407-410.

Hynek, B. M., McCollom, T. M., & Rogers, K. L. (2011). Cerro Negro volcano, Nicaragua; an assessment of geological and potential biological systems on early mars. *Special Paper - Geological Society of America, 483*, 279-285.

Hynek, B. M., McCollom, T. M., Marcucci, E. C., Brugman, K., & Rogers, K. L. (2013). Assessment of environmental controls on acid-sulfate alteration at active volcanoes in Nicaragua; applications to relic hydrothermal systems on mars. *Journal of Geophysical Research: Planets, 118,* 2083-2104.

Jones, B., Renaut, R.W. (2003). Hot springs and geysers sinters: The integrated product of precipitation, replacement, and deposition. *Can. J. Earth Sci, 40,* 1549-1569.

Juliani, C. et al. (2005). Paleoproterozoic high-sulfidation mineralization in the Tapajos gold province, Amazonian Craton, Brazil: Geology, mineralogy, alunite argon age, and stable-isotope constraints. *Chem. Geol.*, *215*, 95-125.

Kaasalainen, H., & Stefansson, A. (2011). Sulfur speciation in natural hydrothermal waters, Iceland. *Geochimica et Cosmochimica Acta, 75*, 2777-2791.

Kaasalainen, H., & Stefansson, A. (2012). The chemistry of trace elements in surface geothermal waters and steam, Iceland. *Chemical Geology, 330-331*, 60-85.

Kandori, K. et al. (2000). Definitive effects of chloride ions on the formation of spherical hematite particles in a forced hydrolysis reaction. *Phys Chem. & Chem. Phys., 2,* 3293-3299.

Karakaya, N., Karakaya, M.C., Nalbantcilar, M.T., Yavuz, F. (2007). Relation between spring-water chemistry and geothermal alteration in the Saplica volcanic rocks, Sebinkarahisar. J. *Geochem. Explor, 93,* 35-46

King, P. L., & McSween, H. Y., J. (2005). Effects of H (sub 2) O, pH, and oxidation state on the stability of fe minerals on mars. *Journal of Geophysical Research, 110,* E12S10.

Klingelhofer, G. et al. (2004) Jarosite and Hematite at Meridiani Planum from Opportunities Mossbauer Spectrometer. *Science, 206,* 1740—1745.

Knauth, L. P., Burt, D. M., & Wohletz, K. H. (2005). Impact origin of sediments at the opportunity landing site on mars. *Nature, 438*(7071), 1123-1128.

Knoll, A. H et al. (2005). An astrobiological perspective on Meridiani Planum. *Earth and Planetary Science Letters, 240*, 179-189.

Koornneef, J.M. et al. (2011). Melting of a Two-component Source beneath Iceland. *Journal of Petrology, 53*(1), 127-157.

Krauskopf, K. B. (1959). The geochemistry of silica in sedimentary environments. *Special Publication - Society of Economic Paleontologists and Mineralogists, 7,* 4-19.

Krebs, J.E. et al. (2014). Microbial Community Structures of Novel Icelandic Hot Spring Systems Revealed by phlyChip G3 Analysis. *Astrobiology, 14*, 229-240.

Kristmanndottir, H. (1982). Alteration in the IRDP drill hole compared with other holes in Iceland. *Journal of Geophysical Research. 87*, 6525-6531.

Lane, M. D., Bishop, J. L., Dyar, M. D., King, P. L., Parente, M., & Hyde, B. C. (2008). Mineralogy of the paso robles soils on mars. *American Mineralogist, 93*(5-6), 728-739.

Langevin, Y., Poulet, F., Bibring, J., Gondet, B., & Hanson, B. (2005). Sulfates in the north polar region of mars detected by OMEGA/Mars express. *Science, 307*(5715), 1584-1586.

Lanz, J. K., & Saric, M. B. (2009). Cone fields in SW elysium planitia; hydrothermal venting on mars? *Journal of Geophysical Research, 114,* E02008.

Lonker, S. W., Franzson, H., & Kristmannsdottir, H. (1993). Mineral-fluid interactions in the reykjanes and svartsengi geothermal systems, iceland. *American Journal of Science, 293*(7), 605-670.

Maclennan, J., Jull, M., McKenzie, D., Slater, L., Gronvold, K. (2002). The link between volcanism and deglaciation in Iceland. *Geochemistry, Geophysics, Geosystems, 3*(11), 1-25.

Manga, M., Patel, A., Dufek, J., & Kite, E. S. (2012). Wet surface and dense atmosphere on early mars suggested by the bomb sag at home plate, mars. *Geophysical Research Letters, 39*(1).

Markusson, S. H., & Stefansson, A. (2011). Geothermal surface alteration of basalts, Krýsuvík Iceland; alteration mineralogy, water chemistry and the effects of acid supply on the alteration process. *Journal of Volcanology and Geothermal Research, 206*(1-2), 46-59.

McCollom, T. M., & Hynek, B. M. (2005). A volcanic environment for bedrock diagenesis at Meridiani Planum on mars. *Nature, 438*(7071), 1129-1131.

McCollom, T. M., Robbins, M., Moskowitz, B., Berquo, T. S., Joens, N., & Hynek, B. M. (2013). Experimental study of acid-sulfate alteration of basalt and implications for sulfate deposits on mars. *Journal of Geophysical Research: Planets, 118*(4), 577-614.

McCay, C.P. (1997). The search for life on Mars. *Origins Life Evol. Biosphere, 27*, 263-289.

McLennan, S.M. et al. (2013). Elemental Geochemistry of Sedimentary Rocks at Yellowknife Bay, Gale Crater, Mars. *Science, 343*(6169), 1-10.

McHenry, L. J. (2009). Element mobility during zeolitic and argillic alteration of volcanic ash in a closed-basin lacustrine environment: Case study Olduvai Gorge, Tanzania. *Chemical Geology,* 265, 540-552.

McHenry L. J., Chevrier, V., Schroder, C. (2011). Jarosite in a Pleistocene East African saline-alkaline paleolacustrine deposit: Implications for Mars aqueous geochemistry. *Journal of Geophysical Research, 116,* E04002.

McLennan, S. M. et al. (2005). Provenance and diagenesis of the evaporate-bearing Burns Formation, Meridiani Planum, Mars. *Earth and Planetary Science Letters, 240*, 95-121.

McSween, H. Y. et al. (2008). Mineralogy of volcanic rocks in Gusev crater, mars; reconciling Mossbauer, alpha particle X-ray spectrometer, and miniature thermal emission spectrometer spectra. *Journal of Geophysical Research, 113*.

McSween, H. Y., Taylor, J., Wyatt, M. B. (2009). Elemental composition of the Martian curst. *Science, 324,* 736-739.

Miliken, R. E. et al. (2008). Opaline silica in young deposits on Mars. *Geology, 36*(11), 847-850.

Ming, D. W. et al. (2006). Geochemical and mineralogical indicators for aqueous processes in the Columbia hills of Gusev crater, mars. *Journal of Geophysical Research, 111*.

Ming, D. W. et al. (2008). Geochemical properties of rocks and soils in Gusev crater, mars; results of the alpha particle X-ray spectrometer from Cumberland ridge to home plate. *Journal of Geophysical Research, 113*.

Morris, R. V., Ming, D. W., Graff, T. G., Arvidson, R. E., Bell F,,III, Squyres, S. W., Robinson, G. A. (2005). Hematite spherules in basaltic tephra altered under aqueous, acid-sulfate conditions on Mauna Kea volcano, Hawaii; possible clues for the occurrence of hematite-rich spherules in the burns formation at Meridiani Planum, mars. *Earth and Planetary Science Letters, 240*(1), 168-178.

Morris, R. V., Klingelhoefer, G., Schroeder, C., Rodionov, D. S., Yen, A., Ming, D. W., Arvidson, R. E. (2006). Mossbauer mineralogy of rock, soil, and dust at Meridiani Planum, mars; opportunity's journey across sulfate-rich outcrop, basaltic sand and dust, and hematite lag deposits. *Journal of Geophysical Research, 111*.

Morris, R. V., Klingelhoefer, G., Schroeder, C., Fleischer, I., Ming, D. W., Yen, A. S., Squyres, S. W. (2008). Iron mineralogy and aqueous alteration from husband hill through home plate at Gusev crater, mars; results from the Mossbauer instrument on the spirit mars exploration rover. *Journal of Geophysical Research, 113*.

Mustard, J. F. et al. (2008). Hydrated silicate minerals on Mars observed by the Mars Reconnaissance Orbiter CRISM instrument. *Nature, 454,* 305-309.

Nesbitt, H.W., Wilson, R,E. (1992). Recent chemical weathering of basalts. *American Journal of Science, 292*(10), 740-777.

Nicholson, H. et al. (1991). Geochemical and isotopic evidence for crustal assimilation beneath Krafla, Iceland. *Journal of Petrology, 32,* 1005-1020.

Nicholson, H., & Latin, D. (1992). Olivine tholeiites from Krafla, Iceland; evidence for variations in melt fraction within a plume. *Journal of Petrology, 33*(5), 1105-1124.

Niles, P. B., & Michalski, J. R. (2009). The origin of the Meridiani sediments; the key for understanding the formation of sulfates and layered deposits on mars. *Abstracts of Papers Submitted to the Lunar and Planetary Science Conference, 40*.

Nixon, S.L., Cockell, C.S., Tranter, M. (2013). Plausible microbial metabolisms on Mars. *Astron Geophys, 54,* 13-16.

Nixon, S.L., Cockell, C.S., Tranter, M. (2012). Limitations to a microbial iron cycle on Mars. *Planetary and Space Sciences, 72*, 116-128.

Nordstrom, D. K., & Alpers, C. N. (1999). Geochemistry of acid mine waters. *Reviews in Economic Geology, 6A*, 133-160.

Oliva-Urcia, B., & Kontny, A. (2012). Remanent magnetization of maghemitized basalts from krafla drill cores, NE-iceland.*Studia Geophysica Et Geodaetica, 56*(3), 641-657.

Papike, J. J., Karner, J. M., & Shearer, C. K. (2006). Comparative planetary mineralogy; implications of martian and terrestrial jarosite; a crystal chemical perspective. *Geochimica Et Cosmochimica Acta, 70*(5), 1309-1321.

Papike, J. J. et al. (2007). Terrestrial analogs of martian jarosites; major, minor element systematics and na-K zoning in selected samples. *American Mineralogist, 92*(2-3), 444-447.

Papike, J. J., Karner, J. M., Shearer, C. K., & Burger, P. V. (2009). Silicate mineralogy of martian meteorites. *Geochimica Et Cosmochimica Acta, 73*(24), 7443-7485.

Payne, J.H., Mau, K.T. (1946). A study of the chemical alteration of basalt in the Kilauea region of Hawaii. *Journal of Geology, 54*(6), 345-358.

Peretyazhko, T., Sutter, B., Ming, D.W. (2014). Alteration of basaltic glass to Mg/Fe-smectite under acidic conditions: A potential smectite formation mechanisms on Mars. *Clay Mineral Society* abstracts.

Poulet, F., Arvidson, R. E., Gomez, C., Morris, R. V., Bibring, J. P., Langevin, Y., . . . Griffes, J. (2008). Mineralogy of terra meridiani and western arabia terra from OMEGA/MEx and implications for their formation. *ICARUS, 195*(1), 106-130.

Reardon, E.J., Beckie, R.D. (1987): Modelling chemical-equilibria of acid-mine drainage - the FeSO4-H2SO4-H2O system. *Geochim. et Cosmochim. Acta, 51*(9), 2355–2368.

Rice, M. S. et al. (2010). Silica-rich deposits and hydrated minerals at Gusev Crater, Mars; VIS-NIR spectral characterization and regional mapping. *Icarus, 205*(2), 375-395.

Roach, L. H., Mustard, J. F., Lane, M. D., Bishop, J. L., & Murchie, S. L. (2010). Diagenetic haematite and sulfate assemblages in valles marineris. *ICARUS, 207*(2), 659-674.

Ruff, S. W. et al. (2011). Characteristics, distribution, origin, and significance of opaline silica observed by the spirit rover in Gusev crater, mars. *Journal of Geophysical Research, 116*.

Ruff, S.W. (2015). New observations reveal a former hot spring environment with high habitability and preservation potential in Gusev Crater, Mars. *46th Lunar and Planetary Sciences* Abstracts.

Saemundsson, K. (1967). Vulcanismus und Tektonik des Hengill-Gebietes in Sudwest-Island. *Acta Naturalia Island, 11*, 1-105.

Saemundsson, K. (1991). The geology of the Krafla system. *In: Nattura Myvatns, ed. Arnpor Gardarsson and Arni Einarsson. HIN*, 24-95.

Saemundsson, K., Hjartarson, A., Kaldal, I., Sigurgeirsson, M.A., Kristinsson, S.G. and Vikingsson, S. (2012). *Geological Map of the northern Volcanic Zone, Iceland. Northern Part. 1:100,000*. Reykjavik: Iceland GeoSurvey and Landsvierkjun.

Schmidt, M. E. et al. (2008). Hydrothermal origin of halogens at home plate, Gusev crater. *Journal of Geophysical Research, 113*, 0-Citation E06S12.

Schmidt, M. E. et al. (2009). Spectral, mineralogical, and geochemical variations across home plate, Gusev crater, mars indicate high and low temperature alteration. *Earth and Planetary Science Letters, 281*(3-4), 258-266.

Scott, D.H., and Carr, M.H. (1978). Geologic map of Mars: U.S. Geological Survey Miscellaneous Investigations Series Map I–1083, scale 1:25,000,000.

Skok, J. R., Mustard, J. F., Ehlmann, B. L., Milliken, R. E., & Murchie, S. L. (2010). Silica deposits in the nili patera caldera on the syrtis major volcanic complex on mars. *Nature Geoscience, 3*(12), 838-841.

Sims, K. W. W., Maclennan, J., Blichert-Toft, J., Mervine, E. M., Blusztajn, J., & Gronvold, K. (2013). Short length scale mantle heterogeneity beneath iceland probed by glacial modulation of melting. *Earth and Planetary Science Letters,379*, 146-157.

Squyres, S. W. et al. (2004). The spirit rover's Athena science investigation at Gusev crater, mars. *Science, 305*(5685), 794-799.

Squyres, S W. et al. (2005). Sedimentary rocks at Meridiani Planum: Origin diagenesis, and implications for life on Mars. *Earth and Planetary Sciences, 240*, 1-10.

Squyres, S. W. et al. (2006). Rocks of the Columbia hills. *Journal of Geophysical Research, 111*, 0-E02S11.

Squyres, S.W. et al. (2007). Pyroclastic Activity at Home Plate in Gusev Crater, Mars. *Science, 316*, 738-742.

Squyres, S. W. et al. (2008). Detection of silica-rich deposits on mars. *Science, 320*(5879), 1063-1067.

Stefansson, V. (1981). The Krafla geothermal field, north-east Iceland. In: L. Rybach and L.J.P. Muffler (eds) Geothermal Systems: Principles and Case Histories. Wiley, New York, N.Y. 273-294.

Stefansson, A., Gislason, S.R., Arnorsson, S. (2001). Dissolution of primary minerals in natural waters II: Mineral saturation state. *Chemical Geology, 172*, 251-276.

Stefansson, A., Arnorsson, S. (2002) Gas pressures and redox reactions in geothermal fluids in Iceland. *Chemical Geology, 190*, 251-271

Stoffregen, R. E., Alpers, C.N., Jambor J.L. (2000). Alunite-jarosite crystallography, thermodynamics, and geochronology, in Sulfate Minerals: Crystallography, Geochemistry, and Environmental Significance, Rev. Mineral. Geochem, edited by C. N. Alpers et al., pp. 453-479, Mineral. Soc. Amer., Washington, D. C.

Stoiber, R.E., and Rose, W.I. (1974). Fumarole incrustations at active Central American volcanoes. *Geochim. Cosmochim. Acta, 38*,495–516.

Story, S., Bowen, B. B., Benison, K. C., & Schulze, D. G. (2010). Authigenic phyllosilicates in modern acid saline lake sediments and implications for mars. *Journal of Geophysical Research, 115*, E12012.

Stroncik, N.A., Schminke, H.U. (2001). Palagonite – a review. *International Journal of Earth Science, 91*, 680-697.

Tanaka, K.L.. (1986). The stratigraphy of Mars, in Proceedings of the Lunar and Planetary Science Conference. *Journal of Geophysical Research, 91*, 139–158.

Thollot, P. et al. (2012). Most mars minerals in a nutshell: Various alteration phases formed in a single environment in noctis labyrinthus. *Journal of Geophysical Research, 117*(00).

Tobler, D.J., Stefansson, A., Benning, L.G. (2008). *In-situ* grown silica sinters in Icelandic geothermal areas. *Geobiology, 6*(5), 481-502.

Tosca, N. J., McLennan, S. M., Hindsley, D. H., & Schoonen, M. A. A. (2004). Acid-sulfate weathering of synthetic Martian basalt; the acid fog model revisited. *Journal of Geophysical Research, 109*, 29.

Tosca, N. J. et al. (2005). Geochemical modeling of evaporation processes on Mars: Insight from the sedimentary record at Meridiani Planum. *Earth and Planetary Science Letters, 240*, 122-148.

Velde, B. (Ed.) (1995). *Origin and Mineralogy of Clays*, Springs, New York.

Wang, A., & Ling, Z. C. (2011). Ferric sulfates on mars; a combined mission data analysis of salty soils at gusev crater and laboratory experimental investigations. *Journal of Geophysical Research, 116*, E00F17.

Weber, K. et al. (2006). Microorganisms pumping iron: anaerobic microbial iron oxidation and reduction. *Applied Environmental Microbiology, 72*, 686.

Wolfe, C. J., Bjarnason, I. T., VanDecar, J. C., & Solomon, S. C. (2002). Assessing the depth resolution of tomographic models of upper mantle structure beneath iceland. *Geophysical Research Letters, 29*(2), 4.

Wray, J. J. et al. (2009). Phyllosilicates and sulfates at endeavour crater, meridiani planum, mars. *Geophysical Research Letters, 36*(21).

Wyatt, M. B., & McSween,Harry Y.,,Jr. (2002). Spectral evidence for weathered basalt as an alternative to andesite in the northern lowlands of mars. *Nature (London), 417*(6886), 263-266.

Yen, A. S. et al. (2008). Hydrothermal processes at Gusev crater; an evaluation of Paso robles class soils. *Journal of Geophysical Research, 113*.

Zolotov, M. Y., & Shock, E. L. (2005). Formation of jarosite-bearing deposits through aqueous oxidation of pyrite at Meridiani Planum, Mars. *Geophysical Research Letters, 32*(21), 5.

Appendix A

Field Photos

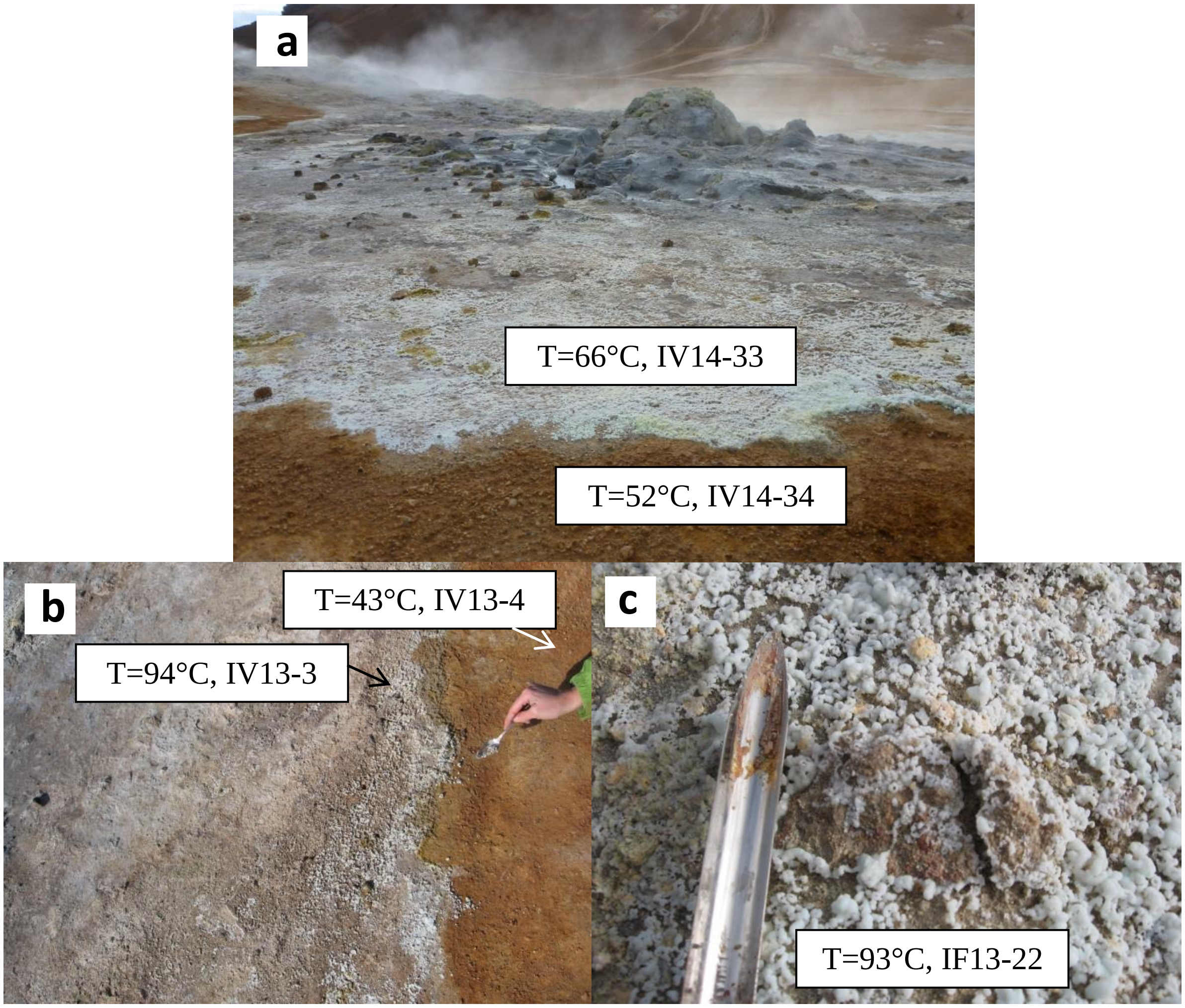

Figure 32: Field photos of hot springs (mud pots) from the Krafla and Námafjall area. (a) Samples IV14-33, -34 and (b) samples IV13-3, -4 from the Hverir geothermal field. (b) Sample IF13-22 from Víti Crater.

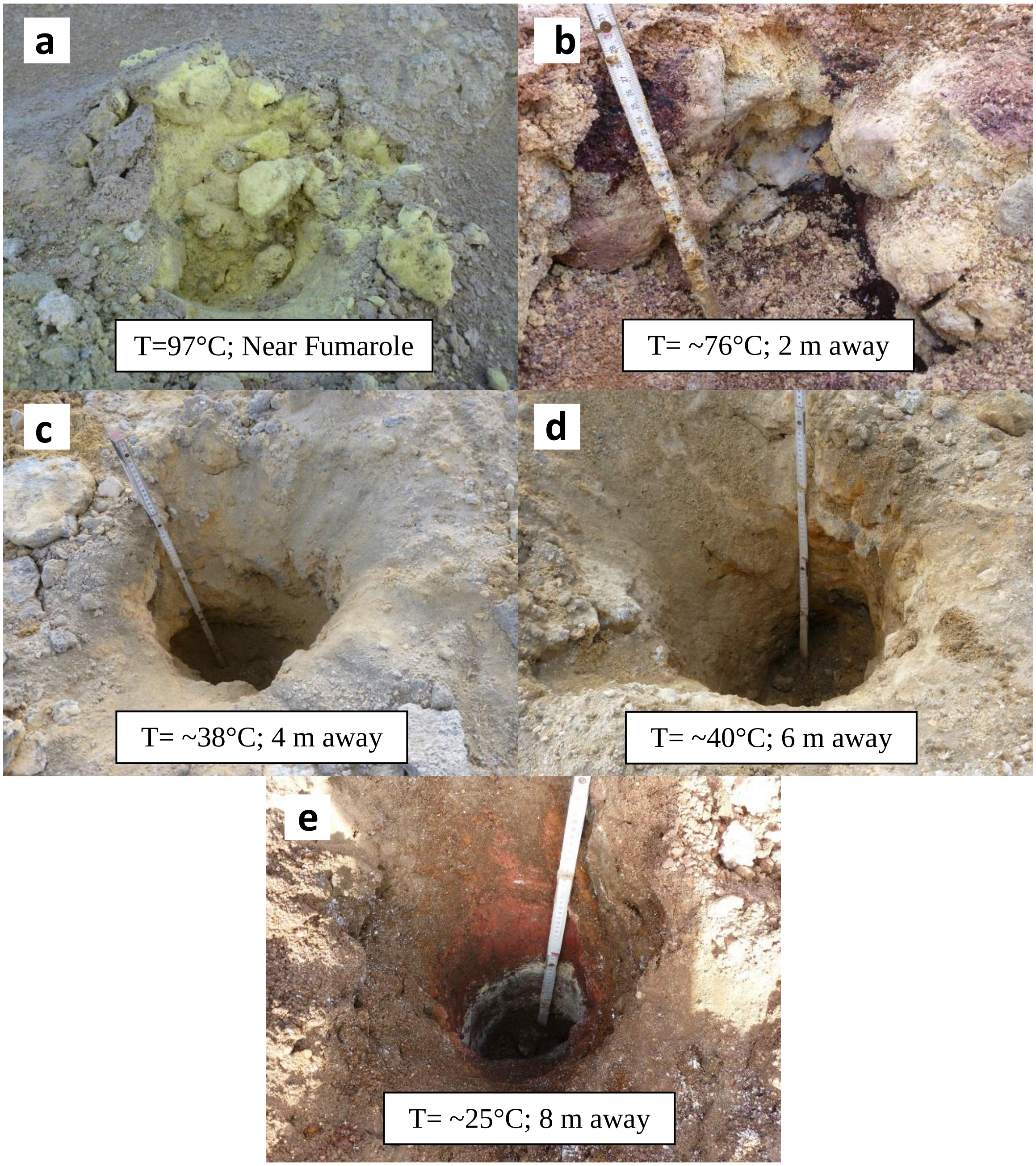

Figure 33: Field photos of the fumarole from the Hverir alteration apron. (a) Sample IV14-20, (b) samples IV14-06 through -12, (c) sample IV14-13, (d) samples IV14-14 through -16, and (e) samples IV14-17 through -19.

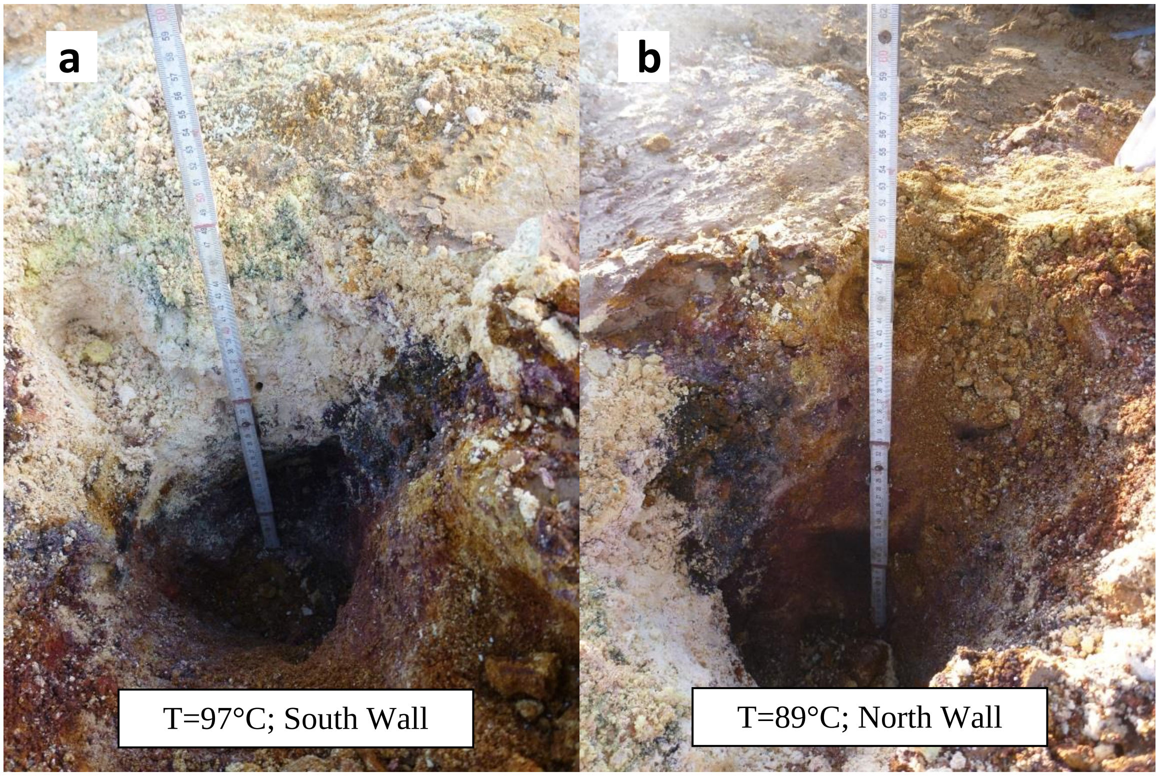

Figure 34: Field photos of fumaroles from Leirhnjúkur. (a) South and (b) north wall of depth profile that contain samples IV14-30 through 32.

Appendix B

Supplementary SEM Images

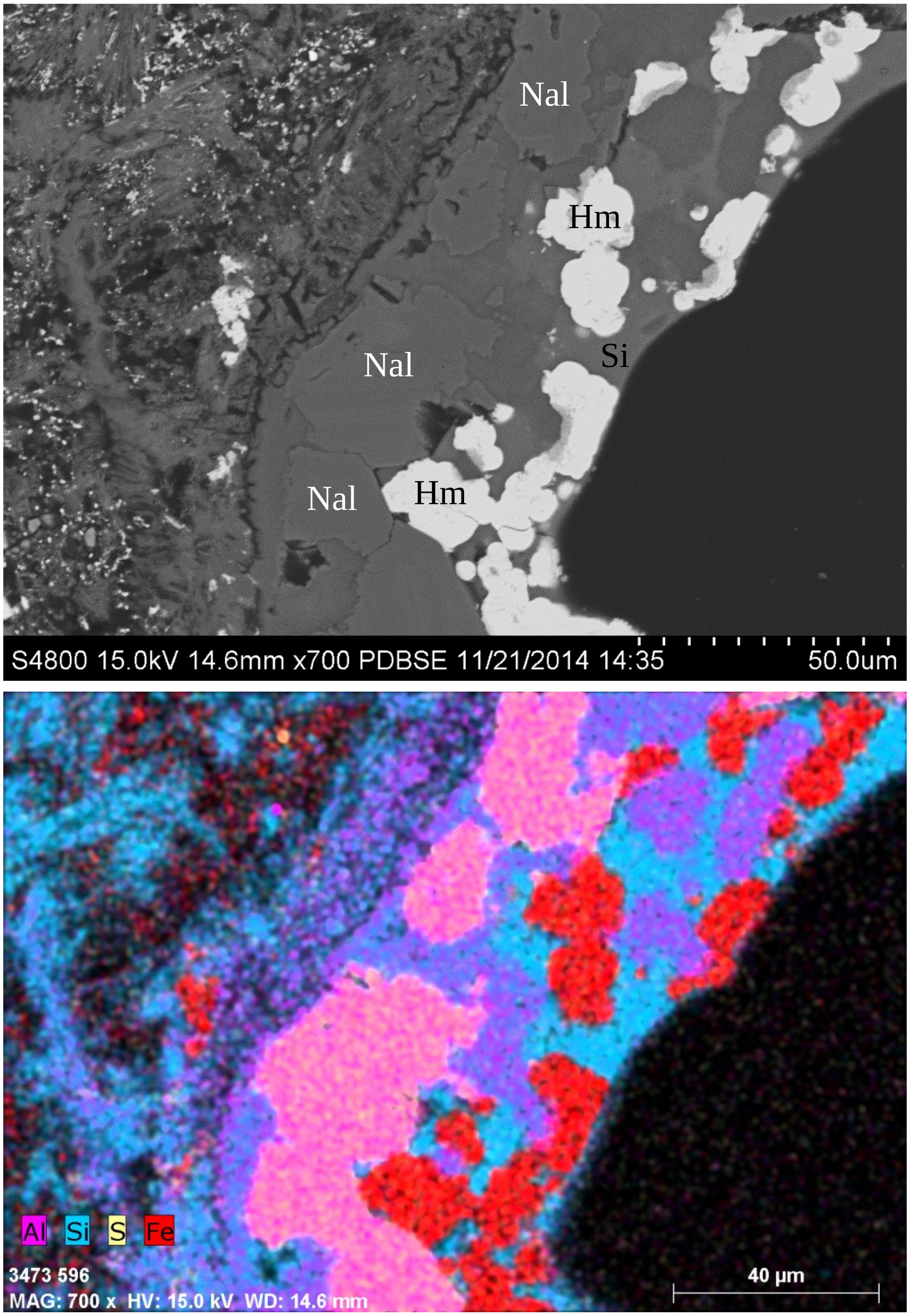

Figure 35: SEM image of sample IV13-13: (a) An altered basalt with mineral precipitates (amorphous silica, natroalunite, and hematite) forming along a vesicle wall. (b) Element dot map generated by EDS highlights the S-bearing phase (natroalunite), Fe-bearing phase (hematite), and the Si-bearing phase (amorphous silica). Nal = natroalunite, Hm = hematite, Si = amorphous silica.

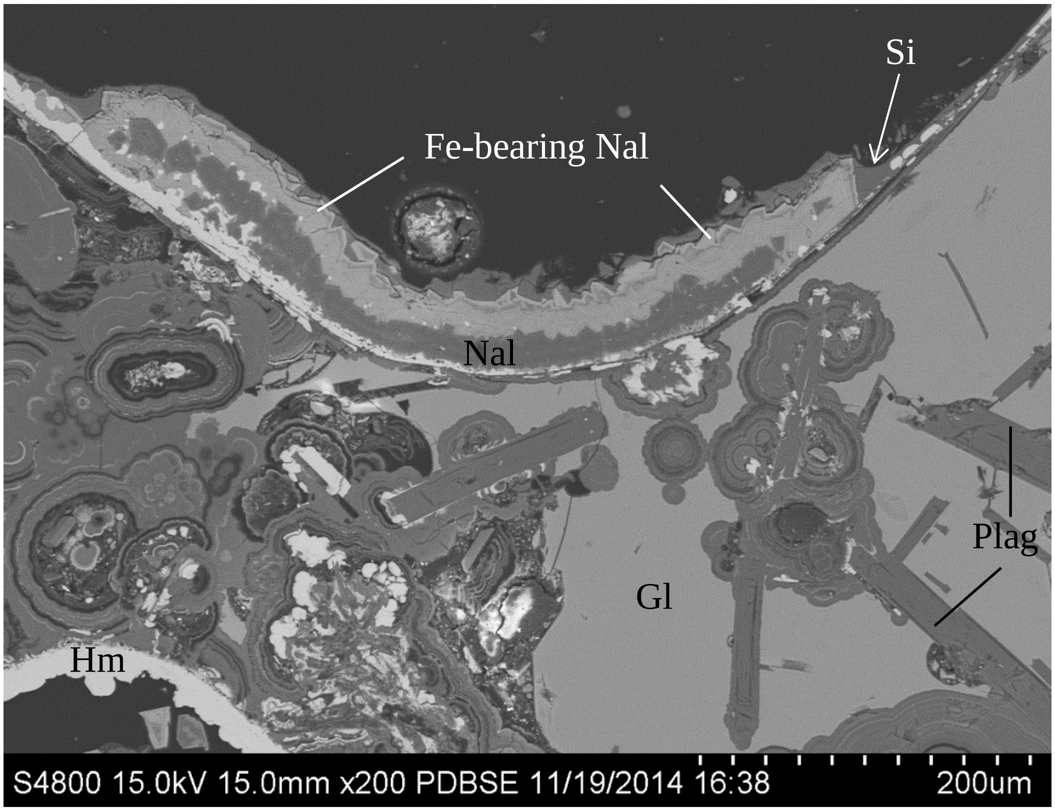

Figure 36: SEM image of sample IV13-14: Altered basalt with natroalunite (dark cubes) and Fe-bearing natroalunite (white cubes) coated by amorphous silica along the same vesicle wall. The Nal = natroalunite, Hm = hematite, Si =amorphous silica, Gl = basaltic glass, Plag = remnant plagioclase laths.

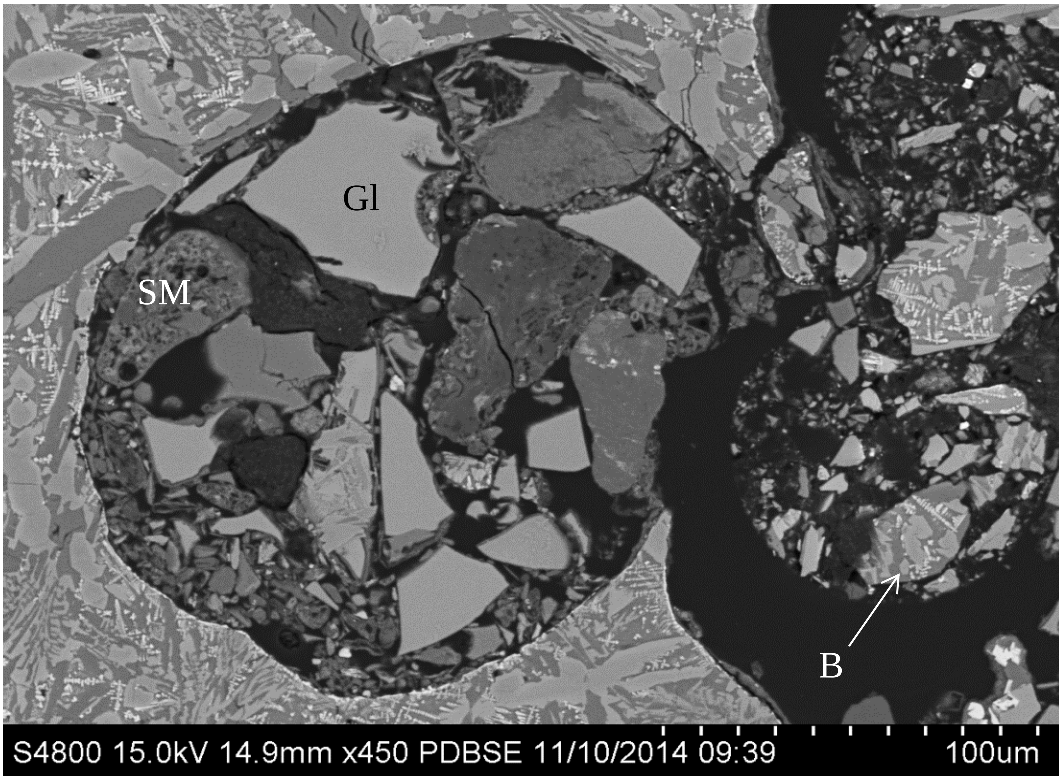

Figure 37: SEM image of sample IV13-11: Slightly altered vesicular basalt along the margins of the Hverir fumarolic apron. Basaltic glass and secondary minerals are partially-filling a vesicle compared to amorphous silica and sulfate minerals in the purple and red alteration zones. Secondary minerals have not been identified, but smectites and zeolites are likely based on results from XRD and EDS analysis. B = piece of basalt, Gl = basaltic glass, SM = secondary minerals.

Appendix C

Detailed List of Samples

Table 7: List of all samples separated into sample type, location, thermal feature present, temperature, substrate, and mineral assemblage[a]

ID No.	Sample Location	Substrate	Thermal Feature	T°C	Distance[b,c]	Mineral Assemblage
White precipitate						
IV13-3	Hverir	?	mud pot	94.3	x	Halotrichite-Pickingerite, Gypsum, Szomolnokite
IV14-33	Hverir	?	mud pot	66.2	x	Epsomite, Gypsum, Halotrichite, Starkeyite
IF13-12	Leirhnjúkur	hyaloclastite	mud pot	83.6	20 – 50	Halotrichite-Pickingerite
IF13-22	Víti Crater	?	mud pot	93.5	x	Pickeringite, Rozenite, Gypsum
IV14-27	Námaskard	hyaloclastite	fumarole	85	x	Gypsum, Pickeringerite, Rozenite
Orange precipitate/sediment						
IV13-4	Hverir	?	mud pot	43.7	x	Anatase, Alunogen, Hematite, Goethite, Jarosite, Smectite (Montmorillonite)
IV14-34	Hverir	?	mud pot	52.2	x	Anatase, Alunogen, Chaclcocyanite?, Jarosite, Quartz, Rostite, Smectite (Montmorillonite), Zeolite
IF13-14	Leirhnjúkur	hyaloclastite	mud pot	38.1	40 – 80	Igneous (Plagioclase), Alunogen, Hematite, Jarosite, Quartz, Rostite
IJ13-1	Námaskard	hyaloclastite	fumarole	36	34 - 40	Igneous (plagioclase, augite), Alunogen, Anatase, Gypsum, Hematite, Quartz, (Natro)alunite/jarosite, Smectite (Montmorillonite)
IF14-23	Leirhnjúkur	hyaloclastite	fumarole	56.4	x	Alunite, Alunogen, Goethite, Magnetite, Quartz, Rostite, Stellerite
IF13-6	Leirhnjúkur	basalt	fumarole	30.6	100 - 120	Igneous (Plagioclase), Alunogen, Hematite, Kaolinite, (Natro)alunite/jarosite, Quartz, Smectite (Nontronite), Zeolite
Gray mud						

IV14-30	Námaskard	hyaloclastite	mud pot	75.2	x	Anatase, Kaolinite, Marcasite, Pyrite
IV14-32	Námaskard	hyaloclastite	mud pot	51.1	x	Alunite, Amorphous Silica, Anatase, Elemental Sulfur, Natroalunite, Rhomboclase?
IV13-2	Hverir	?	mud pot	71.5	0	Amorphous Silica, Alunogen, Anatase, Elemental Sulfur, Kaolinite, Pyrite
IF13-17	Leirhnjúkur	hyaloclastite	fumarole	56.4	x	Amorphous Silica, Anatase, Halloysite, Marcasite, Pyrite, Quartz
IF13-15	Leirhnjúkur	hyaloclastite	fumarole	93.7	x	Amorphous silica, Elemental Sulfur, Kaolinite, Natroalunite, Rhomboclase
Sulfur-rich						
IF14-24	Leirhnjúkur	hyaloclastite	fumarole	97	x	Anatase, Elemental Sulfur, Rostite
IF13-16	Leirhnjúkur	hyaloclastite	hot spring	35.2	0	Anatase, Alunogen, Elemental sulfur, Hematite, Kaolinite, Rostite
IF13-1	Leirhnjúkur	basalt	fumarole	<100	0	Amorphous silica, Anatase, Elemental Sulfur, Hematite, Rhomboclase
IF13-2	Leirhnjúkur	basalt	fumarole	97	0	Anatase, Elemental Sulfur, Rhomboclase
IF13-8	Leirhnjúkur	basalt	fumarole	97.2	0	Anatase, Elemental Sulfur
IV14-19	Hverir	basalt	fumarole	39.9	x	Amorphous Silica, Alunogen, Anatase, Elemental Sulfur
IV13-5	Hverir	basalt	fumarole	97.8	0	Sulfur
Silica-rich						
IJ13-8	Námaskard	hyaloclastite	-	28	x	Amorphous Silica, Anatase, Magnetite, Quartz
IJ13-9	Námaskard	hyaloclastite	-	32.2	x	Amorphous Silica, Anatase, Natroalunite, Quartz, Zeolite?
IV14-8	Hverir	basalt	fumarole	76.8	200	Amorphous Silica, Anatase, Cristobalite
IV14-9	Hverir	basalt	fumarole	71.3	200	Alunite, Antase, Cristobalite, Hematite
IV14-10	Hverir	basalt	fumarole	69.6	200	Amorphous Silica, Anatase, Cristobalite, Natroalunite
IV14-13	Hverir	basalt	fumarole	38.1	400	Amorphous Silica, Anatase
IV13-6	Hverir	basalt	fumarole	66.9	30 - 120	Amorphous Silica, Antatse

IV13-8	Hverir	basalt	fumarole	68.5	200 - 260	Amorphous Silica, Anatase, Quartz
IV13-9	Hverir	basalt	fumarole	14.4	280 – 400	Amorphous Silica, Anatase
IV13-12	Hverir	basalt	fumarole	14.4	280 – 400	Amorphous silica, Anatase
IF13-5	Leirhnjúkur	basalt	fumarole	95.1	40	Amorphous silica, Anatase, Elemental Sulfur, Gypsum, Rostite
IF13-7	Leirhnjúkur	basalt	fumarole	97.1	20	Amorphous Silica, Alunogen, Anatase, Gypsum, Kaolinite, Natroalunite, Zeolite
Purple sediment						
IF14-26	Leirhnjúkur	hyaloclastite	fumarole	96.4	x	Igneous (Plagioclase), Alunogen, Hematite, Jarosite, Quartz, Rostite
IJ13-10	Námaskard	hyaloclastite	-	19.8	x	Amorphous Silica, Alunogen, Anatase, Hematite, Natroalunite, Quartz, Zeolite
IV13-14	Hverir	basalt	fumarole	x	500	Amorphous Silica, Anatase, Hematite, Jarosite, Natroalunite
Red sediment						
IF13-13R	Leirhnjúkur	hyaloclastite	mud pot	12.4	200	Anatase, Hematite, Kaolinite, Maghemite, Quartz
IF13-19	Leirhnjúkur	hyaloclastite	fumarole	47.6	x	Alunogen, Anatase, Hematite, Goethite, Rostite
IJ13-7	Námaskard	hyaloclastite	-	33	x	Alunogen, Anatase, Hematite, Quartz, Smectite (Montmorillonite), Zeolite
IF13-9	Leirhnjúkur	basalt	fumarole	83.4	20	Anatase, Hematite, Kaolinite, Natroalunite, Zeolite
Relict red sediment						
IF14-8	Lítli-Leirhnjúkur	hyaloclastite	-	ambient	x	Anatase, Hematite, Kaolinite, Smectite (Vermiculite, Saponite)
IF14-9	Lítli-Leirhnjúkur	hyaloclastite	-	ambient	x	Anatase, Hematite, Kaolinite
Clay-rich sediment						
IF13-13W	Leirhnjúkur	hyaloclastite	mud pot	12.4	200	Anatase, Kaolinite, Magnetite, Quartz

IF13-20	Leirhnjúkur	hyaloclastite	fumarole	85	Near Vent	Anatase, Kaolinite
IF13-21	Leirhnjúkur	hyaloclastite	fumarole	85.3	x	Anatase, Hematite, Kaolinite, Quartz, Rostite, Smectite (Montmorillonite)
IF14-22	Leirhnjúkur	hyaloclastite	fumarole	ambient	x	Anatase, Alunogen, Clinoptilolite (zeolite), Rostite, Smectite (Montmorillonite, Saponite)
IF13-18	Leirhnjúkur	hyaloclastite	fumarole	31.4	x	Alunogen, Anatase, Jarosite, Kaolinite, Smectite (Montmorillonite), Rostite
Relict clay-rich sediment						
IF14-3	Lítli-Leirhnjúkur	hyaloclastite	-	ambient	x	Anatase, Kaolinite
IF14-4	Lítli-Leirhnjúkur	hyaloclastite	-	ambient	x	Anatase, Kaolinite, Smectite (Vermiculite)
IF14-6	Lítli-Leirhnjúkur	hyaloclastite	-	ambient	x	Anatase, Halloysite, Kaolinite
IF14-7	Lítli-Leirhnjúkur	hyaloclastite	-	ambient	x	Anatase, Kaolinite
Gypsum Mound						
IF14-19	Leirhnjúkur	hyaloclastite	-	ambient	x	Gypsum
IF14-20	Leirhnjúkur	hyaloclastite	-	ambient	x	Gypsum
IF14-21	Leirhnjúkur	hyaloclastite	-	ambient	x	Gypsum, Kaolinite, Variscite

[a] Mineral phases are listed in alphabetical order

[b] Distance = Distance away from an active thermal feature

[c] Range in distance may represent the a specific surface unit where the sample was collected

"-" No thermal feature present

"?" Unknown substrate

"x" Did not measure

Appendix D

Detailed List of Samples from Depth Profile

Table 8: Detailed list of samples from depth profiles

Depth profiles at the Hverir fumarolic apron

Sample No.	T °C	Depth (cm)[a]	Mineral Assemblage
Near Fumarole; 65 cm depth			
IV14-20	97	10 - 40	Elemental Sulfur
2 m away; 70 cm depth (South Wall)			
IV14-6	73.2	16 - 28	Amorphous Silica, Anatase, Cristobalite
IV14-7	76.2	28 - 38	Anatase, Hematite, Kaolinite
2 m away; 70 cm depth (North Wall)			
IV14-8	76.8	13 - 38	Amorphous Silica, Anatase, Cristobalite
IV14-9	71.3	38 - 68	Alunite, Antase, Cristobalite, Hematite
IV14-10	69.6	68 - 70	Anatase, Cristobalite, Natroalunite
4 m away; 60 cm depth			
IV14-13	38.1	0 - 60	Amorphous Silica, Anatase
6 m away; 70 cm depth			
IV14-14	20.6	throughout	Anatase, Goethite, (Natro)Jarosite/Alunite
IV14-15	40.5	0 -70	Amorphous silica, anatase
IV14-16	-	70	Anatase, Gypsum, Hematite, Jarosite, Natroalunite
8 m away; 68 cm depth			
IV14-17	19.5	10 - 40	Anatase, Kaolinite, Hematite
IV14-18	25.1	14 - 34	Alunite, Anatase, Hematite, Kaolinite
IV14-19	39.1	34 -68	Amorphous Silica, Alunogen, Anatase, Elemental Sulfur

Depth profiles atop of Námaskard

Sample No.	T °C	Depth (cm)	Mineral Assemblage
Adjacent to mud pot (near water sample IV14-23); 25 cm depth			
IV14-24	30.5	0 - 1	Anatase, Alunogen, Jarosite, Quartz, Rostite, Smectite (Montmorillonite), Zeolite
IV14-25	33.4	1 - 3	Anatase, Quartz
IV14-26	61.2	3 - 25	Amorphous Silica, Anatase, Kaolinite, Pyrite, Rozenite
Adjacent to mud pot (near water sample IV14-29); 28 cm depth			
IV14-31	36.2	0 -6	Alunite, Amorphous Silica, Anatase, Elemental Sulfur, Natroalunite, Rhomboclase
IV14-32	51.2	6 - 10	Amorphous Silica, Anatase, Elemental Sulfur, Natroalunite, Stellerite
IV14-30	74.6	10 - 28	Anatase, Kaolinite, Marcasite, Pyrite

Depth profiles at Lítli-Leirhnjúkur

Sample No.	T °C	Depth (cm)	Mineral Assemblage
Northern end of hyaloclastite ridge; 50 cm depth			
IF14-3	-	0 - 5	Anatase, Kaolinite
IF14-4	-	5 - 10	Anatase, Kaolinite, Smectite (Vermiculite)

IF14-5	-	10 - 50	Anatase, Halloysite, Kaolinite
Southern end of hyaloclastite ridge; 60 cm depth			
IF14-7	-	5 - 10	Anatase, Kaolinite
IF14-8	-	10 - 20	Anatase, Hematite, Kaolinite, Smectite (Vermiculite, Saponite)
IF14-9	-	20 - 60	Anatase, Hematite, Kaolinite

Depth profiles atop of Leirhnjúkur

Sample No.	T °C	Depth (cm)	Mineral Assemblage
Southern end of hyaloclastite ridge; 50 cm depth (South Wall)			
IF14-24	97	7 - 21	Anatase, Elemental Sulfur, Rostite
IF14-26	96.4	21 - 50	Alunogen, Anatase, Hematite, Heulandite, Smectite (Montmorillonite) Quartz, Rostite
Southern end of hyaloclastite ridge; 50 cm depth (North Wall)			
IF14-23	68.2	0 - 10	Alunite, Alunogen, Goethite, Magnetite, Quartz, Rostite, Stellerite
IF14-25	89.2	10 - 50	Anatase, Alunogen, Geothite, Hematite, Kaolinite, Montmorillonite

[a] Depth = Represents the thickness of a specific layer (or unit) where the sample was collected

Appendix E

Field Description and Mineralogical Composition of Representative Samples

Table 9: Field description and mineralogical composition of representative samples from Figure 13

Sample No.	Sample Type	Descriptions	Major/Mineral Phases[a]	Accessory Phases[b]
F13-8	**Sulfur-rich**	Massive yellow deposits from active vapor discharge area (T = ~100°C)	elemental sulfur (M), anatase (m)	-
F13-17	**Gray mud**	Saturated, gray mud near boiling mud pot (T = 75°C, pH 2)	pyrite (M), amorphous silica (M), sulfur (m)	marcasite, anatase, alunite-jarosite, alunogen, kaolinite
V13-3	**White precipitate**	Fibrous to acicular crystalline aggregates of yellowish white color overlaying dark gray mud adjacent to an active mud pot (T = 65 °C, pH ~2).	halotrichite-pickeringite (M), gypsum (m)	szomonokite
J13-1	**Orange precipitate/ sediment**	Similar as F13-6; except collected from fumarole on the hyaloclastite substrate.	alunogen (M), natrojarosite (M), smectite (M), quartz (m)	gypsum, natroalunite, igneous
F13-20	**Clay-rich**	White to gray, clay-sized particles collected near active venting area.	kaolinite (M), anatase (m)	-
F13-21	**Clay-rich**	Similar to sample F13-20. Collected <1 m away.	smectite (M), hematite (m), quartz (m)	anatase, kaolinite, rostite
V13-12	**Silica-rich**	Loose, damp light yellow fine-grained sediment in between extensively altered cobble-sized basalt ~2 m away from large sulfur mound with no visible discharge vapor present.	amorphous silica (M), anatase (m)	-
V14-8	**Silica-rich**	Massive, saturated yellow clay-sized sediment proximal to the large sulfur mound (T = ~77°C).	amorphous silica (M), cristobalite (M), anatase (m)	-
J13-8	**Silica-rich**	Similar to V13-12. Collected ~10 m away from focused steam vent (>100°C) and adjacent to discharge channel at Námaskard.	amorphous silica (M), anatase (m), quartz (m)	natroalunite
V13-14	**Purple sediment**	Dark purple to red altered basalt with similar purplish colored loose sediment ~5 m away from large sulfur mound.	amorphous silica (M), natroalunite (M), jarosite (m), hematite (m)	kaolinite, anatase
V13-13	**Red sediment**	Loose, dark-red medium-grained basaltic soil. Altered basalt pieces feature white veins and surface coating ~6 m away from the large sulfur mound.	hematite (M), jarosite (m), amorphous silica (m)	goethite, natroalunite
F13-19	**Red sediment**	Predominately bright-red clay-sized particles with small black streaks intermixed.	hematite (M), geothite (m)	anatase, alunogen, rostite
F14-21	**Gypsum Mound**	Small blue-green nodules (<0.6 cm) were randomly dispersed within the depth profile in the gypsum mound.	variscite (M), gypsum (m)	kaolinite

[a] M = major, m = minor [b] Accessory minerals are found in trace abundance